ION BEAM MODIFICATION OF SURFACES IN THE NANOSCALE DOMAIN

Barbara Šetina Batič

Doctoral Dissertation
Jožef Stefan International Postgraduate School
Ljubljana, Slovenia, June 2010

Evaluation Board:

Doc. Dr. Borivoj Šuštaršič, IMT, Lepi pot 11, Ljubljana, Slovenia

Prof. Dr. Ugo Valbusa, University of Genova, Via Dodecanesco 33, Genova, Italy

Prof. Dr. John T. Grant, University of Dayton, Ohio, USA

MEDNARODNA PODIPLOMSKA ŠOLA JOŽEFA STEFANA
JOŽEF STEFAN INTERNATIONAL POSTGRADUATE SCHOOL

Barbara Šetina Batič

ION BEAM MODIFICATION OF SURFACES IN THE NANOSCALE DOMAIN

Doctoral Dissertation

MODIFIKACIJA POVRŠIN Z IONSKIM CURKOM NA NANONIVOJU

Doktorska disertacija

Supervisor: Prof. Dr. Monika Jenko

Ljubljana, Slovenia, June 2010

Contents

Abstract **vii**

Povzetek **viii**

Abbreviations **ix**

1 Introduction **1**

2 Literature review **3**
- 2.1 Historical overview . . . 5
- 2.2 Patterns and patterning regimes . . . 7
  - 2.2.1 Bradley-Harper theory: ion-induced ripple orientation . . . 8
  - 2.2.2 Ehrlich - Schwoebel instability: surface crystallinity . . . 11
  - 2.2.3 Kinetic roughening - athermal Bradley - Harper behavior . . . 12
  - 2.2.4 Non-roughening regime . . . 12
- 2.3 The atomistic approach - theory of sputtering . . . 13
  - 2.3.1 Initial sputtering damage . . . 13
  - 2.3.2 Defect evolution after the ion impact . . . 14
- 2.4 Patterning thin films . . . 16
- 2.5 Metals . . . 21
- 2.6 Possible applications of ion beam nanostructured surfaces . . . 27

3 Aims and hypothesis **29**

4 Experimental **31**
- 4.1 Materials . . . 31
  - 4.1.1 Gold films deposited on glass . . . 32
  - 4.1.2 FeSiAl alloys . . . 33
- 4.2 Sputtering . . . 34
- 4.3 Characterization of resulting structures . . . 36
  - 4.3.1 Atomic force microscopy . . . 36
  - 4.3.2 SEM with EDS/WDS . . . 40
  - 4.3.3 EBSD - Crystallographic Information in the SEM . . . 42

5 Ion beam patterning of thin polycrystalline films 45
5.1 Thin Au film growth 46
5.2 Sputtering results 52
5.2.1 Sputter deposited thin films 52
5.2.2 Evaporated thin films 54
5.2.3 Patterning a flat film with large grains 56
5.3 Shadowing instability 57
5.4 Grains and grain boundaries 60

6 FeSiAl polycrystalline alloy - characterization of structures 63
6.1 Classification of features 63
6.2 Intergranular structures 64
6.3 Intragranular effects 66
6.3.1 Etch pits - an example of depressed features 66
6.3.2 Protuberant structures - triangular facet-like structures 68
6.3.3 Periodic ripple-like structures 71
6.3.4 Smoothing of individual crystal grains 73

7 The role of grain orientation 75
7.1 Initial characterization of the alloy 75
7.2 Normal incidence sputtering 78
7.2.1 Origin of the etch pits 82
7.3 Off-normal incidence sputtering 83
7.4 Single crystal substrates 86
7.4.1 Initial characterisation 86
7.4.2 Etch pit formation 87

8 Conclusions 91
8.1 Contribution to science 92

Acknowledgments 93

Bibliography 94

A Selected bibliography of the author 117

Abstract

Ion beam sputtering induces morphological as well as compositional changes on the surfaces of ion-sputtered substrates. The surface undergoes kinetic processes, which lead to different morphological details: periodic ripples, substrate-defined etch pits or protuberant structures, roughening and smoothing are some possibilities for surface evolution.

The aim of my doctoral dissertation was to explore Ar^+ ion beam-induced patterns formed on three different classes of metallic substrates: thin polycrystalline films, polycrystalline alloy and single crystal materials. The substrates were sputtered by Ar^+ ions of 0.8 - 10 keV at different ion fluences, and the resulting morphological features were characterized adopting a multi-technique approach: Atomic force microscopy (AFM) for determination of surface roughness and resulting structure morphology; Scanning electron microscopy (FE-SEM) for visualization of surfaces at a larger scale, Electron backscatter diffraction (EBSD) technique was used for the determination of texture and individual crystal properties.

Thin films were prepared by different methods to achieve different starting roughness and grain sizes. After off-normal grazing incidence sputtering the films exhibit elongated ripples with wavelengths comparable to grain sizes in the order of 100 nm; and after prolonged sputtering the ripples become more regular. The initial wavelength selection process is governed by the so-called shadowing effect of the larger and taller grains, resulting in initial wavelengths comparable to grain sizes.

As a polycrystalline alloy, FeSiAl steel (silicon steel; electrical steel) was used. The sputtering was performed at normal and off-normal incidences. The results show a grain-orientation dependent behavior that is concise with formation of chemically induced etch pits on the surface of alloys of similar composition at normal incidence sputtering. At off-normal incidence, the surface undergoes changes that result in ripples, facets or smoother surfaces; depending on the individual crystal grain orientation.

Electron backscatter diffraction along with scanning electron microscopy was employed to correlate the individual crystal orientation to the pattern formed inside that individual grain. To compare the results obtained from polycrystalline alloys, single crystal substrates of well-defined orientations were used. The sputtering at normal incidence again results in the formation of etch pits with crystal symmetry.

Povzetek

Pod vplivom ionskega curka se spremeni morfologija in kemijska sestava površine. Kinetični procesi, ki sodelujejo pri preoblikovanju površine, vodijo do formacije različnih površinskih vzorcev. Glede na parametre ionskega snopa (energija, tok, vpadni kot, vrsta ionov...) in samega substrata se lahko na površini pojavijo valovite strukture, jedkalne figure z značilno obliko, piramide, povečana hrapavost ali pa glajenje površine. Glavni namen moje doktorske disertacije je bil preučiti vpliv ionskega jedkanja z Ar^{+} ioni na treh različnih kovinskih substratih: tankih polikristaliničnih filmih, polikristalinični zlitini in monokristalih različnih orientacij. Substrate sem jedkala z ionskim snopom energij od 0.8 keV do 10 keV z različnimi časi izpostavitve.
Nastale strukture sem karakterizirala z več tehnikami: vrstična elektronska mikroskopija z izvorom na poljsko emisijo (FE-SEM) je služila ogledu površine na večji skali, medtem ko sem mikroskopijo na atomsko silo (AFM) uporabila za določitev parametrov hrapavosti in periodičnosti površinskih struktur. Z metodo uklona povratno sipanih elektronov (EBSD) pa sem lahko korelirala orientacijo posameznih kristalnih zrn in vzorce, ki so se pojavili na njih.
Tanke filme sem pripravila na različne načine, s tem sem dobila plasti z različnimi začetnimi parametri hrapavosti in velikosti posameznih zrn. Pri ionskem jedkanju pod velikim vpadnim kotom se pojavijo valovite strukture, ki so povezane z začetnimi lastnostmi filmov. Proces izbire valovne dolžine struktur je koreliran s povprečno velikostjo zrn zaradi vpliva senčenja.
FeSiAl zlitina je bila uporabljena kot modelni sistem za polikristalinične zlitine. Substrat sem jedkala pri pravokotnem vpadu in pod večjim kotom. Strukture, ki so tako nastale, so korelirane z individualno orientacijo posameznih zrn. Znotraj enega zrna se formira karakterističen vzorec, ki sem ga lahko povezala s kristalno orientacijo. pri pravokotnem vpadu se pojavijo jedkalne figure (jamice), ki s svojo obliko kažejo na orientacijo zrna. Pri večjem vpadnem kotu se strukture lahko razdelijo na 4 različne morfologije, vsaka pa je konsistentno prisotna za določeno orientacijo.

Abbreviations

AFM	Atomic force microscopy
SEM	Scanning electron microscopy
EDS	Energy dispersive spectroscopy
WDS	Wavelength dispersive spectroscopy
EBSD	Electron backscatter diffraction
XPS	X-ray photoelectron spectroscopy
AES	Auger electron spectroscopy
EBSD	Electron backscatter diffraction
SIMS	Secondary ion mass spectroscopy
BH	Bradley Harper
ES	Ehrlich Schwoebel
b.c.c.	Body centered cubic cell
f.c.c.	Face centered cubic cell
RMS	Root mean square

1 Introduction

Imagine sending a high velocity projectile towards a target and a picture of light, sound, and debris instantly comes up. A similar process on an atomic scale is ion beam sputtering - the projectile is an ion and the debris the atoms ejected from the target. These microscopic explosions have been turned into a versatile tool for precisely controlling the morphology of a material.

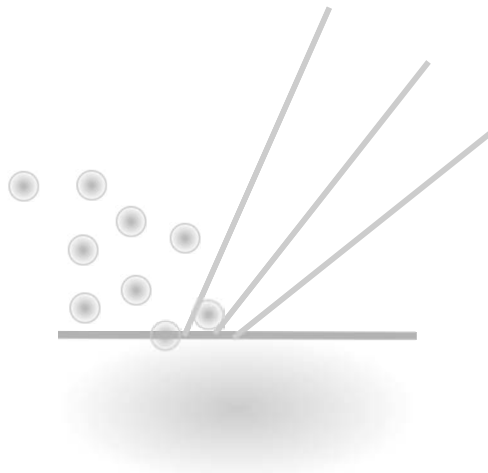

Figure 1.1: Sputtering by ion beam. As ions strike the surface, they produce sputtering of the atoms from the substrate.

Sputtering by an ion beam is applicable in industry as well as in the laboratory. In fact, it even occurs in nature. The fabrication of a microprocessor, laser or microelectromechan-

ical (MEMS) device [1] usually involves several steps of ion beam etching. The devices are built step by step defining submicron scale features with lithography and ion beam drilling. Energetic ions are routinely used to clean surfaces and to deposit thin films. On a planetary scale, sputtering by energetic particles in the solar wind (H^+, He^+) [2, 3] has important implications for the evolution of planetary surfaces.

When ion beams are used to bombard a surface of a material, the surface often develops a periodic pattern. Different pattern types form depending on conditions: the substrate material, ion beam energy, angle and fluence all play a major role. Because the pattern develops spontaneously, that is without applying any external mask or template, there is substantial scientific and technological motivation for understanding surface evolution during sputtering.

Highly ordered surface structures can be formed quite inexpensively over large areas, which can be of technological importance for potential applications such as quantum dot arrays with highly controlled optoelectronic properties, or magnetic media for high-density storage. Besides applications in technology, understanding of pattern formation is also of scientific relevance, giving new insight into fundamental non-equilibrium processes of surface evolution.

While there is a lot of experimental data and theoretical knowledge concerning single crystal substrates and amorphous materials of a well defined composition, only little is known about polycrystalline alloy materials that contain multiple components, and thin film materials, where grains and grain sizes are expected to play an important role in the pattern formation. The main aim of this thesis is to explore ion beam sputtering phenomena and surface morphological changes related to sputtering in polycrystalline metallic materials: thin films as well as bulk alloy materials.

2
Literature review

The phenomenon of ion beam sputtering has been known for more than one hundred years, but the last decades have seen a growing interest for experimental evidence and theoretical development of models that explain the processes governing surface evolution and ion beam - surface interactions. A review of the latest developments in this field is given, for example, by Chan and Chason [4]. The development seen is in part due to advances in the fields of nanotechnology, fabrication of MEMS/NEMS devices, and a growing interest for surface analytical techniques, which employ ion beam sputtering for the preparation of clean surfaces.

An example of a pattern developed after irradiation of a SiO_2 surface after sputtering by 1 keV Xe ions at room temperature conditions and the experimental set-up is shown in fig. 2.1. The resulting structure is a well-defined periodic ripple pattern, with a periodicity of about 30 nm and ripple amplitude of about 1 nm, when approximately 30 nm of material has been removed. The ripples have formed uniformly over a large area of the surface.

Variations of this behavior can be observed depending on the sputtering conditions and the materials used: ripple wavelengths can range from nanometers to micrometers, their alignment can be matched to be parallel or perpendicular to the ion beam projection, or it even might be consistent with the material's crystal structure and orientation. It is possible for the surface to develop one-dimensional highly ordered ripples [6, 7], but mounds, pyramids, and pits have also been widely reported in the literature [8, 9].

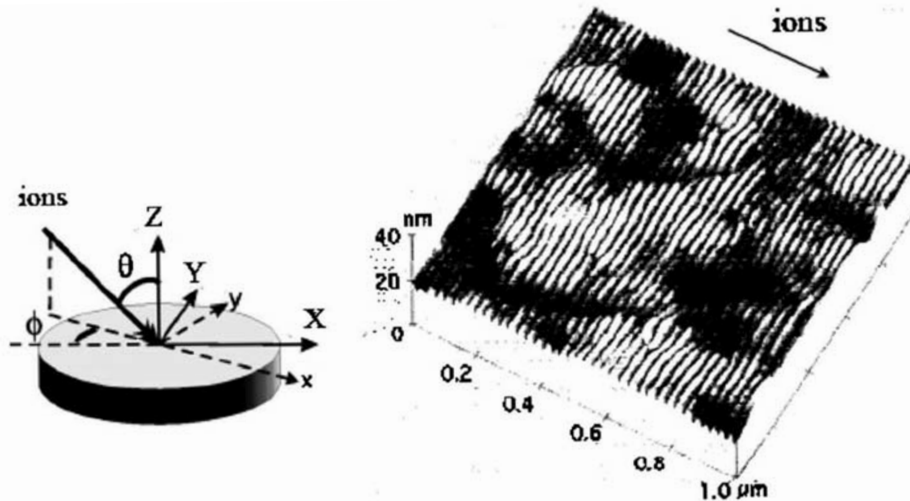

Figure 2.1: An Xe ion beam sputtered solid SiO_2 surface. Image from [5].

It is also possible, under certain conditions, that the surface undergoes a layer-by-layer erosion [10, 11], smoothing [12, 13, 14] or self-affine roughening, where the surface does not develop any characteristic periodicity [15].

Upon ion irradiation, some topography will inevitably develop on the surface. The process of ion beam sputtering invariably creates at least atomic scale discontinuities at the surface. Such effects can be observed for smaller ion fluences (individual ion impacts and irradiations up to 10^{16} ions/cm^2, depending on the ion and substrate parameters. As ion fluence increases above this level, the density of atomic scale discontinuities increases and the features become microscopically observable. At high ion fluences, when the bombardment induces sufficient ion induced defects, major changes in surface topography are observed resulting from local variation in sputtering yield and enhanced surface diffusion of ejected atoms.

With the advent of new materials, new processing conditions and improved imaging and analytical techniques there has been a continual back-and-forth between the observation of new phenomena and the development of new models to explain them. A large range of observed morphological features further complicates our basic understanding. However, a comprehensive picture has begun to emerge, which relates the surface patterning to fundamental physical processes governing the ion-solid interaction and surface relaxation kinetics.

2.1 Historical overview

The first systematic studies of ion beam sputtering and the related surface morphological changes began in the early 1950's. One of the first reports of self-organized periodic structures was provided by Navez *et al.*, who observed ion beam induced ripple-like formations on the surface of glass [16]. The ripples they observed had wavelengths of less than 100 nm and were quite regular.

A large variety of other morphologies, such as pits, pyramids and cones were also reported in earlier studies. Carter *et al.* in the 1980s produced an extensive review of observed features in metallic face centered cubic (FCC) substrate sputtering [17]. The authors provided a classification of the resulting ion-beam induced patterns and showed the need of further studies, which would employ well-defined substrates and processing conditions, such as monocrystalline materials with well defined orientations, and a controlled range of ion bombardment settings, including energy, species and incidence angle.

To visualize the surface changes in these early studies, mostly scanning electron microscopy techniques were used [18]. Advances in instrumentation such as the development of scanning probe microscopy in the late 1980s as well as various scattering techniques, such as grazing incidence X-ray scattering (GISAX) and rutherford backscattering spectroscopy (RBS) have also brought significant progress in the field. Higher quality data could be obtained, and it was also possible to observe the kinetics of evolution and single ion impacts *in situ*.

The theory of ion beam induced surface morphological changes developed together with experimental work. The first theoretical proposals employ some sort of roughening mechanisms, such as sputter yield dependence on the local slope, balanced with surface diffusion, to explain the resulting periodic structures. Such an instability theory was proposed in the late 1980s by Bradley and Harper [19], and this model has served as a basis for the development of other models which either extended the basic mechanism by adding additional terms or by including other physical effects. However, the Bradley - Harper model is valid mainly for amorphous materials and materials that become amorphous during the ion impact. As such, this model was unable to provide a comprehensive explanation of pattern formation on metal surfaces (pits, mounds, crystal-orientation dependent ripples). These features were associated with diffusion barriers inducing mass flow and acting as a driving force for pattern formation via the Ehrlich-Schwoebel barrier [20]. With the advances in computer science and computing power, various models based on Monte Carlo calculations [21, 22, 23] or Molecular Dynamics simulations [24, 25] have also been proposed. In this approach, sputtering and surface

diffusion are simulated on an atomistic basis and the collective surface evolution results from the action of many ion impacts.

Ion beam sputtering is also a routinely used technique in various surface science applications, for example surface sensitive techniques such as Auger electron spectroscopy (AES) depth profiling, secondary ion mass spectroscopy (SIMS) analysis and X-ray photoelectron (XPS) depth profiling. In this case, the development of any surface topography hinders the vertical resolution of the techniques, and a lot of effort has been made in order to prevent or at least minimize the formation of morphological features. To a certain extend, this is possible by rotating the specimen during the sputter process or by employing rocking of the specimen [26, 27, 28, 29, 30]. The theory underlying this phenomenon has been developed by Bradley and Cilin [31], who proposed that as the sample is rotated, the smoothing effects of viscous flow and surface self-diffusion can prevail over the roughening effect of the curvature-dependent sputter yield and generate a smoother surface.

2.2 Patterns and patterning regimes

Observation of different behaviors in different systems could suggest that different physical mechanisms were responsible for pattern formation in different systems. For example, Bradley - Harper type ripples mainly form on amorphous and semiconductor systems and can be explained by a balance between diffusion and curvature dependent sputter yield; while ripples oriented along crystallographic directions and other diffusion related effects are mainly observed on metal surfaces and can be explained by the Ehrlich - Schwoebel diffusion barrier. But more recently, it has also been shown that also Bradley-Harper ripples can be induced on single crystal metal substrates using certain processing conditions and that in a similar way semiconductor surfaces exhibit patterning induced by diffusion mechanisms. This leads to the conclusion that multiple mechanisms can be active on the same surfaces and that the variety of observed structures is due to the predominance of different mechanisms in different regimes.

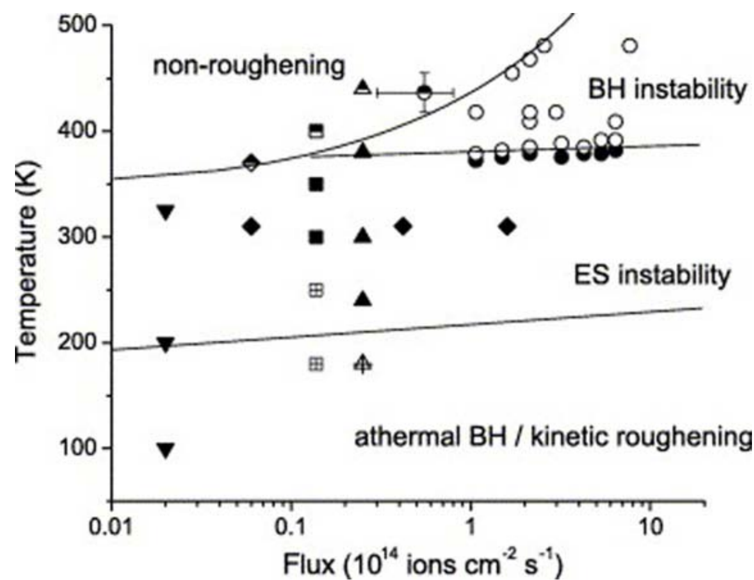

Figure 2.2: Kinetic phase diagram for pattern formation on Cu(001)/Ag(001) surfaces. Each region in the diagram represents a different pattern formed on the surface [32].

To better understand the patterns and the regimes that form during ion beam sputtering, W.L Chan *et al.*constructed what they call ”kinetic patterning diagrams” [32] that enable organization of different patterning behaviors in terms of ion processing conditions and temperature in which they are observed. A kinetic phase diagram for ion-induced patterning on Cu (001) surface is shown in fig. 2.2. The diagram shows that even with variability in the sputtering conditions, different types of behavior cluster into different regions of flux and temperature. Important trends can be identified from the kinetic phase diagram, such as what temperature or flux is needed to change one pattern behavior to another.

The four different regimes that the authors [32] identify in this kinetic phase diagram are **athermal Bradley-Harper/kinetic roughening** behavior for temperatures below 200 K, which at higher temperatures turns into **Ehrlich-Schwoebel** type behavior characterized by crystal-orientation dependent diffusivity. At even higher temperatures the authors observe two possible behaviors: a layer-by layer **non-roughening erosion** for lower ion fluxes and **Bradley-Harper instability** characterized by ion-beam dependent ripple orientation. The diagram clearly shows that different behavior types cluster into different regions of flux and temperature. In the remainder of this section, I will review the different patterning regimes depicted on the diagram and describe the characteristic features of the surface evolution process for each of them.

2.2.1 Bradley-Harper theory of ripple formation - ion-induced orientation

Bradley and Harper [19] developed a theory of sputter-induced pattern formation on amorphous surfaces in 1988. This theory combines the effect of curvature-dependent sputter yield with surface diffusion. The main result of their theory was an explanation of how a surface that undergoes sputtering processes can develop a regular ripple pattern, and the theory also successfully accounts for the ripple wave vector rotation. The theory is valid for surfaces where direct sputtering effects are large and the effect of surface crystallinity on diffusion is relatively low (there is no preferential direction for surface diffusion).

The rate of sputtering depends on the local surface morphology, described by the function $h(x, y)$, as well as the angle θ of the ion beam relative to the surface. Sputtering itself can be approximated by a linear partial differential equation,

$$\frac{\partial h}{\partial t} = -\nu_0 + \frac{\partial \nu_0}{\partial \theta}\frac{\partial x}{\partial h} + \nu_x \frac{\partial^2 h}{\partial x^2} + \nu_y \frac{\partial^2 h}{\partial y^2}. \tag{2.1}$$

The ν_0 is average erosion rate of the bombarded surface, and it depends on θ, the angle of ion incidence, as well as other ion beam parameters and the surface itself. ν_x and ν_y are also functions of ion beam parameters that relate the sputter yield at any point on the surface to the local curvature. More energy is deposited on a surface with negative curvature than on the surface with a positive curvature, and this makes the valleys erode faster than the hilltops. A schematic diagram of this process is shown in fig. 2.3. A similar mechanism can be employed to explain the ripple-like structures that form by wind erosion in the deserts.

The other mechanism that affects the pattern development in ion sputtered surfaces is the diffusion of adatoms, which acts to make a surface smoother. When surface energy

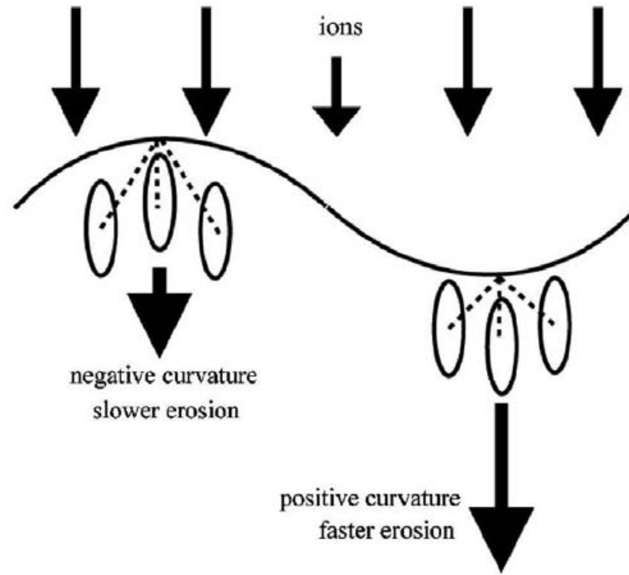

Figure 2.3: More energy is deposited at areas with a positive curvature, leading to a faster sputtering of these areas compared to the areas with a negative curvature. The elliptical shapes represent the deposition of ion energy inside the bulk according to Sigmund sputtering model.

γ is independent of the orientation, the surface chemical potential μ is proportional to local surface curvature. Gradients in surface chemical potential generate the a flux of mobile species. Herring and Mullins [33, 34] determined that the rate of height change due to diffusion is proportional to the divergence of the curvature,

$$\frac{\partial h}{\partial t} = -B\nabla^4 h. \tag{2.2}$$

Parameter B is equal to

$$B = \frac{\gamma D_s C}{n^2 k_B T}. \tag{2.3}$$

In this equation, γ is the surface energy, D_s the diffusivity of a mobile surface defect, C the average concentration of mobile defects on the surface and n is the number of atoms per unit volume. The diffusing species in this model is not determined, and the theory is equally valid for the diffusion of adatoms and surface vacancies.

Bradley and Harper combined the two mechanisms; curvature-dependent sputter yield as the erosion mechanism and surface diffusion as the smoothing mechanism. The surface height evolution is then described by a linear partial differential equation,

$$\frac{\partial h}{\partial t} = -\nu_0 + \frac{\partial \nu_0}{\partial \theta}\frac{\partial x}{\partial h} + \nu_x \frac{\partial^2 h}{\partial x^2} + \nu_y \frac{\partial^2 h}{\partial y^2} - B\nabla^4 h. \tag{2.4}$$

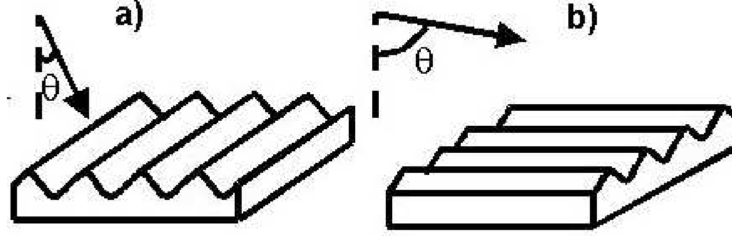

Figure 2.4: Bradley and Harper's theory of sputtering: wave vector rotation. (a) Ripples perpendicular to ion beam direction form at near-normal incidence angles, and (b) ripples parallel to the ion beam form at grazing incidence [19].

The equation 2.4 can be solved in Fourier space. The solution predicts a ripple periodic pattern with a characteristic wavelength λ^*, given by

$$\lambda^* = 2\pi\sqrt{\frac{2B}{\nu_{max}}}. \tag{2.5}$$

The notation ν_{max} equals to the larger of the values of $-\nu_x$ and $-\nu_y$. The orientation of the resulting ripple pattern depends whether ν_x or ν_y is more negative.

The results given by Bradley and Harper, describing the evolution of surface periodic pattern during ion beam sputtering, can be summarized in the following points:

- The wave vector of the resulting pattern depends on the angle of the ion beam projection, as is illustrated in fig. 2.4.
- Resulting wavelength is constant at given temperature.
- The wavelength varies as a function of temperature, obeying the law

$$\lambda \propto \sqrt{\frac{1}{fT}} \exp\left(-\frac{\Delta E}{2k_B T}\right), \tag{2.6}$$

  where f is the ion flux, T is the temperature and ΔE the activation energy.
- The amplitude of the pattern grows rapidly with an exponential time behavior.

The Bradley-Harper theory applies quite well to amorphous materials or crystalline substrates, which become amorphized by a high sputtering rate [35]. For example, Bradley - Harper behavior has been observed on semiconductor GaAs system [36] and Si [37, 38] single crystal substrates. Some reports also show that even for semiconductor materials, sputtered at ambient temperature or at high ion fluxes, the approximation of isotropic diffusivity holds, which is due to a high diffusion energy barrier of such materials [39].

2.2.2 Ehrlich-Schwoebel instability: patterning determined by surface crystallinity

Quite different is the case when the surface diffusion is not isotropic, as is, for example, in single crystal metals. Anisotropic surface diffusion of adatoms and vacancies generates its own surface instabilities, which combine with the beam-induced surface instabilities. Ion impacts create both adatoms and vacancies. In the case of crystalline materials there are various sources of anisotropy: the crystalline structure compels adatoms and vacancies to diffuse along thermodynamically favored directions. Secondly, certain substrates can present extra energy barriers for adatom or vacancy diffusion.

The most commonly employed energy barrier is the so-called *Ehrlich - Schwoebel barrier* [20, 40], an energy barrier to diffusion over step edges, which is known to create morphological instabilities during the deposition process. The Ehrlich - Schwoebel barrier was proposed by Villain [41] to explain roughening in homoepitaxial growth. Due to this barrier, the adatoms preferentially attach to the upper step edges rather than the lower step edges. Although it was originally used to explain growth roughening, it can also be applied to explain pattern formation behavior during sputtering.

The Ehrlich - Schwoebel barrier is mostly applied to metallic substrates, and the main characteristics of this pattern regime are the following:

- Shape and alignment of the mound-like structures depend on the symmetry of the underlying substrate. This means elongated ripples in the case of monodirectional substrates, but also square and hexagonal symmetry mounds respectively for quadratic or triangular surfaces as (001) and (111) f.c.c. as well as b.c.c. crystals.
- Time dependence of their principal morphological parameters is governed by power laws. The power-law coefficients, usually called dynamical exponents, depend non-trivially on various experimental variables among which are also the surface temperature and the values of extra diffusion barriers.

The Ehrlich-Schwoebel mechanism was originally developed to explain growth roughening, but it has also been successfully applied to patterning by sputtering. In this case, the surface defects may be adatoms, vacancies or clusters, but during deposition the defects are mostly adatoms. Golubovic *et al.* predicted the formation of different types of morphologies on (110) and (100) surfaces [42, 43], which have been experimentally observed.

2.2.3 Kinetic roughening - athermal Bradley - Harper behavior

Similarly to the Bradley-Harper behavior, the patterning in this regime is ion-beam orientation dependent. The transition between Ehrlich-Schwoebel governed patterning to Bradley-Harper like patterning is observed at lower temperatures. This transition indicates a decrease in the strength of the diffusive roughening mechanism due to lower diffusivity of mobile species at lower temperatures. The main difference between this regime and the high-temperature Bradley - Harper regime is that the wavelength of the ripple formation depends only weakly on the temperature. In addition to periodic structures, some substrates may also roughen without forming a well-developed pattern [44].

2.2.4 Non-roughening regime

On some crystalline surfaces under certain conditions (low flux, relatively high temperatures) the surface exhibits no roughening, but the sputtering takes place in a layer-by-layer manner [45, 46]. The instability models are not able to predict such behavior and additional physical mechanisms need to be incorporated. Tersoff *et al.* [47] explained the layer-by-layer growth in the homoepitaxial growth of films, and a similar mechanism is expected to govern the surface evolution in non-roughening sputtering. In this model the roughening is limited by kinetic barriers to nucleating new clusters on the surface.

Layer-by-layer erosion has been experimentally observed *in situ* by various scattering techniques, such as He atom scattering [48] on InSb(110) sputtered by low-energy ion bombardment; X-ray reflectivity [49] on Au(111) surfaces bombarded by 70 eV Ar ions that underwent a persistent layer-by-layer erosion (the authors observed more than a hundred cycles of layer-by-layer erosion); and reflection high energy electron spectroscopy [50] of Si(100) by 200 eV and 250 eV Xe bombardment. This technique monitors the intensity of the specular reflected beam as a function of sputtering time. As the surface roughens, the beam intensity decreases, and as such beam intensity provides a good measurement of the substrate roughness evolution. This behavior is observed only in a narrow range of sputtering conditions including ion flux and temperature, and the values are material-dependent.

2.3 The atomistic approach - theory of sputtering

When an energetic ion impinges on a surface, it gives up its considerable kinetic energy in a series of collision events. This results in the ejection of material atoms (sputtering) and creation of numerous defects in the bulk (vacancies and interstitials) and on the surface itself (adatoms and surface vacancies).

2.3.1 Initial sputtering damage

Experimental measurements of a single ion impact have been reported for various substrates using scanning tunneling microscopy or atomic force microscopy on a number of different substrates, for example on Pt [51, 52, 53]; Si(111) [54]; graphite [55, 56], GaAs [57] etc. Other spectroscopic tehniques such as reflection high energy electron diffraction (RHEED), field-ion microscopy (FIM) and transmission electron microscopy were also used in a number of experimental studies, for example [58]. The majority of the experimental work has been performed on crystalline surfaces, such as Si and Pt, and the observations of single-ion impacts or smaller defect clusters indicate that significant mass redistribution can happen on the surface after a single ion impact.

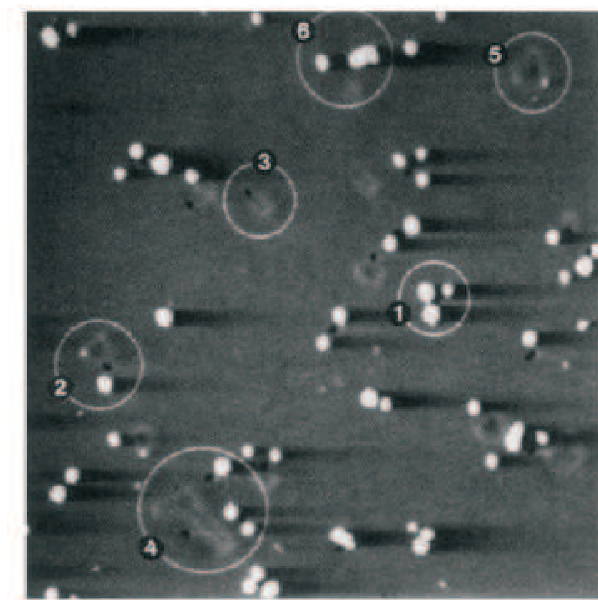

Figure 2.5: Scanning tunneling microscopy image of defects induced by single ion impacts on Pt(111) surface. Bombarding species was Xe at 5 keV. Image size is 770x770 Å^2. The image is taken from [52].

Figure 2.5 shows the damage created by a single ion impact on Pt(111) surface by Xe 5 keV bombardment [52]. The ion fluence in this case was 4.1×10^{11} ions cm^{-2}, and the area in the image shown has received on average 24 ion impacts. A crater has formed

at the center of each impact and it is surrounded by a number of adatom clusters, some single atoms and vacancies.

The type of ion-induced damage created depends on the substrate and the ion. Molecular dynamics and kinetic Monte Carlo simulations [59, 60, 61, 62] enable modeling of the difference of single-ion impacts depending on the bombarding species. Bombardment with heavy ions produces damage concentrated at the point of impact, which is consistent with higher stopping power inside the bulk. Molecular dynamics simulations further suggest that high energy deposited near the surface can cause processes such as local melting of the surface or so-called "microexplosions", which lead to the formation of craters and large adatom clusters near the point of impact. The lighter ions (such as He) induce linear collision cascades creating individual defects on the surface. On amorphous surfaces and surfaces that amorphize during sputtering individual surface defects cannot be as easily distinguished. Bulk and surface defects may manifest themselves only as local variations of atomic density.

Extensive calculations of various species and beam energies, as well as angular dependence of damage produced by an ion impact have been performed by the group of B. Garrison [63, 64], who used molecular dynamics simulations to great success. They were able to quantitatively predict the energy and the angular distributions of the particles ejected from the surface, as well as the collision cascades produced in the solid.

2.3.2 Defect evolution after the ion impact

As ion impacts produce defects and remove material from the surface, subsequent evolution of the surface morphology is determined by surface transport. Defects can diffuse on the surface to smoothen the morphology and minimize the surface free energy. On crystalline surfaces the presence of steps can modify the diffusion kinetics or even lead to roughening in the presence of barriers to interlayer diffusion. Amorphous surfaces can experience ion-enhanced viscous flow.

While sputtering and surface defect generation leads to roughening of the surface, defect diffusion usually acts to make the surface smoother. An isotropic surface, where the surface energy is independent of the orientation, the relaxation of the surface is driven by the reduction of total surface area. For crystalline surfaces the surface energy is orientation dependent. In the presence of steps, the evolution of the surface height depends on the morphology in a complicated non-linear way. Transport on the surface can be controlled by the rate of diffusion across the terrace and over step edges as well as attachment/detachment of atoms to/from the step edge.

Ion-induced surface defect diffusion can also lead to the roughening of the surface through several mechanisms. One well-known roughening mechanism is induced by

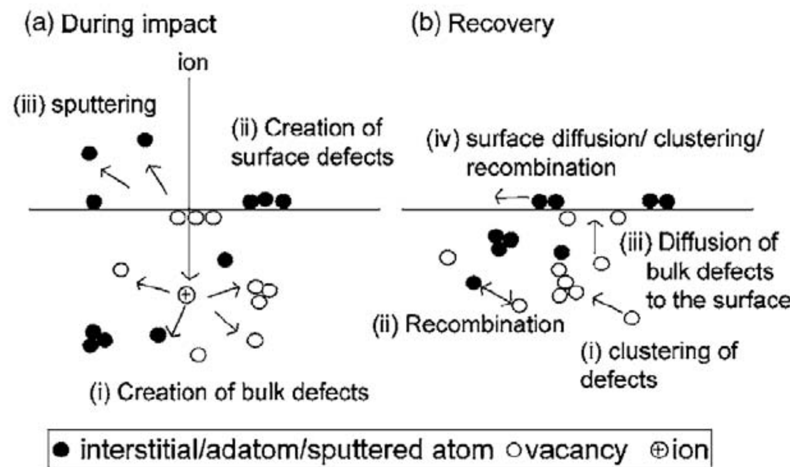

Figure 2.6: Schematic representation of ion impact and defect evolution [4]. (a) An ion bombards the solid surface, defects are created in the bulk and on the surface. Some atoms are sputtered away, leaving vacancies on the surface. (b) Evolution after the ion impact: defects annihilate and recombine; bulk defects can diffuse to the surface to create surface defects.

barriers to diffusion of adatoms and surface vacancies across step edges (Ehrlich-Schwoebel barriers). The presence of an ES barrier causes flux of surface defects to increase the roughness of the substrate. This mechanism induces a pattern that follows the crystallographic directions of the surface, in contrast to the ion-induced mechanism that creates ripples along the ion beam direction. This instability is usually found on metal surfaces with a significant ES barrier, as in for example Pt(111), Au(111), Ag(001), Ag(110), Cu(110) and Co(0001).

2.4 Patterning thin films

Thin film systems have only recently attracted attention, as they are a class of materials that is often used in applications such as optical devices, magnetic coatings and storage media. Recent studies of ion beam sputtering of thin films show that such systems can also be patterned by ion beam. This has been shown in numerous recent publications, as is for example [65] and [66], along with some others.

A number of metal films, for example Al, Co, Cu, Ag, Pt and Au are found to be prone to perpendicular ripple formation on the material surfaces when irradiated by a grazing incidence angle (usually of more than 70°) by inert gas ions (such as Ar^+ gas) as well as with reactive gas ions as is O_2^+ [67]. Extensive results of patterning thin films is given in [68]. The films were prepared by physical vapour deposition techniques at room temperature in a magnetron sputter unit onto polished Si(100) wafers. The authors observe a dependence of morphology on the sputtering angle. Up to 50° incidence angle a cone-like morphology is observed. Further increase of the incidence angle shows the beginning of distinct changes of the surface morphology which ultimately ends up with regular ripple structures at grazing ion incidence. At 60° weakly pronounced ripples with a wave vector parallel to the ion beam direction, especially in Co and Cu films, appear. At 70° the morphology shows the development of arrays of tiny cones aligned along the projection of the ion beam direction. Finally, at 80° regular ripple-like surface instability with the wave vector perpendicular to the ion beam direction is developed.

The rotation of the ripple wavevector by 90° is one of the most important theoretical predictions of the BH model. In the angular range of 30° to 60° the ripple wavevector is parallel to the ion beam direction, and for incidence angles greater than 60 ° the ripples are formed with the wavevector perpendicular to the ion beam direction. The threshold angle is solely dependent on the shape of the deposited energy distribution for a particular ion/target combination. At the point of impact, the kinetic energy carried by the incident ion is dissipated inside the surface forming a collision cascade around the ion track.

Another fact that needs to be considered concerning the patterning of metal films is that the films are composed of individual grains. In order to extend the results found on single crystal substrates and to apply the mechanisms to thin films, one must take into account the influence of the vertical and lateral corrugation of the pristine film. During ion beam sputtering, the thin film systems will first undergo some smoothing (decreasing the RMS roughness) before a regular pattern starts to form [67, 69]. For small scale initial roughness, different atomistic smoothing processes such as surface diffusion, redeposition, ballistic drift of recoil adatoms etc. dominate in the evolution of surface topography during early stages of sputtering. In the late stages of sputtering, the

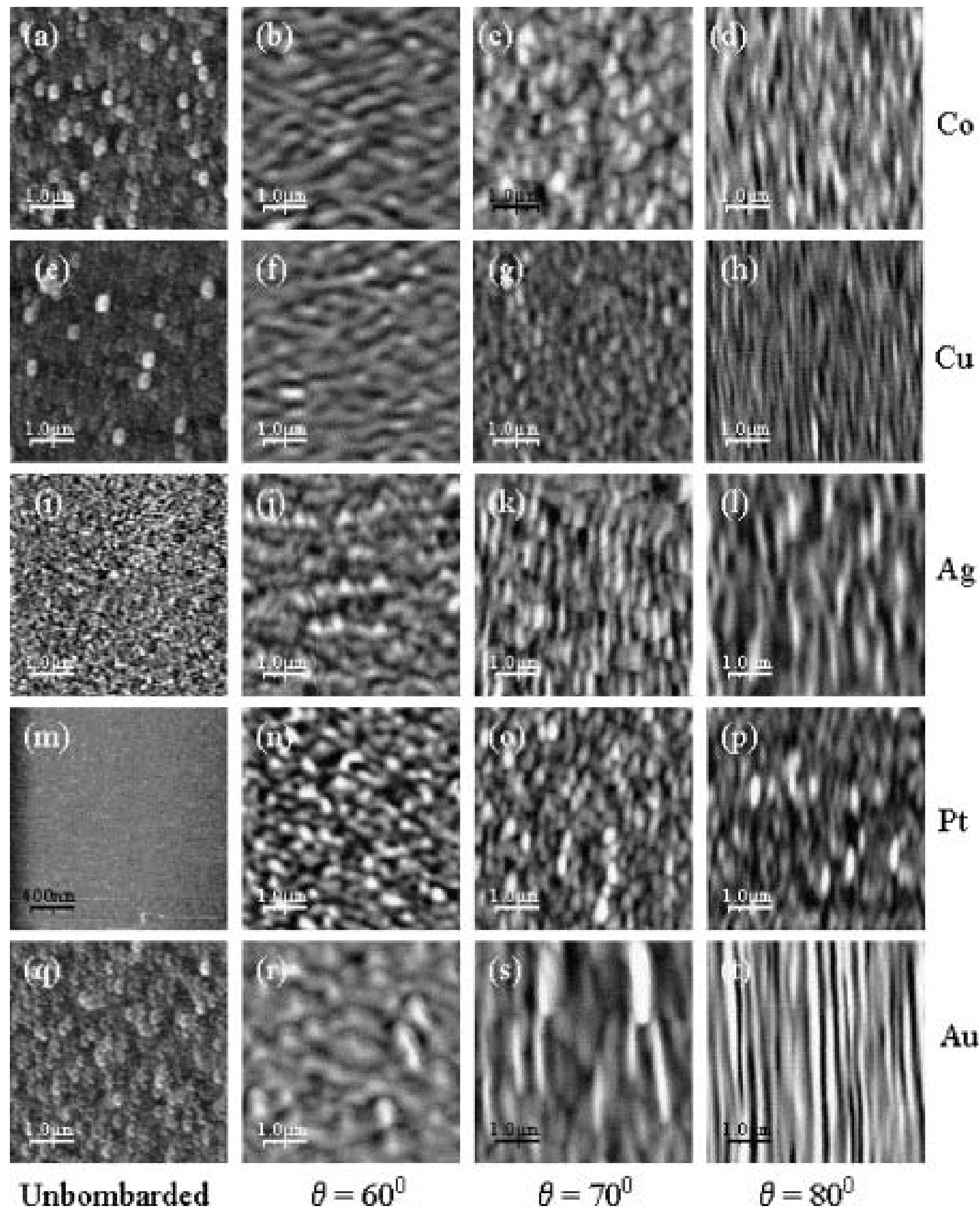

Figure 2.7: AFM images of the unbombarded and 16.7 keV Ar+ sputtered Co, Cu, Ag, Pt and Au surfaces at different angles of incidence. The bombarding fluence for Co, Cu, Ag, and Au is 1×10^{17} ions/cm^2, while that for Pt is 5×10^{16} ions/cm^2. The ion beam direction is from the bottom to the top. Image from Karmakar *et al* [68].

curvature-dependent roughening mechanism is more active and ripple-like topography develops. This behavior indicates the presence of two distinct topographical regimes: the ion beam smoothing regime, where the surface roughness decreases (usually following an inverse power law) and the roughening regime, where the roughness evolution follows a power law increase.

Ion beam sputtering must not always lead to regular pattern formation, and the same holds for ion beam sputtering of thin films. Rough, self-affine surfaces have been reported in Fe films under 5 keV Ar ion bombardment at 25° angle of incidence [70]. D. Ghose *et al.* report that they observed no ripple formation on a number of inert gas ion sputtered films, but the surfaces underwent kinetic roughening in the form of irregular mounds or bump-like structures. These structures formed just when the incidence angle was less than 50° to 60°. One such example is shown in fig. 2.8, where a thin Pt film is shown to undergo kinetic roughening transformation. With increasing sputter time, the lateral size and height of the mounds are found to increase. Under continuous bombardment, the structures finally shrink.

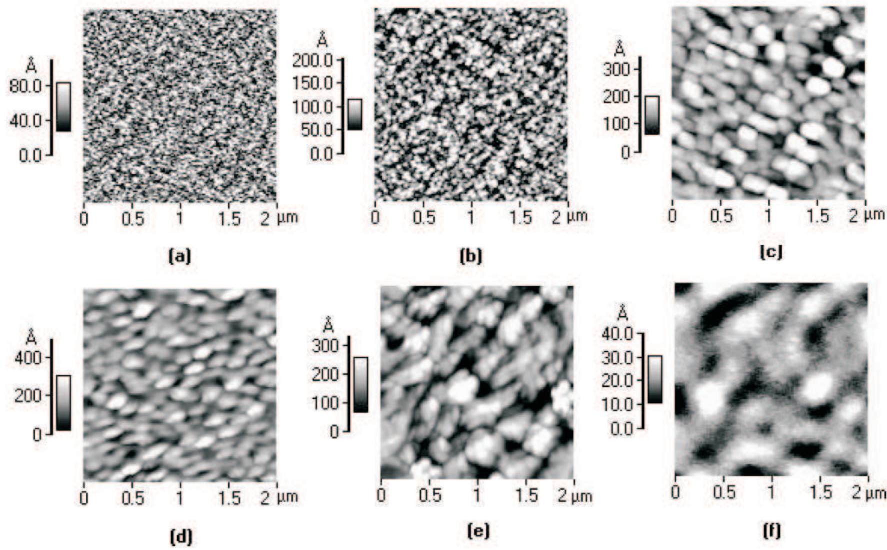

Figure 2.8: Images of 9.7 keV Ar^+ sputtered 30 nm Pt thin films at an angle $\theta = 45°$, showing a sequence of the evolution of surface topography with increasing ion fluence. Image from Gose *et al.* [65].

There have also been efforts to perform some simulations of kinetic self-organisation in thin metal films. Stepanova *et al.* report on their results [71] of Kinetic Monte Carlo simulations (KMC) and their application to thin metal films. The model they used is depicted in fig. 2.9. It accounts for two major factors defining the surface morphology: sputtering of surface atoms due to energy deposition by the ions, and thermally activated surface diffusion. The surface is described as a height function $h(i,j)$, where $\{i,j\}$ denote the position in a grid with periodic boundary conditions. When an atom is added or removed at a cell at $\{i,j\}$, the height $h(i,j)$ changes by one atom size. Incident ions are generated at random positions above the surface, and ion impact position is defined as is shown in fig. 2.9. Such impact mechanism naturally accounts for shadowing of the Ar trajectories by surface morphology, which leads to shadowing effects of some surface regions, as is described for example in [72, 73].

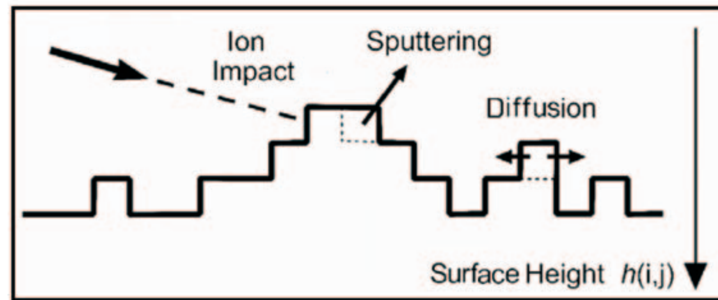

Figure 2.9: Model that describes the surface of a thin film undergoing ion beam sputtering. Image from [71].

Upon reaching the surface, Ar ions are either reflected with the probability dependent on the local angle of incidence [74, 75] or penetrate inside the surface and deposit their energy into a volume of ellipsoidal shape, as the authors find that this is the volume shape of energy deposition in Cu [76]. After each energy deposition event, surface atoms are removed at a probability based on the sputtering yield, and computed through formalism that is dependent on local angle of incidence.

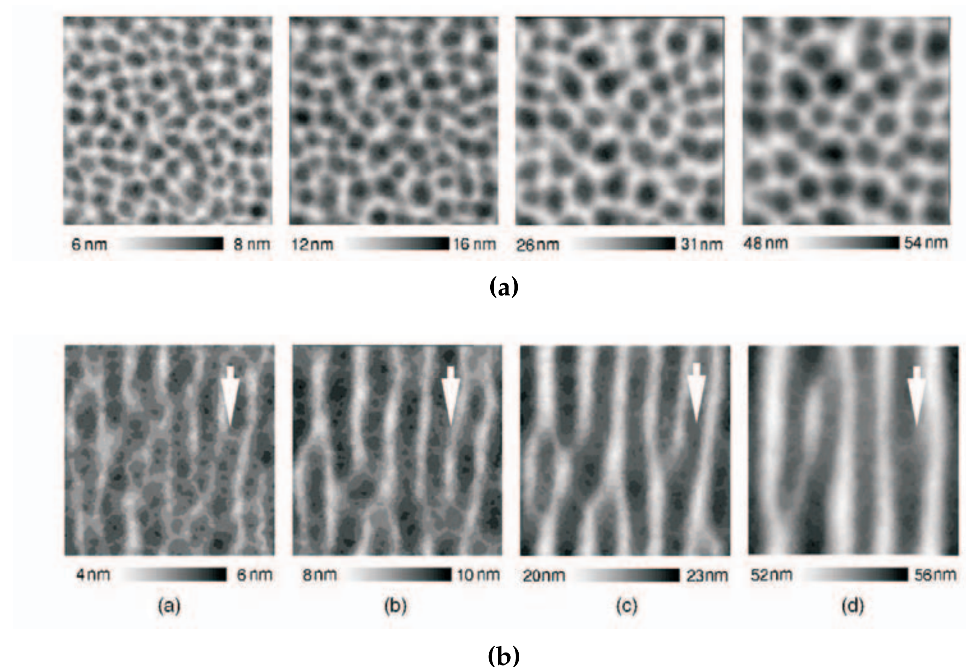

Figure 2.10: Simulated 100 nm $\times$ 100 nm surface morphologies for Cu bombarded by 1 keV ions at (a) normal incidence and (b) 80 ° incidence. Image from [71].

The simulations demonstrate that the angle of incidence of the ion beam determines the geometry of the nanostructures on the Cu surface. At normal incidence, the pattern is shaped as a network of partially interconnected hillocks, and at grazing incidence arrays of ripples directed along the surface projection of the Ar ion beam self-assemble. The size of the surface features shows a pronounced dependence on the ion flux, and

the predicted trends imply that ion beam sputtering is a controllable way to produce surface nanostructures. The results of simulations are shown in fig. 2.10.

2.5 Metals

Particular attention should be devoted to the case of metals. Due to their higher diffusivity with respect to semiconductors and amorphous materials and to the non-directional character of the metallic bond, ion impact does not imply amorphisation of the surface. The main effect associated with the impact of a single ion is the production of monoatomic-height adatom and vacancy clusters. It has been experimentally confirmed that even after prolonged sputtering the crystalline quality of the substrate is not affected much[77]. In the case of metals, the surface pattern is produced by two different mechanisms: the surface curvature dependence of ion sputtering and the presence of an extra energy barrier, the Ehrlich-Schwoebel barrier, when the diffusing atoms try to descend step edges.

Valbusa *et al.* [78] observed the effect on Ag(110) for different temperatures. Their results are shown in Figure fig. 2.11. They found out that ripple morphology is greatly dependent on the temperature of the substrate. At low temperatures (T<230 K) the surface was rough, without any evidence of organization. At a temperature of 230 K ripple structures appeared, aligned along <001>. At higher temperatures (around 270 K) the structure evolved first into an array of rectangular mounds, for even higher temperatures (290 K and 320 K) the ripple structure was aligned along <1$\bar{1}$0>. At the highest temperature explored (350 K) the surface tends to smoothen, losing the ripple morphology.

The structures produced in the case of metals have a different nature than those observed on amorphous materials. The main characteristics of ion sputtered surfaces of metals can be summarized as follows:

- Structures are also produced by bombardment at normal incidence, while this condition forms no ripples on non-metalic substrates
- Ripple orientation and wavelength depend on the temperature
- Ripple wavelength depends on the ion fluence

In the case of Ag(110) shown in fig. 2.11, anisotropic surface diffusion is responsible for these effects. The surface temperature changes the relative magnitude of the two diffusion rates and so plays a key role in determining the ripple orientation.

Neither the Bradley - Harper model [19] nor its linear extension by Makeev, Cuerno and Barabasi [79, 80], who added non-linear terms to account for the anisotropic surface diffusion, explains all the phenomena observed. This is because the contribution of the diffusive term is oversimplified in all cases. What needs to be done is to introduce

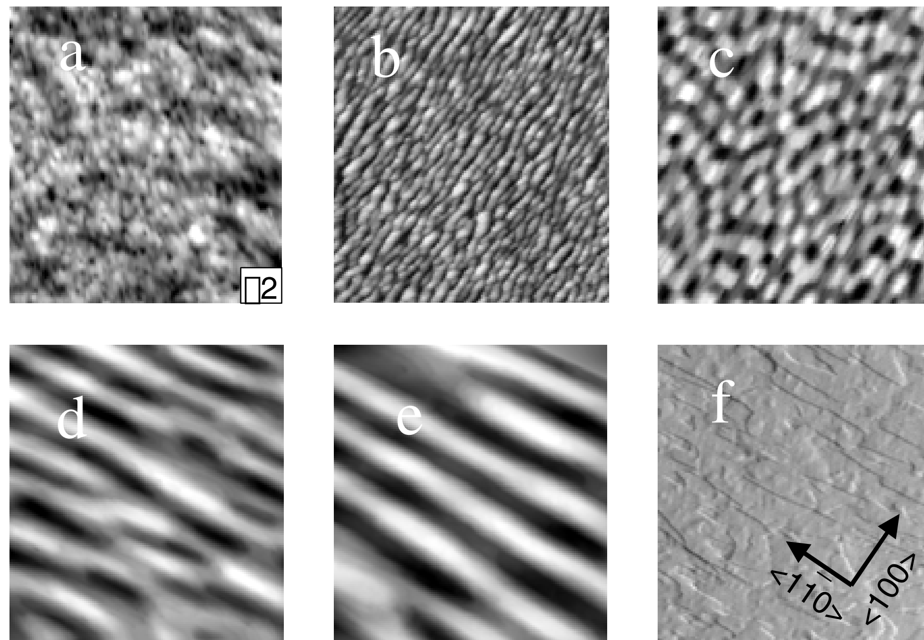

Figure 2.11: AFM images of Ag(110) after ion sputtering at normal incidence for different temperatures: a) 160 K, b) 230 K, c) 270 K, d) 290 K, e) 320 K, f) 350 K. The size of the images is 350 × 350 nm^2. [15]

different diffusion terms for each principal surface direction and assume that this term depends exponentially on the temperature.

There are two contributions to the diffusion term: one is thermal diffusion, which tends to move atoms from hills to valleys, and the other one is diffusion arising from the Ehrlich-Schwoebel barrier, which moves atoms uphill [81]. It should be noted that amorphous materials do not have an Ehrlich-Schwoebel barrier and also no preferred diffusion direction. This model is quite good at explaining the phenomena observed on metal surfaces.

At normal incidence and low substrate temperatures, an erosion mechanism alone would result in a rough and unstructured surface morphology. However, the activation of the terrace diffusion barrier and the Ehrlich-Schwoebel barrier opens the possibility for the development of surface instability connected with ripple formation.

The mechanism of temperature dependence on ripple formation will be much clearer when explained using the example of Ag(110), as it is shown in fig. 2.11. At low temperature (160 K) the surface is rough since the mobility of adatoms and vacancies is very low. At temperatures around 230 K, ripples appear along <001> direction. The mobility sets in first along the <1$\bar{1}$0> direction and the adatoms are not able to descend the steps due to the Ehrlich-Schwoebel barrier in that direction. As the temperature is increased to 270 K, mobility also occurs along the <001> direction and the adatoms are

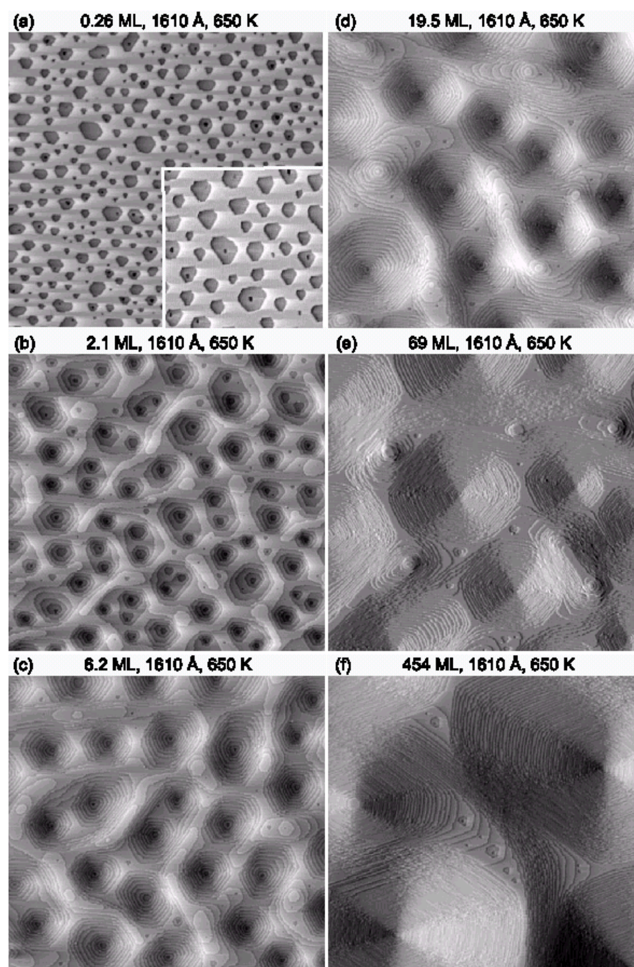

Figure 2.12: STM topographies after normal angle ion erosion of Pt(111) at 650 K. The removed amount of material (in monolayers) is indicated, as well as the temperatures and the image scales. The inset in (a) is shown at higher magnification [82].

also affected by the barrier along <001>; so instead of ripples, mounds form, because Ehrlich-Schwoebel barrier is now present in both directions. At even higher temperatures, the adatoms can descend the steps first along <1$\bar{1}$0> and ripples are formed along this direction. When the temperature is high enough (above 350 K) adatoms can efficiently descend the steps along <1$\bar{1}$0> and <001> and thus the surface becomes smooth and loses its ripple structure.

As this experiment [15] shows, it is possible to produce a regular array of nanostructures on single-crystalline metal surfaces whose orientation is determined by the dominant diffusion direction. For this reason we call the set of conditions in which these nanostructures appear the *diffusive regime*. In this regime, which is characterized by incident angles near normal and high substrate temperature the diffusion of the produced ad species proceeds at a rate which is fast in comparison with the impingement

rate of ions, so the structure of the unit cell tends to be reflected in the orientation of the nanostructure, as fig. 2.12 shows. The erosive sputtering regime is achieved only for grazing incidence sputtering geometry (incidence angles above 70°) and low substrate temperatures in order to inhibit thermally activated diffusion processes, which tend to smoothen the surface. These two regimes are presented in fig. 2.13.

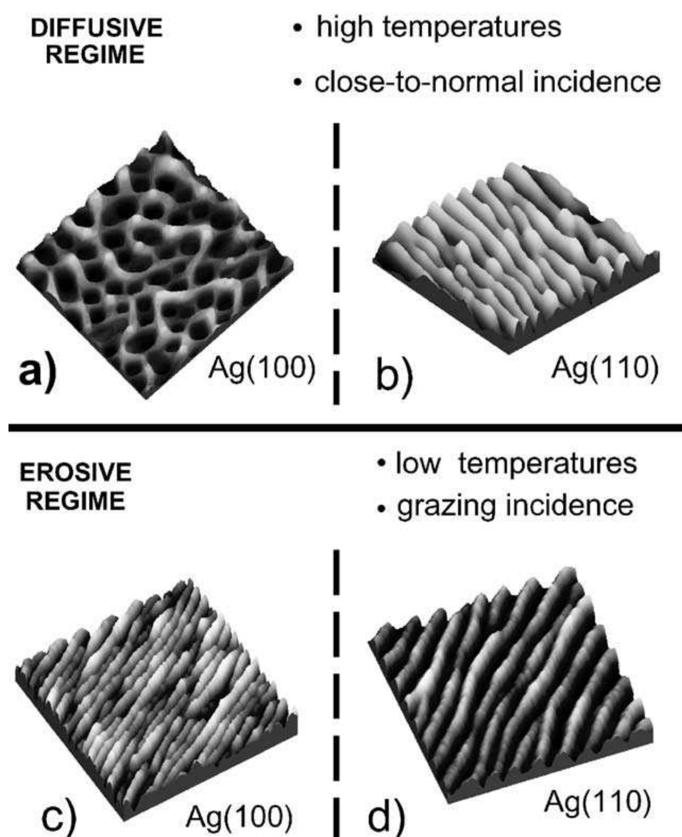

Figure 2.13: Diffusive and erosive regimes and the surface morphologies produced in each of them. [15]

In the 1980's,G. Carter and his colleagues [17] provided an extensive report on sputtering induced topography development on f.c.c. metals (Cu, Ni,Pd, Ag and Pb). They provide a classification scheme on three levels: first, there is the distinction (in polycrystals) between *intragranular* and *intergranular* features. Within the intragranular category (which is valid also for single crystals) there is a distinction between *elevated* and *depressed* features, relative to their immediate surrounding. Finally, the authors propose a distinction between *isolated* and *repetitive* features, where isolated features are sometimes found on all grains and repetitive features are confined to specific grains. Due to different near surface energy deposition during the sputtering process, single crystal materials of different orientations sputter at different rates. Therefore, during ion beam erosion of polycrystalline materials the relief that develops can be different in each grain, depending on the grain orientation. In many situations the *grain boundary*

area is delineated by quite steep intergranular boundary faces or zones, as is shown in fig. 2.14.

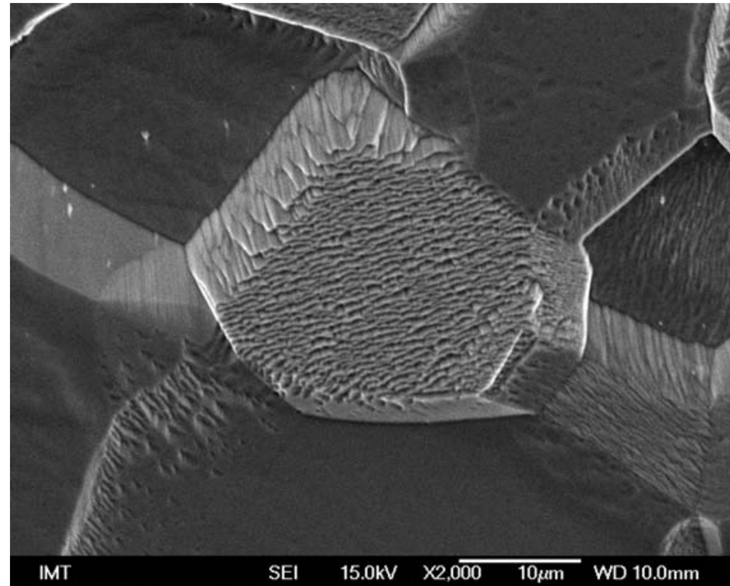

Figure 2.14: Example of grain boundary area: illustration shows differential sputtering of different grains and a steep intergranular boundary. The material is polycrystalline FeSiAl alloy. In this image we can also distinguish between elevated and depressed features.

According to Carter *et al.* [17], the distinctive nature of each crystal face in a polycrystaline material appears to depend not only on the surface orientation of the associated grain, but also on its immediate surrounding. The authors suggest that such effects arise from either or both differentially enhanced erosion of dislocated networks which intersect the grain boundary related interfaces and facetting of a surface to produce more stable, erosion resistant set of surfaces as it is suggested by the theory of sputtering erosion.

Another point of interest is the formation of so-called *etch pits*. Such structures were reported in early literature on cathodic sputtering and were employed for delineation of dislocations at surfaces [83, 84]. They appear in isolation, in profusion and sometimes, after considerable bombardment, inseparable since they have grown and overlapped to form rather continuous corrugated, faceted structures. The pits developed on individual grains possess a geometrical habit which is grain-orientation dependent. In a way this is similar to chemical etching phenomena, where the pits and their shapes can be utilized to gather information about orientation of a certain grain [85]. An example of triangular etch pits formed on the surface of FeSiAl alloy is shown in fig. 2.15.

Because surface crystallography has a determining effect on the pattern formed, it is generally believed that the pattern formation of this type is related to surface diffusivity. In the literature, this type of behavior has been related to diffusion over step edges

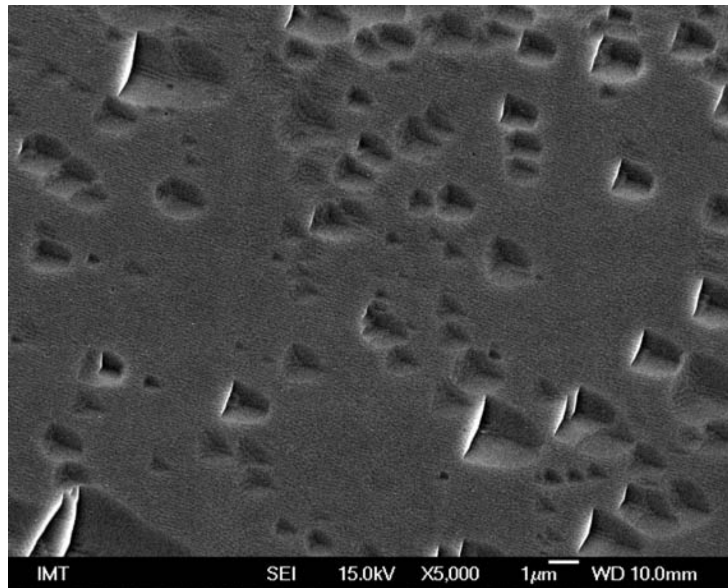

Figure 2.15: Example of triangular etch pits in a grain of FeSiAl alloy.

[40, 20]). This type of surface patterning has been explored on Pt(111) [86, 87], Au(111) [88, 49, 89, 90], Ag(100) and (110) [91, 92], among other systems.

2.6 Possible applications of ion beam nanostructured surfaces

Ion beam sputtering allows a controlled modification of surfaces - their structure, roughness, and along with that also chemical, optical and physical properties. It is possible to extend the patterning of substrates from expensive model systems (single crystal substrates) to technologically relevant classes of materials like polycrystalline metal films and grained bulk metals. The possibility to produce regularly spaced quantum dots [93, 94] on Si and other semiconductor substrates leads to possible applications in device fabrication for quantum computing. As there are many potential uses for ion beam nanostructured surfaces, I will review only a small selection.

Ion sputtered surfaces as templates for alignment and ordering

Many future opto- and nanoelectronic devices are based on well-organized arrays of quantum dot structures. The nanometer scale of such structures is beyond conventional litographic techniques, so nanopatterning of the surface can be attempted by using a high resolution technique (for example, by using a focused ion beam) or by employing the natural self-organization processes, which can be utilized on a large scale (full wafer) and have the advantage of low cost.

Many groups report on the production of ordered quantum dot arrays by using ion beam sputtering. Ronda *et. al* [95] propose a two-step process based on Si substrate nanopatterning by means of an ion beam and a self-assembly of Ge dots on top of surface instabilities in a second step. They observe Ge dots ordering along the substrate undulations due to step and strain effects. Similarly, Facsko *et al.* [96] achieved an ion-induced formation of regular nanostructures on amorphous GaSb surfaces, using commercially available GaSb wafers and sputtering them with low energy Ar ions at normal incidence, resulting in a regular array of nanodots.

Attempts have also been made to use ion beam structured surfaces as templates for carbon nanotube alignment [97]. The authors deposited a carbon nanotube solution on ion beam sputtered quartz substrates and studied the alignment and compression of carbon nanotubes. The nanotubes placed themselves transversely with respect to the ripples and were often tied up with heavier elements, such as metal particles or amorphous carbon particles. The nanotubes were able to follow quite rough topographies. The authors also measured the degree of rope radial compression and the value is quite high, up to 75%; which is higher that the value associated with ropes crossing on flat surfaces.

Modifying chemical reactivity by ion beam sputtering

By controlling the density and nature of defects present on surfaces, it is possible to control also their chemical reactivity. Surface structures strongly affect the reaction barriers for relevant chemical processes, for example C-H bond activation of ethane on Ir(111) [98, 99]. The possibility to tune the density of atomic steps and their orientation is the key issue to tailoring chemical reactivity of the surfaces. By ion beam sputtering it is possible to produce defects (atomic steps) of a well-defined type (orientation) and density.

Studies were performed on dissociation of O_2 on Ag(001) nanostructured surfaces in the erosive regime [100]. For the otherwise inert Ag(001) surface significant O_2 dissociation takes place on the nanostructured surface, thus allowing us to control the relative coverage of admolecules and adatoms. The dissociation probability is determined by the experimentally tunable density of kinks.

Similarly, rhomboidal pyramids formed on Rh(110) surfaces have been shown to assist in CO dissociation on the surfaces. On a flat Rh substrate the CO dissociation is negligible on close packed (111), (110) and (100) surfaces but it is increased on stepped (211) and (210) surfaces. However, XPS measurements of CO dissociation [101] on Rh (110) pyramids produced by Xe ion beam sputtering in the diffusive regime show that the Rh nanopyramids can induce dissociation of CO, which would otherwise desorb intact on the (110) teraces. The most probable reaction site for CO dissociation is an on-top configuration at the kinked step edges where Rh atoms have the lowest coordination.

Tuning magnetic properties of thin films

Ultrathin magnetic films are among the first examples of nanosized magnetic systems. The atomic environment affects the local magnetic properties of interface atoms. By reducing the film thickness below a few tens of monolayers, the contribution of interface atoms to the magnetic properties of the film becomes relevant [102, 103, 104]. As ion beam nanostructuring is a versatile technique to induce self-organisation in the nanoscale domain, also low-energy ion sculpting has been applied to tune the magnetic properties of Co/Cu(001) and Fe/Ag(001) thin film systems [105, 106]. The ripples that formed are similar to the ones that are expected on single-crystal substrates. The authors performed Magneto-optical Kerr effect studies (MOKE) to characterise the magnetic hysteresis of the films, depending on the ion fluence. It has been shown that ion beam sculpting induces profound modifications in the magnetic anisotropy of both systems.

3
Aims and hypothesis

Ion bombardment has recently attracted much attention as a tool for inducing self-organized patterns on various metal, semiconductor and amorphous surfaces as a viable alternative to lithographic processes in the nanoscale domain. An extensive range of experiments has been reported on single crystal, amorphous and semiconductor materials, while little is known about the effect grains and grain boundaries play in the self-organization process in thin polycrystalline films and bulk materials. Additional minute concentrations of surface active elements could act as driving forces in the pattern formation.

Ion beam sputtering leads to surface modifications in terms of pattern formation. The pattern that forms is a direct result of an interplay between different instabilities and driving forces: Bradley-Harper instability, Ehrlich-Schwoebel barrier, surface diffusivity and mass transport. By controlling all these, it is possible to tailor the resulting pattern in terms of ripple wavelength, ripple height, lateral ordering and orientation of the slope.

With this dissertation, we aim to expand the scientific knowledge in the field of ion beam induced surface modifications by examining the role that grains, grain boundaries, mass transport across grain boundaries and surface active elements play in the formation of patterns. Experiments were performed on thin film systems, Fe single crystal surfaces and FeSiAl alloys. Two different compositions of FeSiAl alloys were used, one contained

an addition of surface active element Se, and the other composition was without Se. Both alloys contained similar amounts of P and S.

The main aims of this thesis were the following:

- Experimental determination of the evolution of thin film (Au), single crystalline Fe and polycrystalline FeSiAl alloy surface morphology during ion beam sputtering and understanding the processes that govern the surface diffusivity.
- Experimental determination of the effect of crystallite orientation on the formation of ion-beam induced nanostructures.

This thesis up to the date of defense also directly resulted in (accepted) publication of four articles: two on thin film systems [107, 108] and two on FeSiAl alloys [109, 110]. Some of the thesis content was also presented at international and national conferences.

4 Experimental

The majority of the experimental work was performed at the Institute of Metals and Technology in Ljubljana, under the supervision of my mentor, Prof. Dr. Monika Jenko. Sputtering of polycrystalline thin films was done at the Univerity of Genova, Department of Physics, under the supervision of Prof. Dr. Francesco Buatier de Mongeot in the scope of the bilateral Slovenian - Italian project "Grande rilevanza". Atomic Force Microscopy facilites were kindly provided by Prof. Dr. Dragan Mihailović of Jozef Stefan Institute, Complex Matter (F5) department.

4.1 Materials

I performed sputtering experiments on three different material types: polycrystalline bulk materials, single crystal materials and polycrystalline thin films. As polycrystalline bulk materials FeSiAl alloys (also known as electrical or silicon steels) of two different compositions, one with a minor addition of surface active element Se and the other with no additional Se, were used. The S and P content are approximately the same in both compositions. The single crystal substrates were α-Fe(100) and αFe(110), as well as Fe-10% Si single crystals in b.c.c. structure with (100), (111) and (110) orientations. Gold thin films were produced in three different ways to obtain a different starting structure, namely different grain sizes and roughness of the film.

4.1.1 Gold films deposited on glass

The thin Au films used in the experimental work were grown by two different physical vapour deposition (PVD) processes: sputter and thermal deposition, as is depicted in fig. 4.1. The two distinctly different methods of the film growth lead to differences in the film topographical features, which are in details explained in section 5.1.

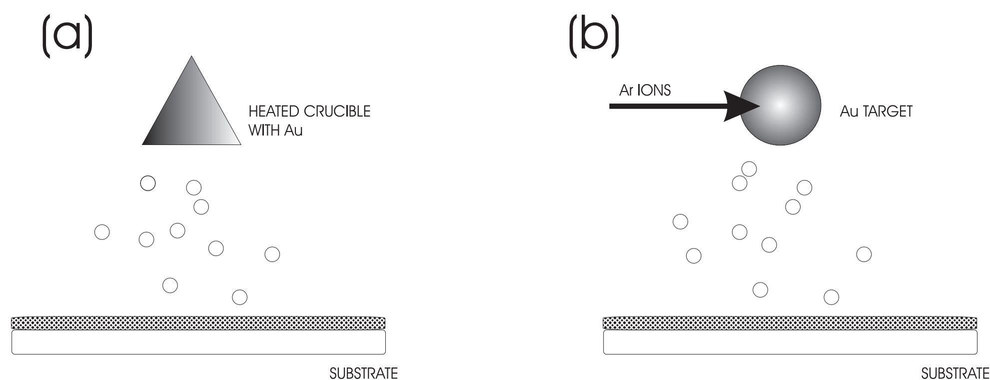

Figure 4.1: Schematic representation of film growth methods: (a) thermal deposition of the film, (b) sputter deposition of the film.

The films were deposited on glass microscope cover slides, which were first cleaned in alcohol and acetone and immersed in an ultrasonic alcohol bath for 10 minutes. The slides were then dried and a gold film of desired thickness was applied. For sputter deposited films, the Gatan Precision Etching and Coating System (PECS) was used with the following ion beam parameters: ion energy 10 keV and ion beam current 300 μA, which led to a deposition rate of about 18 nm/min. The Au target had 99.99% purity. Thermal deposition of the specimens was performed in a dedicated UHV system with a slower deposition rate of 6 nm/min.

4.1.2 FeSiAl alloys

For polycrystalline metal substrates I used FeSiAl alloys, also known as electrical steels. This steel type is tailored to produce certain magnetic properties, such as a small hysteresis area and high permeability, and it is used for transformer cores and stator and rotor components of electrical motors.

The experimental alloy was produced in a laboratory vacuum-induction furnace, hot formed and then finally cold formed into a steel sheet of 0.15 mm thickness. The steel sheet was decarburized in a H_2/H_2O gas mixture at 840 °C for 20 minutes. I used two different steel compositions, which are given in table 4.1.

Table 4.1: Composition of FeSiAl alloys used in the experimental work (in mass percent)

composition	C	Si	Al	Mn	P	S	Se
A	0.035	1.66	0.831	0.199	0.0029	0.0028	0.050
B	0.042	1.73	0.853	0.208	0.0022	0.0020	-

The specimens were ground with emery paper up to number 4000 and then polished with 3 µm and 1 µm diamond paste. After cleaning with alcohol, the specimens were immersed in an ultrasonic alcohol bath for 10 minutes. The duration of the bath was timed and was kept the same for all specimens. A polished surface of the specimen as seen by optical microscopy is given in fig. 4.2, where a smooth surface with some inclusions can be seen.

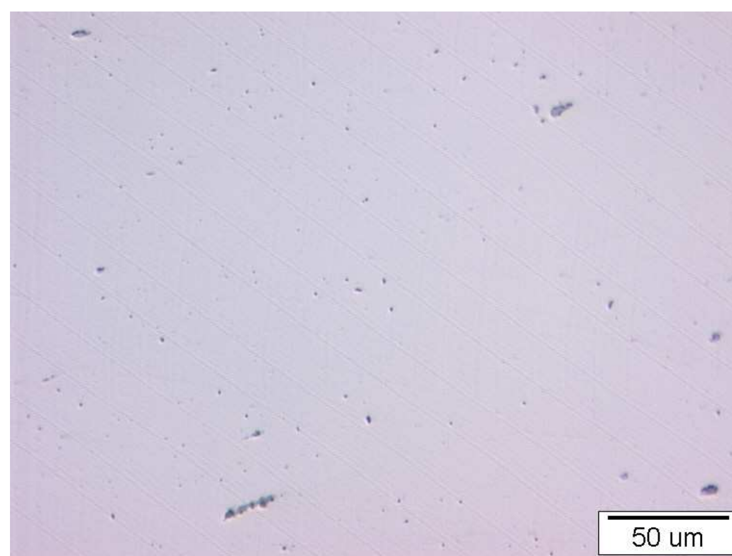

Figure 4.2: The polished steel specimen as seen by optical microscopy.

4.2 Sputtering

Sputtering experiments on thin film specimens were performed at the Department of Physics, University of Genova, Italy. The films were exposed to Ar^+ ion beam irradiation at an off-normal sputtering angle of $\theta = 80°$, measured with respect to the surface normal. The ion flux was constant 5.5×10^{14} ions/cm^{2}s. The surface temperature was stabilized at around T $\approx$ 300 K by means of a liquid nitrogen cooling system. The ion fluence was varied in the range between θ=6.2$\times$10^{17} ions/cm^2 and 1.7$\times$10^{18} ions/cm^2. The experimental system is depicted in fig. 4.3.

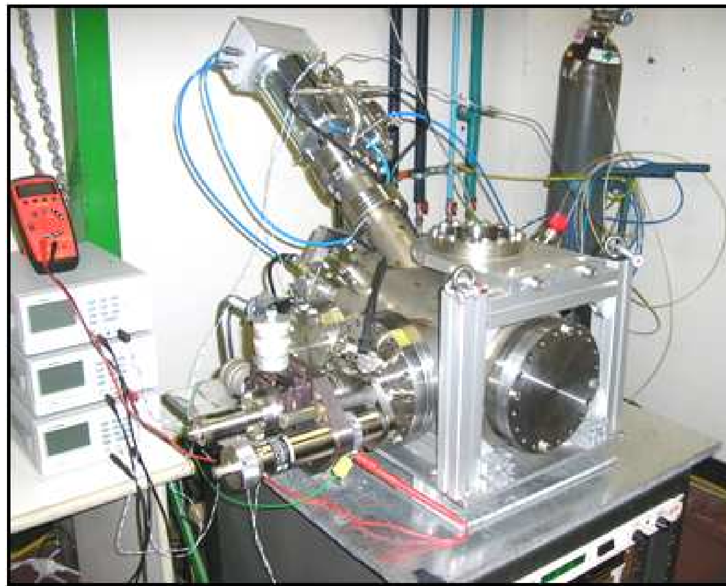

Figure 4.3: The ion beam sputtering system at the Genova Department of Physics, where thin film sputtering experiments were performed.

The bulk specimens were sputtered by Ar^+ ions in a Gatan Precision Etching and Coating System (PECS 682) at the Institute of Metals and Technology in Ljubljana. The system comprises a vacuum chamber, an ion gun for sputtering purposes and two additional ion guns for coating applications. The ion guns are the Penning ion gun type with miniature rare earth magnets. The system is depicted in fig. 4.4. The specimen was positioned on a sample holder and inserted into the system. There was no additional outside heating or cooling of the specimen.

The sputter gun was operated in the range of 6 keV to 10 keV energy and the ion currents were in the range of 150 μA to 500 μA. The chamber is constructed in such a way that it is also possible to etch tilted specimens. A range of tilts between normal incidence and 80° from normal was explored. The irradiation area at normal incidence sputtering conditions has been measured at 6 keV and 10 keV ion beam energy and 350 μA current using a Si wafer. The diameter of the etched circular spot on the surface is 9 $\pm$ 0.5 mm in the case of 10 keV and 8.5 $\pm$ 0.5 mm for the 6 keV beam energy. The area specified

Figure 4.4: Gatan PECS system, which was used for ion beam sputtering of the bulk specimens.

in the manual of the instrument [111] is in good agreement with this measurement, as the technical specifications state that the etched area ranges from 7 mm to 10 mm, depending on the ion gun energy (1.0 keV to 10.0 keV). All doses can be calculated using the irradiation area provided with this experiment and the specified ion beam currents along with etching time, according to the following formula:

$$D = \frac{It}{e_0 S} \tag{4.1}$$

$$S = \frac{S_{irr}}{\cos\theta} \tag{4.2}$$

where I is the beam current, t the etching time, e_0 elemental charge ($e_0 = 1.6 \times 10^{-19}$ C), and S stands for the irradiated area, corrected for tilt as in Equation 4.2.

4.3 Characterization of resulting structures

The patterns formed due to ion beam irradiation were characterized employing a multi-technique approach. I used field-emission scanning electron microscopy (FE-SEM) to visualize the surface on a larger scale as well as atomic force microscopy (AFM) for the detailed measurement of surface corrugation, ripple wavelength and other characteristics. With electron backscatter diffraction (EBSD) I was able to connect the texture and local crystalline orientation measurements with the resulting surface structures. In this section, I will review the basic principles of the instrumentation used.

4.3.1 Atomic force microscopy

The atomic force microscope was developed in 1986 by Binning, Quate, and Gerber [112] as a collaboration between IBM and Stanford University, and since then wide uses for this technique have been found in materials science [113]. It's main advantage over other imaging techniques is that it provides real topographic information: as the cantilever tip is scanned along the surface, the displacement of the tip due to Van der Waals forces reflects the real topography of the sample. Small vertical displacements of the tip are detected by using a laser spot reflected from the top surface of the cantilever into an array of photodiodes. There are three primary modes of AFM operation; contact mode, non-contact mode and tapping mode. Each of these modes has certain advantages and disadvantages and depending on the specimen properties the optimal mode is selected.

For this work, I chose non-contact mode AFM, where the cantilever is oscillated at a frequency which is slightly above the cantilever resonance frequency. The tip does not come in contact with the sample surface, but it is instead oscillated above the sample. This way, there is less possibility for the damage of either the specimen or the tip. The instrument I used was Veeco DiInnova-SPM, which was kindly provided by Prof. Dr. Dragan Mihailović at the Jozef Stefan Institute. I used standard non-tapping mode Veeco TESPA tips with Al back coatings.

Image analysis

The AFM images obtained are 512x512 numerical matrices giving information about surface topography. Image analysis was performed by scanning probe image analysis software, **WSxM** [114], free ware available from Nanotec Electronica.

To estimate the roughness induced by the ion beam, I used the *root mean square (RMS) surface roughness*, S_q, which is defined as

$$S_q = \sqrt{\frac{1}{MN}\sum_{k=0}^{M-1}\sum_{l=0}^{N-1}[z(x_k, y_l) - \mu]^2}. \tag{4.3}$$

Here, $z(x_k, y_l)$ is the height and μ is the mean height value taken across all in-plane coordinates (x, y):

$$\mu = \frac{1}{MN}\sum_{k=0}^{M-1}\sum_{l=0}^{N-1} z(x_k, y_l). \tag{4.4}$$

To obtain information about image periodicity, I used the *selfcorrelation function*, an image transformation that is sensitive to the presence of periodic structures on the surface. The two-dimensional autocorrelation function is defined as

$$G(k_1, k_2) = \sum f(x, y) \times f(x + k_1, x + k_2), \tag{4.5}$$

where $f(x, y)$ is the image matrix. Essentially, the self-correlation function takes the image and the same image shifted for (k_1, k_2), where (0, 0) would be the center of the matrix. The resulting image, $G(k_1, k_2)$, is a measure of how different the two images are. Any periodicity in the original image will be shown as a periodic pattern in the self-correlation. A 2-dimensional sinusoidal wave of 88 nm periodicity and the corresponding self-correlation image is given in fig. 4.5. In the self-correlation image, the wavelength of the periodic structure is then defined as the distance between the central and the first order peak, and the two first-order peaks are separated by a distance of 2λ, as is shown in fig. 4.6.

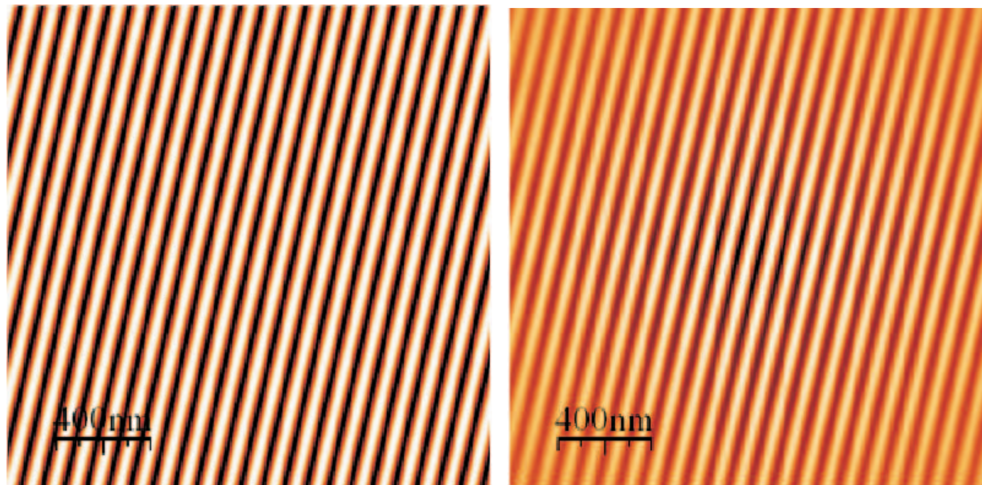

Figure 4.5: A two-dimensional sinusoidal wave and the corresponding self-correlation function.

In the self correlation function of a perfect sinusoidal wave one can observe a slow decay in the case of line profile along the ridges. However, when dealing with real surfaces,

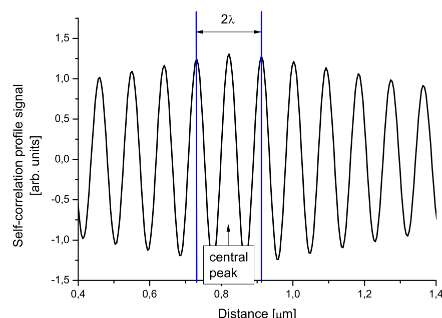

Figure 4.6: Wavelength definition as obtained from self-correlation function. The profile is along the self-correlation image shown in fig. 4.5, where the sinusoidal wavelength is 88 nm.

where the ripples are not a perfect wave, it is not possible to get so many peaks in the self-correlation profile. Still, the definition holds: the two first order peaks are separated by a distance corresponding to two wavelengths (2λ).

Another way to estimate the periodicity of the resulting ripples is via the two-dimensional Fast Fourier Transformation (2D FFT). The Fourier Transform is a series expansion of an image function (in this case over the 2D space domain) in terms of "cosine" image (orthonormal) basis functions.

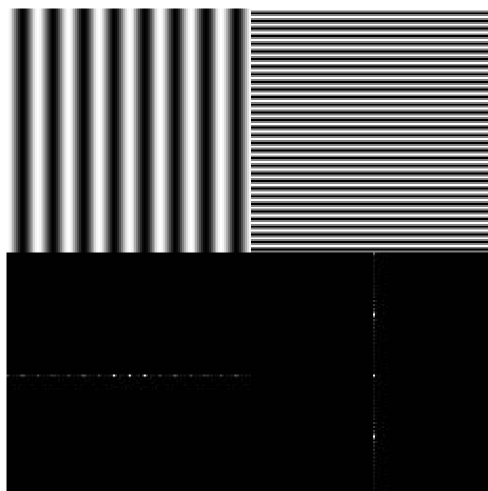

Figure 4.7: Horizontal and vertical cosines and their corresponding 2D FFTs.

Two periodic patterns with their Fourier Transforms shown underneath are depicted in fig. 4.7. The images are a pure horizontal cosine of 8 cycles and a pure vertical cosine of 32 cycles. In this case, the Fourier transform of each has a single component, represented by two bright spots symmetrically placed about the center of the FT image. The center of the image is the origin of the frequency coordinate system. In both cases there is a dot at the center that represents the (0,0) frequency term or average value of the image.

The distance between the two spots corresponds to $1/k$, where k is the wave vector, and the correspondence between the wavelength λ and the wave vector k is the following:

$$k = \frac{2\pi}{\lambda} \tag{4.6}$$

Another example is given in fig. 4.8, where an 88 nm sinusoidal function (the same as in fig. 4.5) and the corresponding 2D FFT is given.

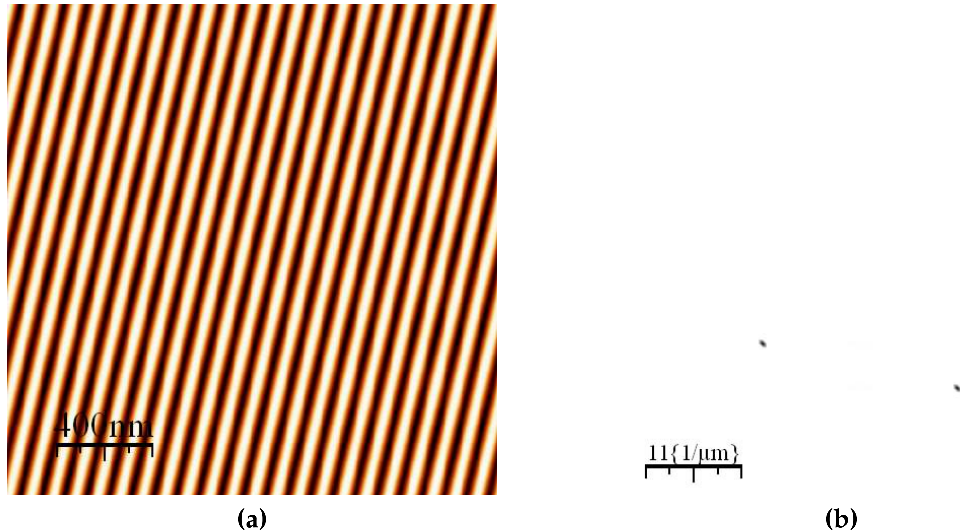

(a) (b)

Figure 4.8: An example of 2D FFT as was performed for "real" AFM images. The image is an 88 nm wave, and the corresponding 2D FFT shows that the distance between two peaks is in fact 22.62 $1/\mu m$, which is 88 nm wavelength.

In this work, I used the 2D FFT and the self-correlation image transformations provided in the WSxM software package.

4.3.2 Scanning electron microscopy with EDS/WDS techniques

Scanning electron microscopy enables visualization of the surface at different magnifications by rastering an electron beam across the surface of the specimen. The instrument used in the experimental work was a JEOL JSM 6500-F scanning electron microscope, with an add-on retractable backscatter electron detector and equipped with the following analytical techniques: Energy dispersive spectroscopy (EDS), Wavelength dispersive spectroscopy (WDS) and Electron backscatter diffraction (EBSD).

The main components of the scanning electron microscope are the electron gun, the electron column, the specimen chamber with detectors and the vacuum system. The electron gun is a Schottky field emission type. The main advantages of Schottky field emission guns are high brightness, long lifetime, and stable beam current along with a small probe size (a few nanometers in diameter). The electron column consists of lenses and apertures that are used to focus the electron beam on the surface of the specimen. By rastering (scanning) an electron beam over the surface of the specimen a two-dimensional image is formed. The specimen is placed in the specimen chamber, which also contains detectors for the numerous signals generated by the electron-specimen interaction. The vacuum system is also a crucial part, generating a pressure of about 10^{-4} Pa in the specimen chamber. Also available on the market are variable pressure and low pressure Scanning electron microscopes, which can be operated at higher pressures.

The detectors I used on the SEM are the following:

- **Secondary electron detector** is a detector that collects electrons. The contrast in an image arises from the beam - specimen interactions that are different from one location to another. The electronics of the detector convert the signal to point-by-point intensity changes on the viewing screen, thus producing an image.
- **Backscattered electron detector** collects backscattered electrons and uses them to generate an image of the specimen. Backscattered electron imaging provides image contrast on the basis of elemental composition. Lighter elements generate fewer electrons and appear darker in the image.
- **Energy dispersive spectroscopy - EDS** detector is a solid state detector for detection of the generated X-rays. The energy deposited by an individual incoming X-ray is measured. An X-ray spectrum shows characteristic peaks of elements at given energy positions.
- **Wavelength dispersive spectrometer - WDS** is a crystal detector operating on the principle of Bragg's law of diffraction for the detection of generated X-rays from the specimen.

- **Electron backscatter diffraction - EBSD** is a special camera that collects diffracted electrons from a tilted specimen to form a diffraction pattern that is used in the determination of surface cyrstal properties. A short description is given in section 4.3.3.

Figure 4.9 shows the scanning electron microscope used for the experimental work in this thesis. The add-on detectors are labeled. The secondary electron detector is positioned in the specimen chamber.

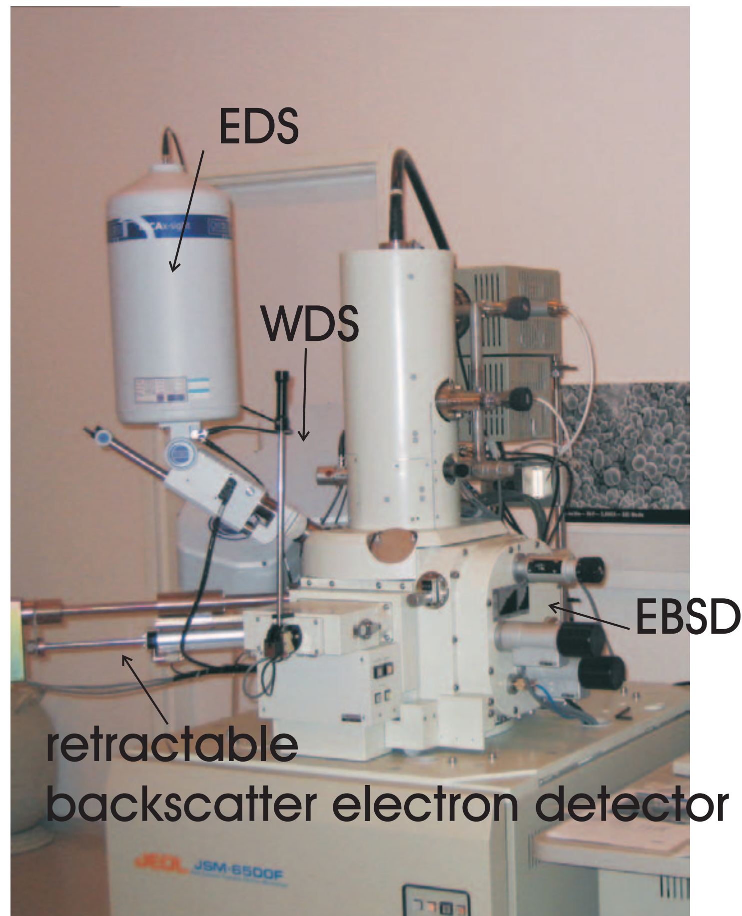

Figure 4.9: The scanning electron microscope used for experimental work.

4.3.3 Electron Backscatter Diffraction - Crystallographic Information in the Scanning Electron Microscope

Electron Backscatter Diffraction (EBSD) is a powerful SEM-based technique which allows one to obtain crystallographic as well as phase information. EBSD is a surface sensitive technique, the diffraction signal coming from the top few nanometers of the crystal lattice. With the latest Field emission electron gun SEMs the EBSD technique can achieve a spatial resolution in the range of 10 nm.

The pattern is generated by illuminating a highly tilted specimen with a stationary electron beam. It consists of many intersecting, linear features called "Kikuchi lines", which consist of a strip, brighter than the background, bounded by two edges. Fundamental physics of pattern formation is not yet well understood, but the most likely description is the following [115]:

1. Electrons strike a sample surface, and are inelastically scattered within a pattern source point, which leads to a little line broadening.
2. Scattering events cause electrons to scatter in all directions within a small volume.
3. Intensity variations are caused by channeling of electrons satisfying the Bragg Diffraction condition for a particular lattice plane
4. These diffracted electrons form two cones, which intersect a flat scintillator to form hyperbolae. These are called Kikuchi lines (Kikuchi bands).

To view the diffraction pattern a special EBSD detector unit consisting of a phosphorous screen and a low light camera connected to a computer with a frame grabber is used. Powerful software then analyses and indexes the obtained patterns. Automatic indexing is performed by first detecting the bands in the pattern by Hough transformation and comparing the pattern to a pre-defined set of possible crystallographic phases (MatchUnits). The automatic indexing procedure is depicted in fig. 4.10.

Besides indexing diffraction patterns, one of the more popular uses of EBSD is for the determination of micro texture. In crystallography, the term "**texture**" means a preferred orientation, that is the non-random orientation of single crystal lattices within a material. If a polycrystalline material has texture then that means that the orientations of crystallites are not uniformly distributed.

Texture is often visualized by constructing a so-called **pole figure** and **inverse pole plot**, in which a specified crystallographic axis (or pole) from each of a representative number of crystallites is plotted in a stereographic projection. A schematic diagram showing the processing of the crystal data and converting it into a pole figure and from there on in an inverse pole plot is shown in fig. 4.11

collect pattern
digitize pattern
Hough transform
position electron beam
detect bands and index
using pre-defined crystal structures

Figure 4.10: EBSD automatic indexing procedure.

Figure 4.11: Construction of EBSD inverse pole figure.

Another quite useful application of electron backscatter diffraction is the possibility to obtain orientation maps. To do this, an electron beam is scanned across the specimen surface, and each resulting EBSD pattern is indexed in real time. Powerful software (I used HKL Channel5 software for orientation mapping [116]) is then applied to generate an orientation map. Each map point is assigned a color that corresponds to the orientation of the crystal lattice at the given point. A recent review of the EBSD technique, its advantages and possibles uses in material science is given in [117].

5

Ion beam patterning of thin polycrystalline films

In most applications dealing with functional metal coatings, e.g. magnetic storage devices, integrated circuit interconnects, and advanced optical coatings, the metal overlayer is deposited in a polycrystalline form. Due to an intrinsic degree of disorder, connected to the presence of sub-micron grains with different sizes and also different crystallographic orientations, supported polycrystalline films have not been the subject of extensive ion beam sputtering experiments. However, some reports have shown the possibility of patterning polycrystalline thin metal films by means of a defocused ion beam [118, 119, 120, 121].

A crucial role in thin film systems is played by the initial surface morphology. The as-deposited film is not flat, but it exhibits considerable lateral and vertical corrugations in the form of individual grains. In the case of ion beam sputtering, this corrugation leads to a biased spatial distribution of the individual ion impacts at off-normal incidence sputtering because of the shadowing effects of large and tall grains. In addition to the initial roughness effect itself, the presence of grain boundaries could also play a role in the evolution of self-organized patterns, as the diffusion of adatoms and vacancies could be hindered by the grain boundaries.

As a model system for exploring pattern formation by a defocused ion beam we chose gold thin films deposited on a glass substrate and mica. To form a complete set of mea-

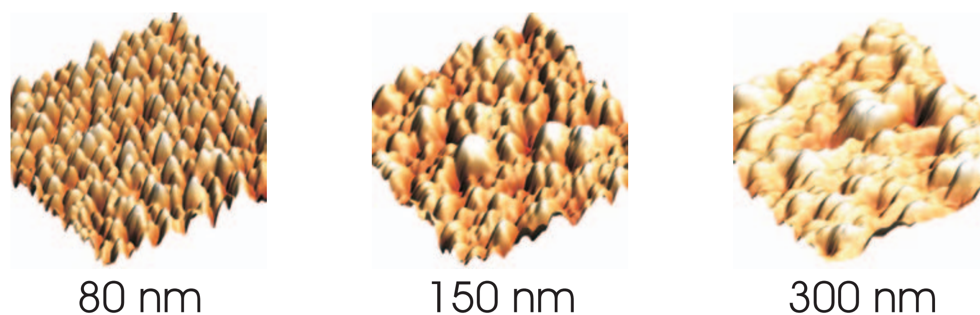

Figure 5.1: AFM images of three different film thicknesses, deposited by sputter deposition method. The image sizes are in all three cases 1 μm× 1 μm.

surements, three different starting films were employed. The main results of patterning polycrystalline metal thin films are given in this section.

5.1 Thin Au film growth

The thin Au films used in the experimental work were grown by two physical vapour deposition (PVD) processes (sputter and thermal deposition) and the third film employed in experimental work was flame-annealed Au 150 nm film deposited on cleaved mica substrate (acquired from SPI supplies). The deposition apparatus for the growth of PVD films and the deposition parameters have been already described in section 4.1.1.

Sputter deposited film thicknesses were monitored by a quartz crystal balance and later checked for consistency with a scratch test. I used a sharp needle to remove a portion of the film from the substrate and then verified the film thickness by AFM profile measurements. The measured thickness was about 20% different than the thickness shown by the crystal balance, so I used the AFM scratch test as a measure of real film thickness and prepared the films adjusting the nominal value of the film thickness. AFM images of films of three different thicknesses (80, 150 and 300 nm) are shown in fig. 5.1.

As the film thickness increases, the general trend is also an increase in average grain sizes and surface roughness [122]. The RMS surface roughness as a function of of Au sputter deposited film thickness is plotted in fig. 5.2. The data was obtained from five to seven AFM images of 1 μm × 1μm^2 size for each thickness and the shown error bars in the plot represent standard deviation of this data.

To obtain information about the film texture, EBSD measurements were performed and later confirmed by X-ray diffraction. EBSD data in fig. 5.3 shows the pole plots and an inverse pole plot in the normal (Z) direction obtained by orientation mapping of a 150 nm thin sputter deposited gold film, consisting of 30200 points. Since the grain sizes are below 100 nm (many even smaller than 50 nm) the map itself could not be used in the determination of the grain sizes or individual orientation of grains due to the technical

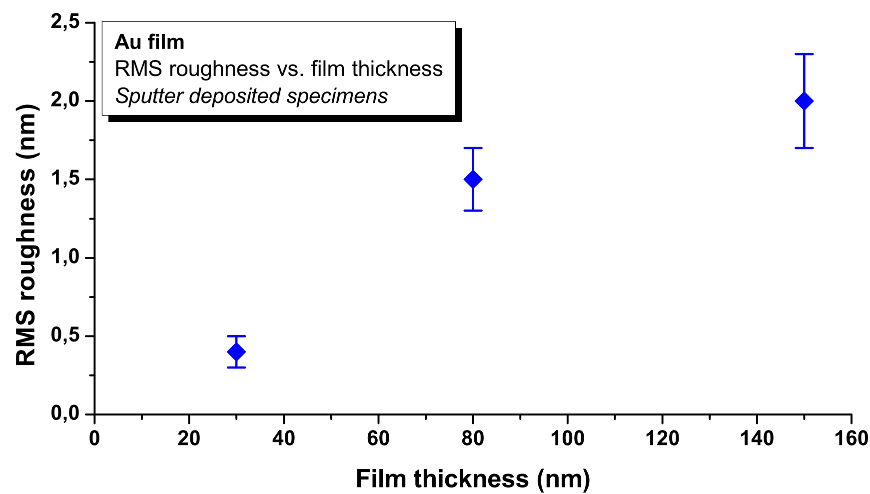

Figure 5.2: RMS roughness evolution of sputter deposited gold films. An increasing trend of surface roughness vs. the film thickness can be observed.

limitations of the EBSD technique and the specimen itself, but nonetheless the inverse pole plot shows a rather general trend that the film growth prefers (111) terminated grains. Similar results were reported in the literature, for example [123], where micro diffraction results for a 1 μm thick film of Au shows a strong preferred (111) texture normal to the film surface, and experimental data on 0.5 and 0.3 μm Au films show an even stronger preference for (111) grain growth. The pole plots in fig. 5.3c show that the material is strongly textured.

To confirm the EBSD measurement, I also performed X-ray diffraction, and the results are collected in fig. 5.4. Again, a large (111) peak can be seen in the diffractogram, with all the other peaks suppressed. There is also a very small (200) peak, and the (111) to (200) peak intensity ratio is about 170:1. The same holds for the thermally deposited specimen, which is also included in the fig. 5.4.

The d-value calculated from the XRD measurements corresponds closely to the d-value reported in PDF data No. 652870 for pure Au. The obtained d-value is $d = 2,351 \pm 0,005$ Å, while the standard d-value is $d = 2,3547$ Å. This holds for both specimens, and there is no significant difference in the (111) XRD peak position of the two specimens.

The films deposited by different PVD methods differ in initial surface morphology. Films prepared by the thermal deposition method exhibit a rougher surface and larger grain sizes compared to the sputter deposited specimens, along with a broader grain size distribution. These differences can be, to a certain extent, also attributed to different deposition rates. In the case of thermally deposited specimens, the deposition rate was about 3 times slower. Comparison of the surface morphologies of the two specimens

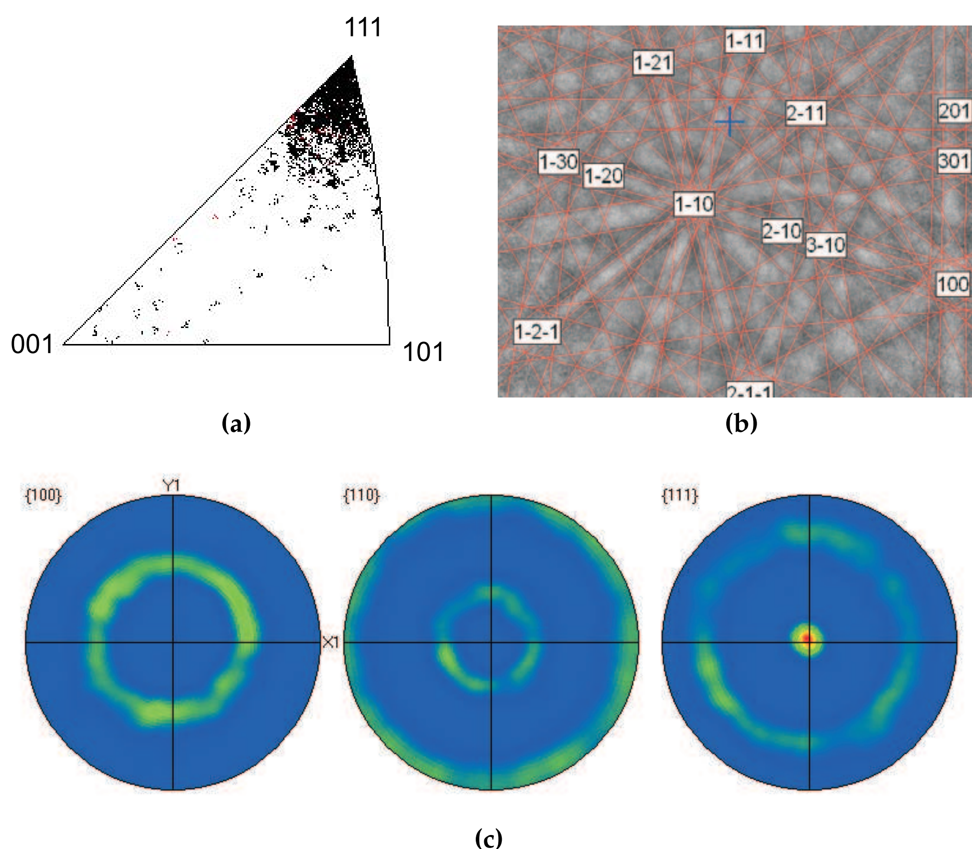

(a) (b)

(c)

Figure 5.3: (a) Inverse pole plot in the normal (Z) direction and (c) pole figures obtained by orientation mapping of 30200 points shows a clear preference for (111) grain growth. A representative pattern in (b) shows that despite small grain sizes, a good-quality pattern can be obtained and indexed.

was performed by AFM and SEM imaging, and representative images are shown in fig. 5.5.

For flat films I used flame-annealed 150 nm thick films on cleaved mica substrates, acquired from SPI supplies [124]. In this case, the films are very smooth (around 1 nm RMS roughness), the grain growth is again (111) preferential, and the average grain sizes are of around 1 μm in diameter. An AFM image of the 150 nm thin film deposited on mica is given in fig. 5.6.

The three different specimens have a different initial roughness and grain sizes. A representative histogram of surface roughness for each 150 nm thick film is given in fig. 5.7. The mica-deposited films have the narrowest distribution of surface heights, meaning that the surface is quite evenly flat. The sputter deposited specimens have a broader distribution, but the average height is smaller than in the case of mica-deposited films. Essentially, this means that the step heights between individual grains are quite regular. The third film, deposited by thermal evaporation of Au on a glass substrate, has by far

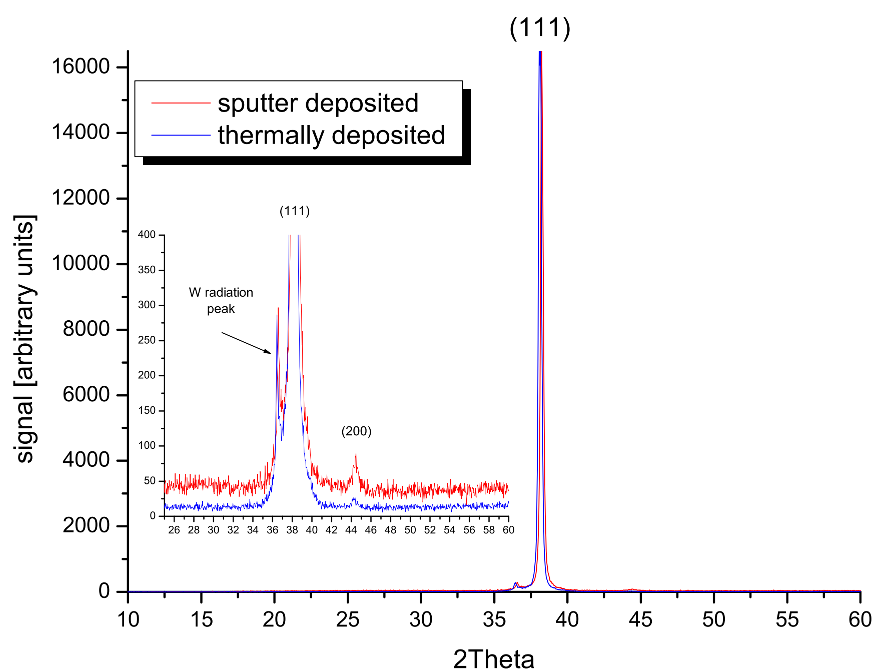

Figure 5.4: XRD measurements of Au sputter deposited and thermally deposited thin film. (111) peak is large, while the other peak (200) is suppresed.

the widest distribution of surface heights. This is an indicator that the surface is much rougher, with large elevation differences between individual grains.

The plot shown in fig. 5.8 shows the grain size distribution of the three specimens of the same thickness (150 nm). I used SEM images in the backscattered electron imaging mode, which were cross-checked for consistency with AFM images. Electron microscopy was used as the primary determination method of grain sizes for two reasons: one, it enables the visualization of a surface on a larger scale and thus fewer images are needed for determination; and two, there are no problems with blunt AFM tips, tip-surface convolution effects resulting in distorted images, or drift.

The films grown by thermal evaporation show an abundant population of grains below 80 nm diameter, but a fraction of grains coarsens into bigger grains with diameters centered at around 130 nm average size. The sputter deposited films show a quite narrow distribution of grain sizes, a significant fraction of grains smaller than 70 nm in diameter and a smaller population of grains with diameters of 100 nm and more. The flame-annealed thin films grown on mica substrates exhibit by far the largest grains, a significant fraction of grains is larger than 1 μm and the center of the distribution is at about 800 nm.

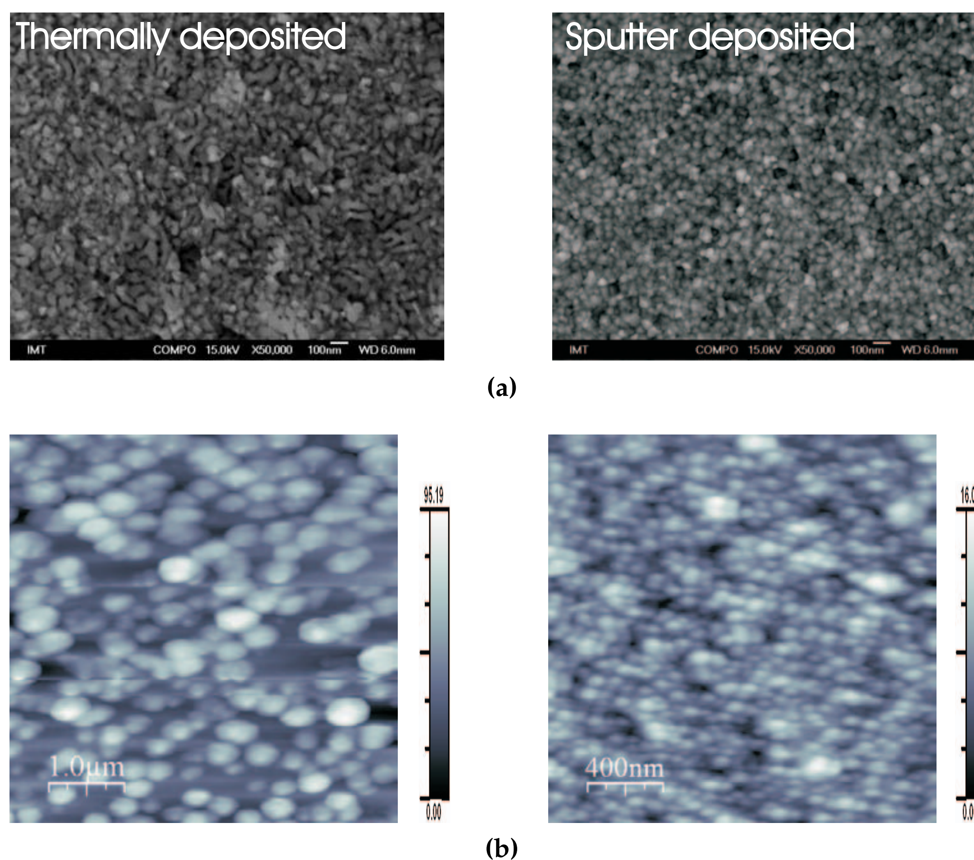

Figure 5.5: Comparison of surface morphologies of initial 150 nm thin films of Au, (a) SEM images and (b) AFM images. The AFM image color scale is given in nm. The sputter deposited specimen exibits smaller and more uniform grains, and surface roughness is much larger in the case of the thermally deposited specimen.

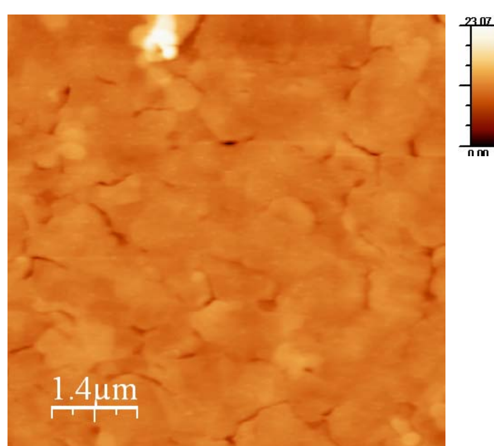

Figure 5.6: Flame-annealed thin Au film of 150 nm thickness, deposited on mica. The specimen exhibits a very smooth surface, as is evident from the color scale (in nm).

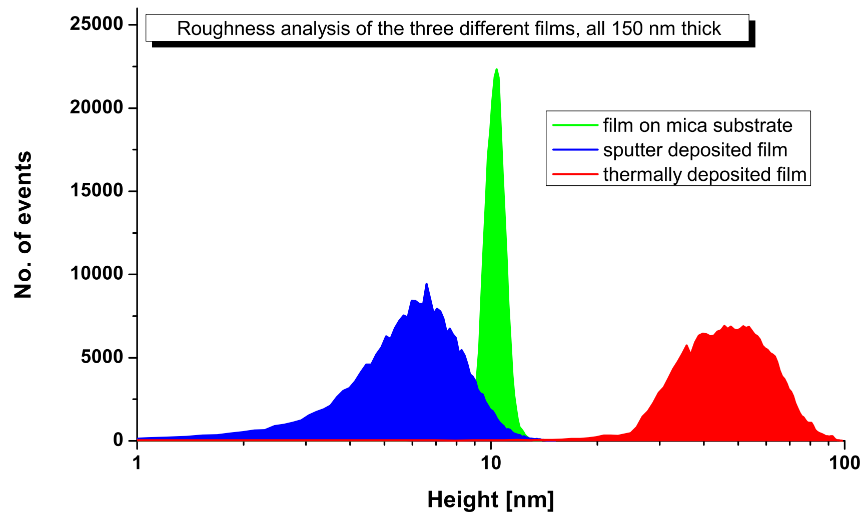

Figure 5.7: Roughness histograms of the three films. Due to large differences in heights, the scale is logarithmic.

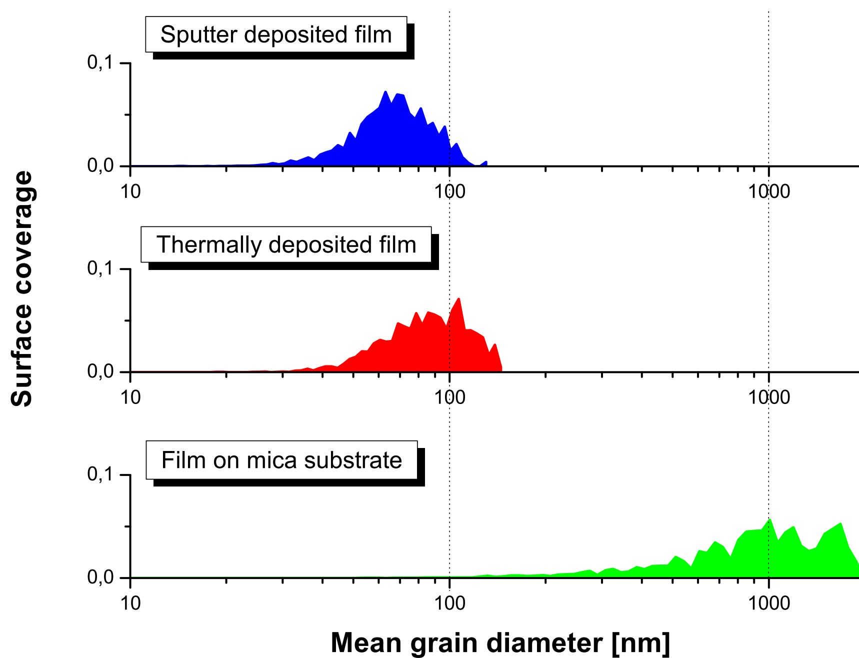

Figure 5.8: Grain size distribution of the Au films.

5.2 Sputtering results

5.2.1 Sputter deposited thin films

In sputtering experiments, I used 150 nm thick films. The films were sputtered at an angle of 80° with 800 eV Ar+ ion beam, varying the sputter times (ion fluences). Ripple-like patterns with wave vector parallel to the ion beam projection formed. The surface modifications during the sputtering process were monitored *ex-situ* by AFM as well as SEM, and the images of surface morphology vs. the sputtering dose for a sputter deposited film is shown in fig. 5.9. AFM images show that after 15 minutes of sputtering (corresponding to an ion dose of 5×10^{17} ions/cm^2) well defined ripples with wavelengths comparable to grain sizes form.

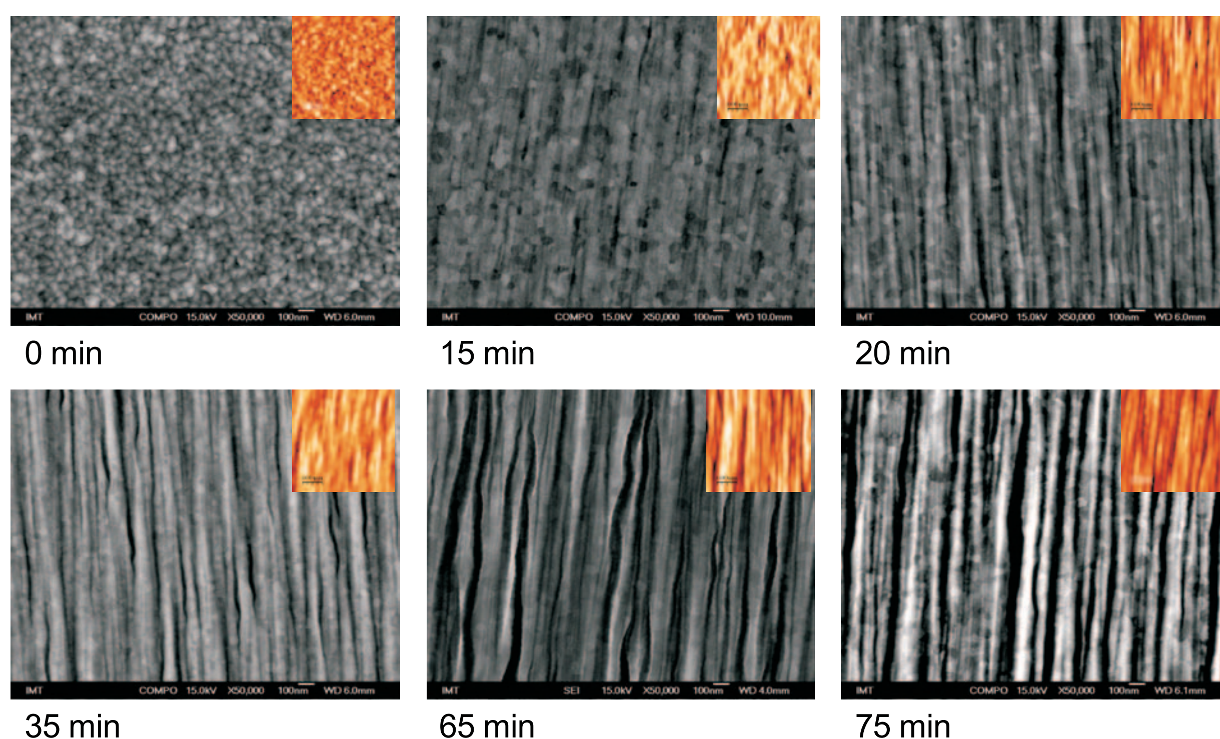

Figure 5.9: Sputter time evolution of sputter deposited specimens, SEM and AFM images as insets.

As the time of sputtering increases, the spatial coherence of the ripples improves. Line scans across the ripples also show that with increasing sputtering time, the ripple profile becomes smoother. With prolonged sputtering the ridge length becomes comparable with the AFM sampling window (3x3 μm^2). This is seen in fig. 5.10, where surface morphologies after 7 minutes (ion dose 2.3×10^{17} ions/cm^2) and 75 minutes (ion dose 2.5×10^{18} ions/cm^2) are compared. AFM images have the same size, and the corresponding 2D FFT patterns are shown below the images. An improvement of the ripple periodicity exhibits itself in the better quality of the FFT pattern.

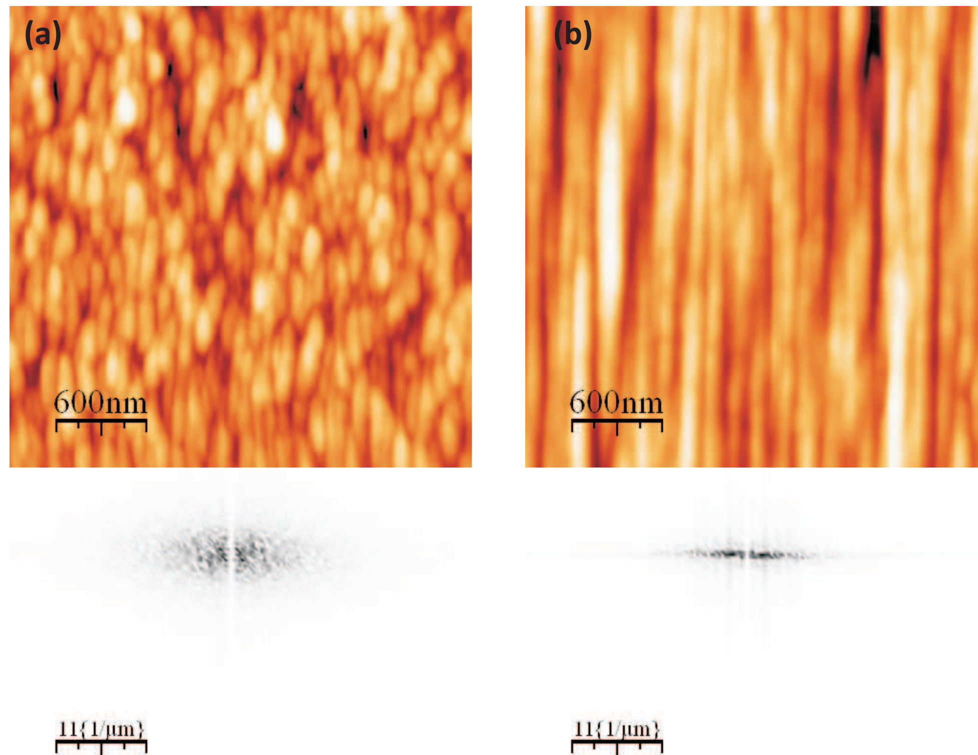

Figure 5.10: Evolution of surface morphology: (a) 7 minute sputter time, (b) 75 minute sputter time. Below each image is a corresponding 2D FFT image, showing the periodicity of the ripple.

I analyzed a statistically significant number of AFM images (usually between 5 and 10) for the determination of dominant wavelength by means of 2D Fast Fourier Transform. The results are collected in the graph shown in fig. 5.11. As can be seen, ripple wavelengths range from 55 nm to 110 nm, depending on the sputtering dose, with average RMS roughness between 2 nm of the pristine film to about 10 nm in the case of 75 minutes sputtered film (corresponding to an ion dose of 2.5×10^{18} ions/cm^2).

Contrary to the models predicting a power law monotonic increase of ripple wavelength with the increased sputtering time, here a different trend is observed. The wavelength first decreases as a function of the ion dose and eventually increases, following a monotonic curve. The initial wavelength selection process appears to be linked to the morphological details of an unsputtered sample and the starting average separation distance is comparable in size to the larger grains of the film. The RMS roughness increases with the sputtering time in a monotonic way.

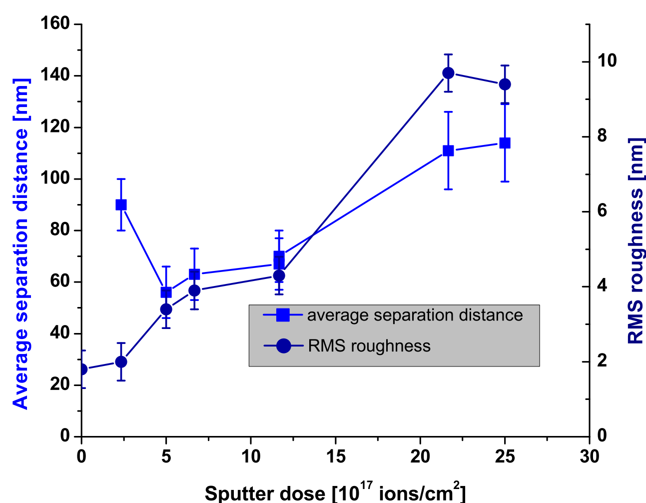

Figure 5.11: Evolution of average separation distance (wavelength) and RMS roughness of the sputter deposited thin film.

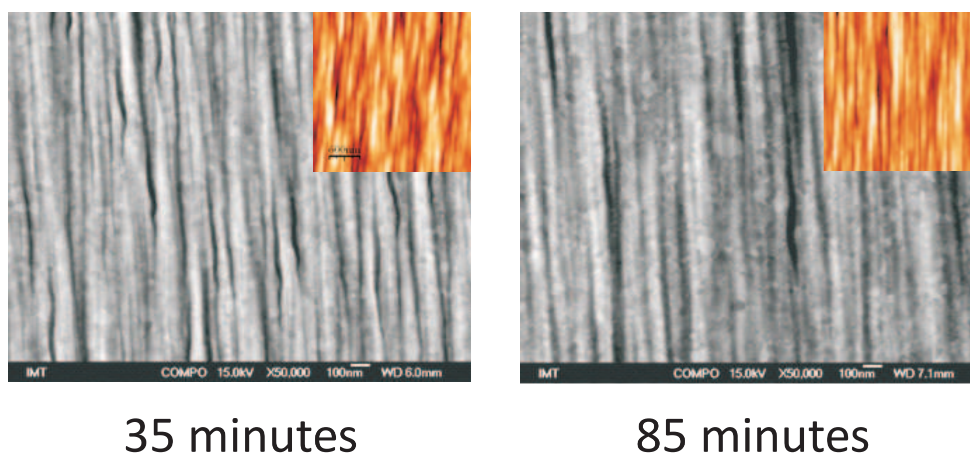

Figure 5.12: Sputtering an 150 nm thermally deposited film also results in regular ripple formation. Two SEM images with AFM images as insets or two different sputtering times are shown.

5.2.2 Evaporated thin films

As has been mentioned before, the thermally deposited thin films have a larger surface roughness, a wider distribution of grain sizes and on average a larger grain size compared to the sputter deposited thin film of same thickness. All these characteristics lead to a slightly different behavior of the sputter evolution. In fig. 5.12 two images showing the time-evolution of the surface morphology during sputtering are shown: the first one after 35 minutes of sputtering (corresponding to an ion dose of 1.0×10^{18} ions/cm^2) and the second one after 85 minutes of sputtering, when the surface has received an ion dose of 2.8×10^{18} ions/cm^2.

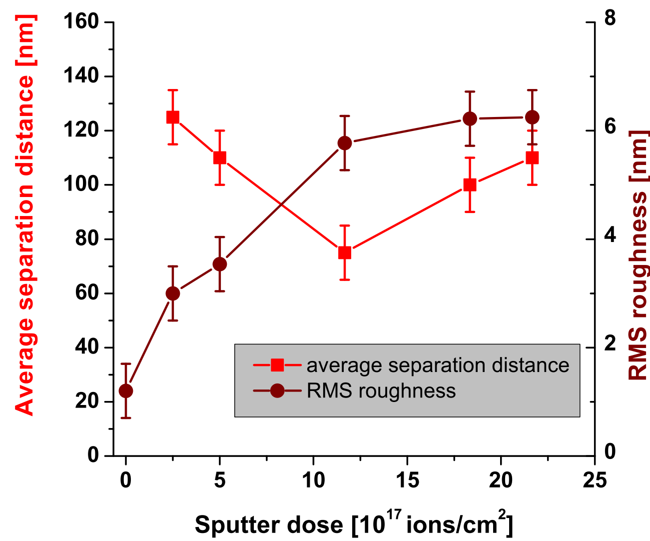

Figure 5.13: Evolution of average separation distance (wavelength) and RMS roughness of the thermally deposited 150 nmthin film.

The situation of initial wavelength selection process being governed by the larger grains in the polycrystalline thin film is even more pronounced in the case of thermally deposited thin films, due to initial larger grain sizes and their wider distribution. Fig. 5.13 shows the evolution of RMS roughness and average separation distance of the ripple ridges. In this case, the initial decrease of the average distance between the ripple ridges is even more pronounced - the wavelength decreases down to 70 nm at 1.5×10^{18} ions/cm^2 sputter dose and afterwards gradually increases.

5.2.3 Patterning a flat film with large grains

Quite different is the case of flat films. The third set of substrates used were 150 nm thick Au films, deposited on a cleaved mica substrate and flame annealed. These films are characterized by large grains (grain size distribution centered at 800 nm grain diameter) with a large portion of grains exceeding 1 μm diameter. AFM imaging of the as-received flame annealed 150 nm thin Au film deposited on mica substrate also shows a very smooth surface with RMS roughness of around 1 nm. The grains grow epitaxially with the cleaved mica substrates, and the grains exhibit (111) surfaces, as was confirmed by EBSD measurements.

In this case each of the grains behaves as a flat Au(111) surface. Morphology evolution is plotted in Figure 5.14.

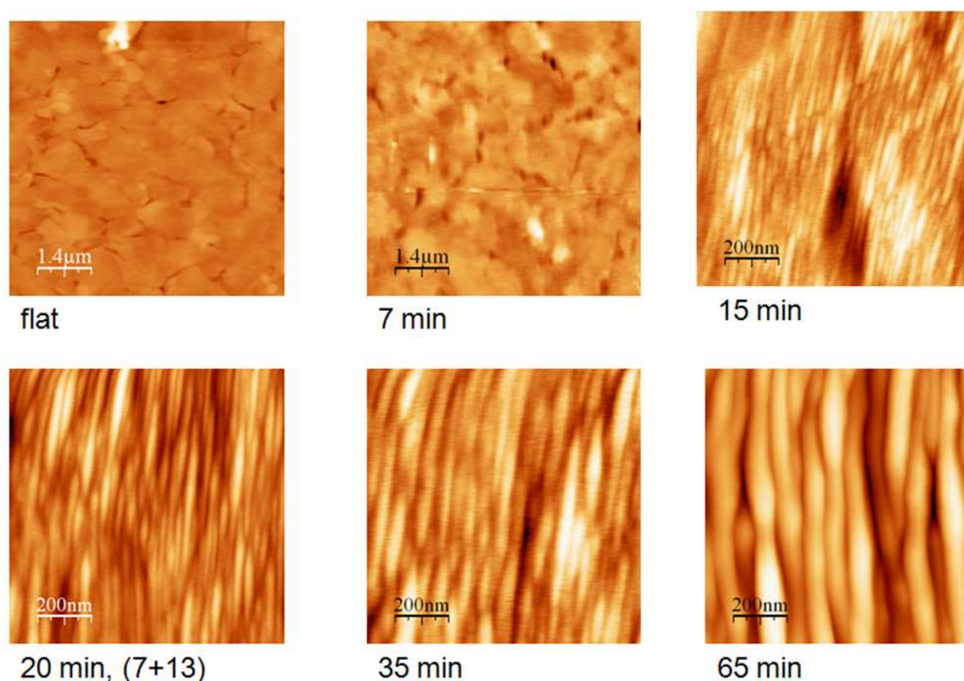

Figure 5.14: Patterning a 150 nm thin Au flat film, deposited on mica substrate.

Patterning a flat film with large (111) terminated grains resulted in an increase of average separation distance ant the RMS surface roughness, as can be seen in the fig. 5.15. The incipient wavelength, which is about 20 nm, is in good agreement with the published data on monocrystalline surfaces [15, 125].

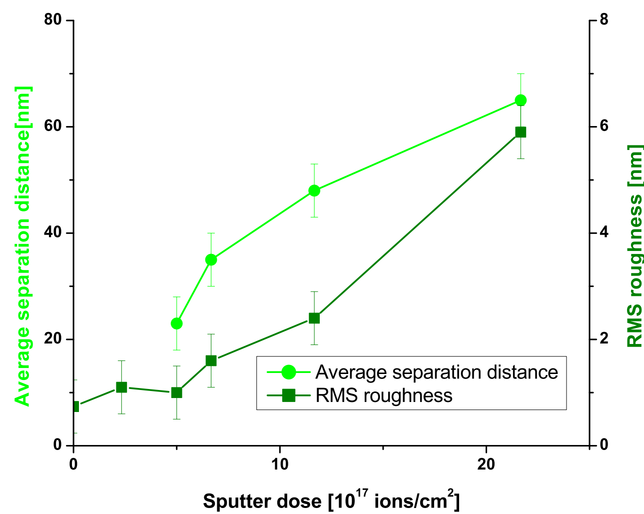

Figure 5.15: Evolution of surface RMS roughness and wavelength of the resulting ripples on a flat film deposited on mica substrate.

5.3 Shadowing instability

When sputtering two single crystal substrates of the same orientation, composition and using the same ion beam parameters, one would expects an equivalence of ripple wavelength and average roughness in the case of same ion dose. However, comparing the three different polycrystalline metal substrates (one with flat large grains and the other two consisting of smaller grains and rough surface), we can observe this is not the case. With initial non-flat thin films we notice two things: (i) the initial selection of the wavelength is closely related to the dominant grain sizes, with a decrease of the dominant ripple wavelength until a threshold dose is reached; and (ii) the ripple wavelength monotonically increases at higher fluences, which is a trend expected for single-crystal surfaces.

This behavior can be explained by introducing a *s*hadowing mechanism. Under grazing ion incidence conditions, the lateral distribution of the ion impact sites becomes non-stochastic and spatially modulated by the local surface corrugations of the pristine grain distribution. Regions behind large and tall grains are shadowed from the ion beam and thus experience a reduced erosion rate, while the regions behind small and shallow grains or in the valleys are eroded efficiently, resulting in a self-leveling mechanism of the ripple ridges along the ion beam projection. The initial wavelength selection is thus driven by a *s*hadowing instability, in which the taller and larger grains select a ripple wavelength that is different from the value expected for an initialy flat film. A schematic diagram depicting the shadowing mechanism is given in fig. 5.16.

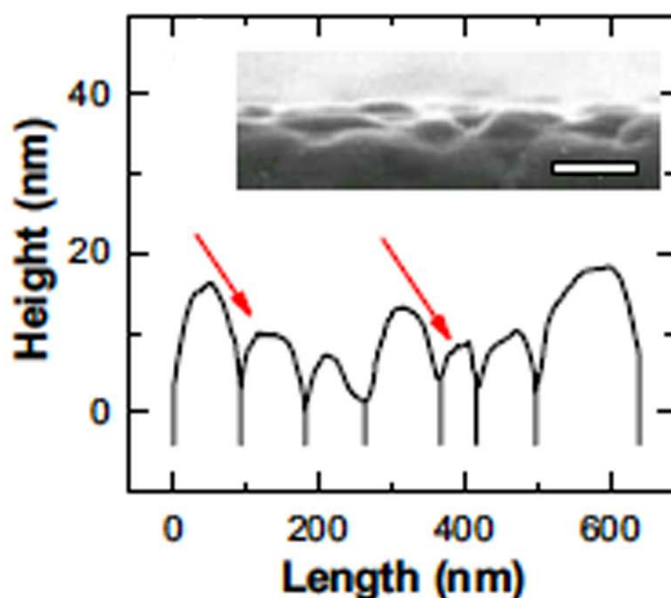

Figure 5.16: Shadowing mechanism. The taller and larger grains shadow the smaller grains, so these regions sputter at a slower rate [108].

The decreasing trend of ripple wavelength in the case of rough films with comparatively small grains can be qualitatively explained with the aid of the Bradley-Harper linear model which predicts the existence of an intrinsic wave mode growing faster than all the other ones. The amplification factor given by the Bradley-Harper theory is positive for all long wavelengths, peaked at an intrinsic wave mode, and negative for some critical wavelength below the intrinsic wavemode [126]. The intrinsic Bradley-Harper wavelength found for single crystal like flat films is well below the initial wavelength imposed by the shadowing instability.

A further important result can be derived from the sputtering data of thin films. The initial grain-size distribution of the non-flat films is responsible for a significant reduction in the ion dose required for the formation of ripples in comparison to the case of the flat surface. Thus, we introduced the concept of *s*caled ion dose, as ripples of comparable wavelength are formed after a substantially larger irradiation dose in the case of flat surfaces. This is seen in fig. 5.17. The data points for roughness and wavelength of the rougher films can be shifted horizontally relative to the flat films, which leads to an overlap of the data points for both wavelength as well as ripple heights over the single-crystal like flat film regime.

The concept of scaled ion dose makes even more sense if one looks at sample topographies of the different series, irradiated with the same *s*caled ion dose, which are compared in 5.17 in panels (c)-(e). The respective two-dimensional fast Fourier transform line cuts evidence the equivalence of ripple periodicity. This implies that when there

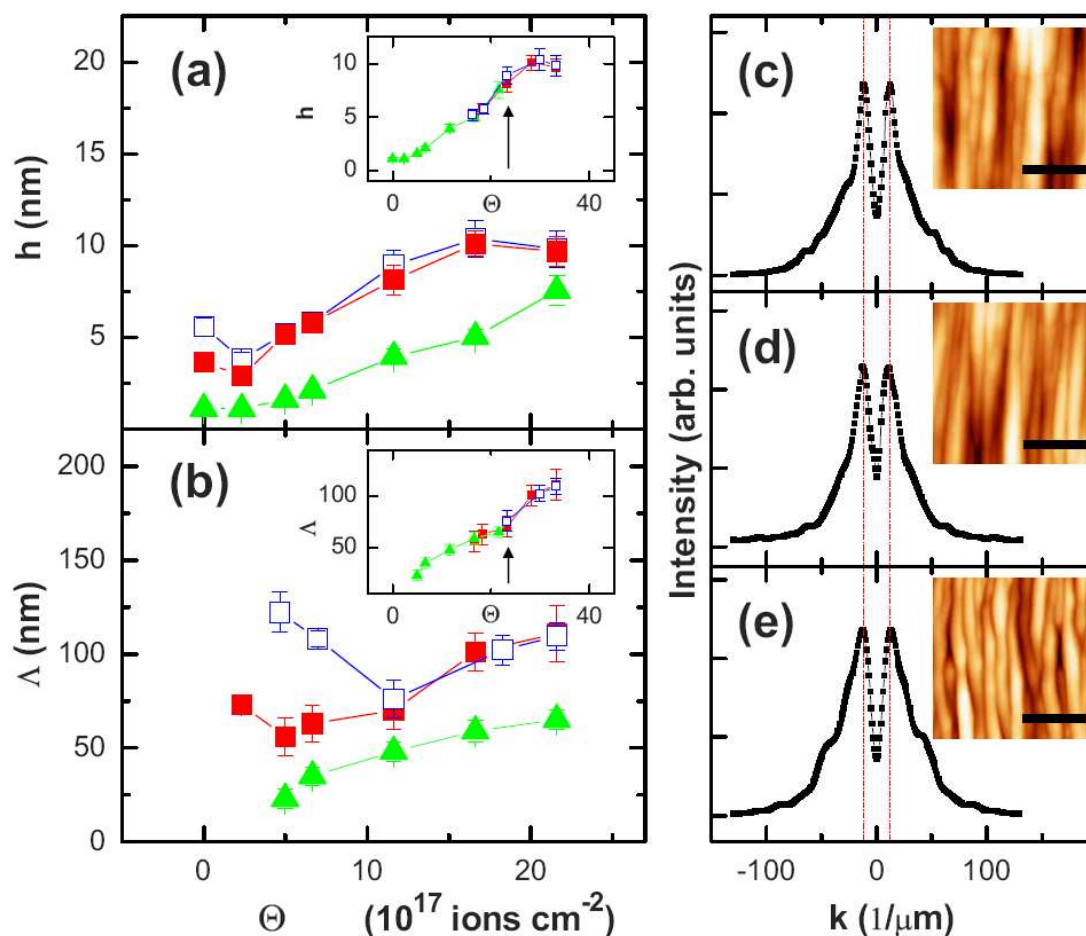

Figure 5.17: (a), (b): Average amplitude (h) and periodicity (Λ) of the formed nanostructures vs. ion fluence, derived from the AFM images. The green triangles refer to the flat films, blue open squares to thermally deposited films, and red closed squares to sputter deposited films. Insets show a horizontal rigid shift of the curves representing the rougher films, which leads to an overlap of the data points of the rougher films and the flat film. (c), (d) and (e): Topographs of the different sample series irradiated with the same scaled ion dose; (c) thermally deposited specimen, (d) Sputter deposited specimen, (e) flat film. The respective 2D FFT line cuts evidence the equivalence of wavelength [108].

is initial topography present, the subsequent evolution is receiving a head start with respect to the flat initial case. The primitive roughness of the polycrystalline film can thus efficiently reduce the ion dose required for the formation of ripple modulations.

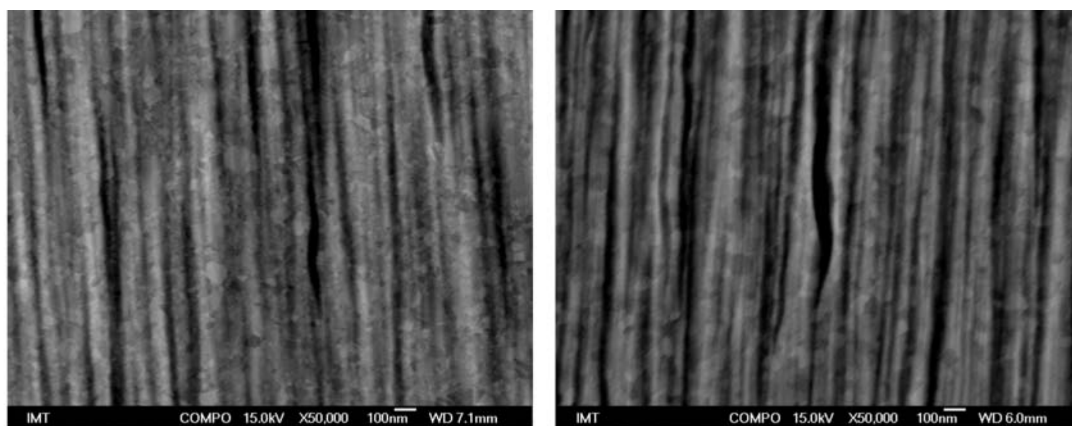

Figure 5.18: SEM image of the ripples propagating through individual grain boundaries. (a) Sputter deposited film with smaller grains; (b) Thermally evaporated film with larger grains. Both films were sputtered by the same ion fluence.

5.4 Grains and grain boundaries

In the case of polycrystalline thin films, the diffusion of mobile species (adatoms and vacancies) is, within an individual grain, behaving as a single-crystal with the same crystallographic termination. However, one would expect that the grain boundaries would represent a barrier against intergrain mass transport, and impose a characteristic upper limit for diffusion and consequently for ripple elongation. Additionally, the different crystallographic orientations of adjacent grains, which impose a local anisotropic diffusion bias to the mobile species, should add a further limitation for the propagation of a ripple pattern from grain to grain. However, contrary to the expectations, SEM analysis of the sputtered films demonstrates that the ripple pattern can propagate from grain to grain coherently across the boundaries, as is evident from fig. 5.18.

In the case of large grains, where the initial surface is quite flat, the situation is similar: ripples propagate across grain boundaries with just a slight mismatch, which could be attributed to minute changes in the in-plane rotational texture from grain to grain. This is visible in fig. 5.19. Otherwise, the ripple propagation on the flat film is not hindered and the propagation length of the ripple ridges can reach or exceed several micrometers.

These results underline the role of the topographic roughness in determining pattern formation. Though the presence of submicron grains with different in-plane orientations might hinder intergrain diffusion of mobile particles, for glancing ion sputtering conditions employed here, the ripple orientation is imposed by the beam projection single crystal erosive regime and coherent ripple propagation is observed across several microns. On the more applied side, the present observations support the extension of the results derived from single crystals to the technologically relevant class of polycrystalline films, and suggest the use of substrates with an artificially corrugated

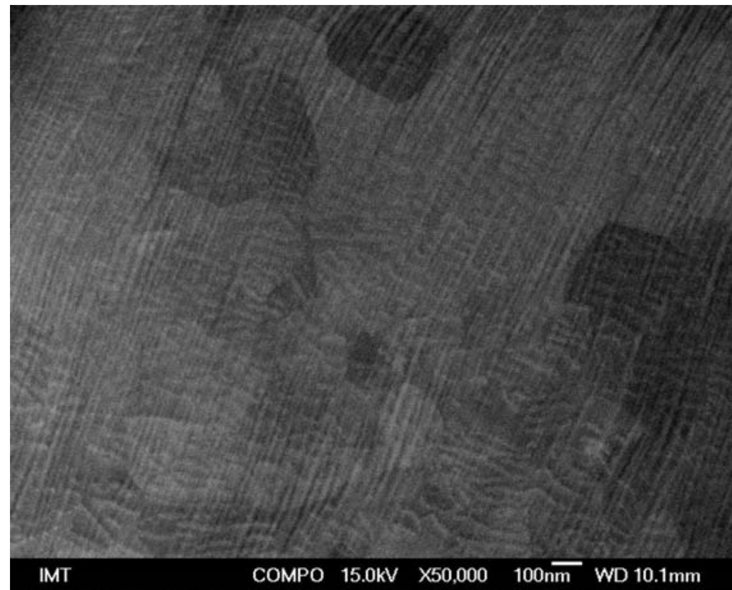

Figure 5.19: SEM image of the ripples propagating through individual grain boundaries in the case of the flat film with large grains. A slight mismatch of the ripple orientation can be observed on the grain boundary, but otherwise the ripple propagation is not hindered and the ripple lengths can exceed several micrometers.

morphology for triggering, via a shadowing instability, the formation of a pattern with a periodicity imposed by the primitive features.

6

FeSiAl polycrystalline alloy - characterization of structures

Another model system used for ion beam sputtering experiments was an FeSiAl alloy, belonging to the class of electrical steels. As described in the Materials and Methods chapter, the specimens were etched in a Gatan Precision Etching and Coating System (PECS 682) using Ar^+ ions. The resulting structures were characterized by SEM and AFM.

6.1 Classification of features

In this section, I will adapt the classification of features provided by Carter *et. al.* [17]. Carter proposes a distinction between intergranular and intragranular effects, between isolated and repetitive features and between elevated and depressed structures. A schematic diagram in fig. 6.1 shows the distinction between these features.

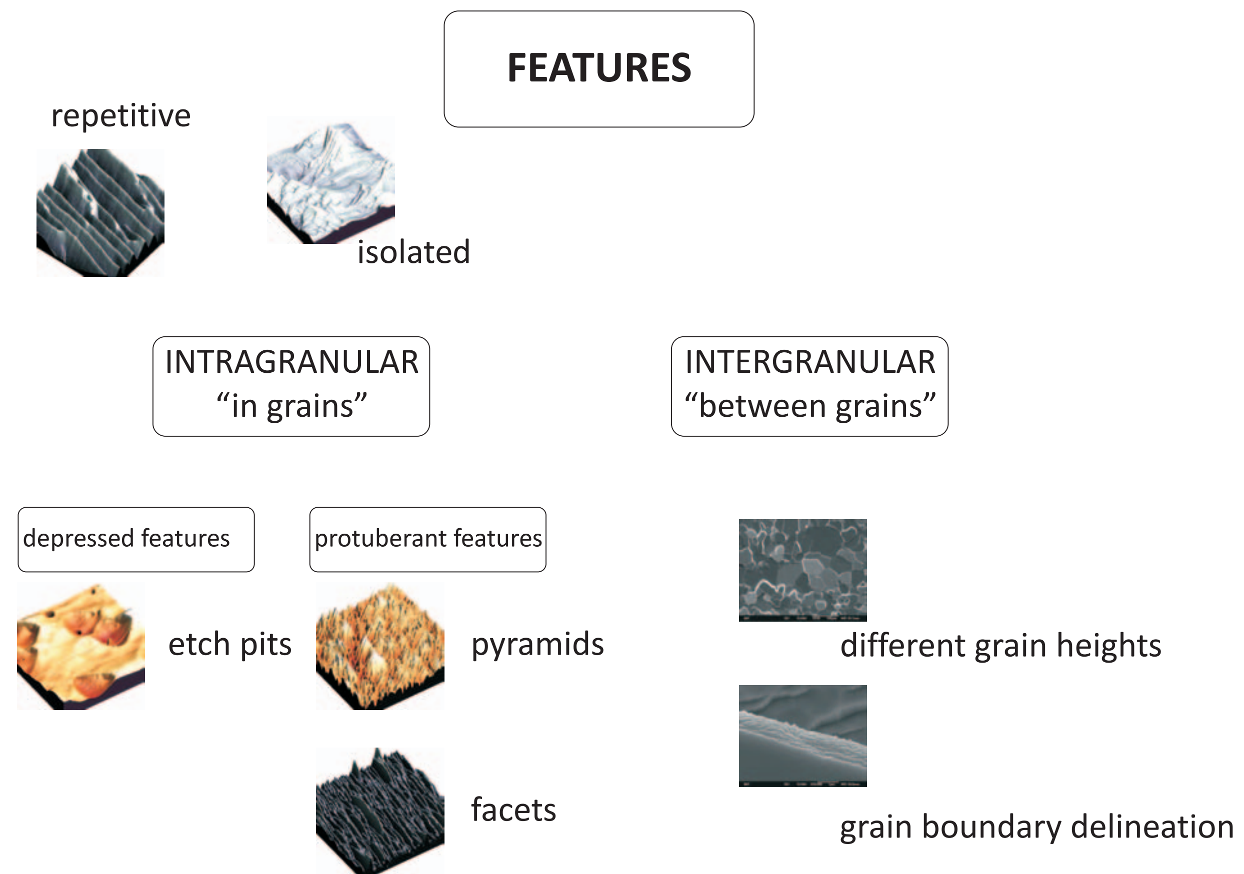

Figure 6.1: Classification of ion beam induced surface morphological properties as proposed by Carter *et al.* [17].

6.2 Intergranular structures

Intergranular effects describe those processes that occur as a result of the differential macroscopic sputtering yield between neighboring grains, due to the dependence of sputter yield on crystal orientation. Grains of different elevations across the surface form, and the relative height difference between the neighboring grains depends on the ion incidence conditions and the individual crystal grain orientation. Grain boundaries, which are essentially low-angle dislocation networks, sputter preferentially and at different rates from the grains themselves.

In the case of FeSiAl alloys used in the experimental work, the grain boundary delineation is very pronounced and diverse patterns form on the grain boundaries themselves. A steep boundary can usually be observed between two adjacent grains, and AFM measurements show that the steps can range from a few tens of nanometers to a few hundred nanometers, depending on the misorientation of the two grains and subsequent etching rates. Near the grain boundary one also observes notable pitting. This effect can be further enhanced by segregation of impurities to surface and grain boundaries. For FeSiAl steels, the segregation of impurities to the grain boundaries and

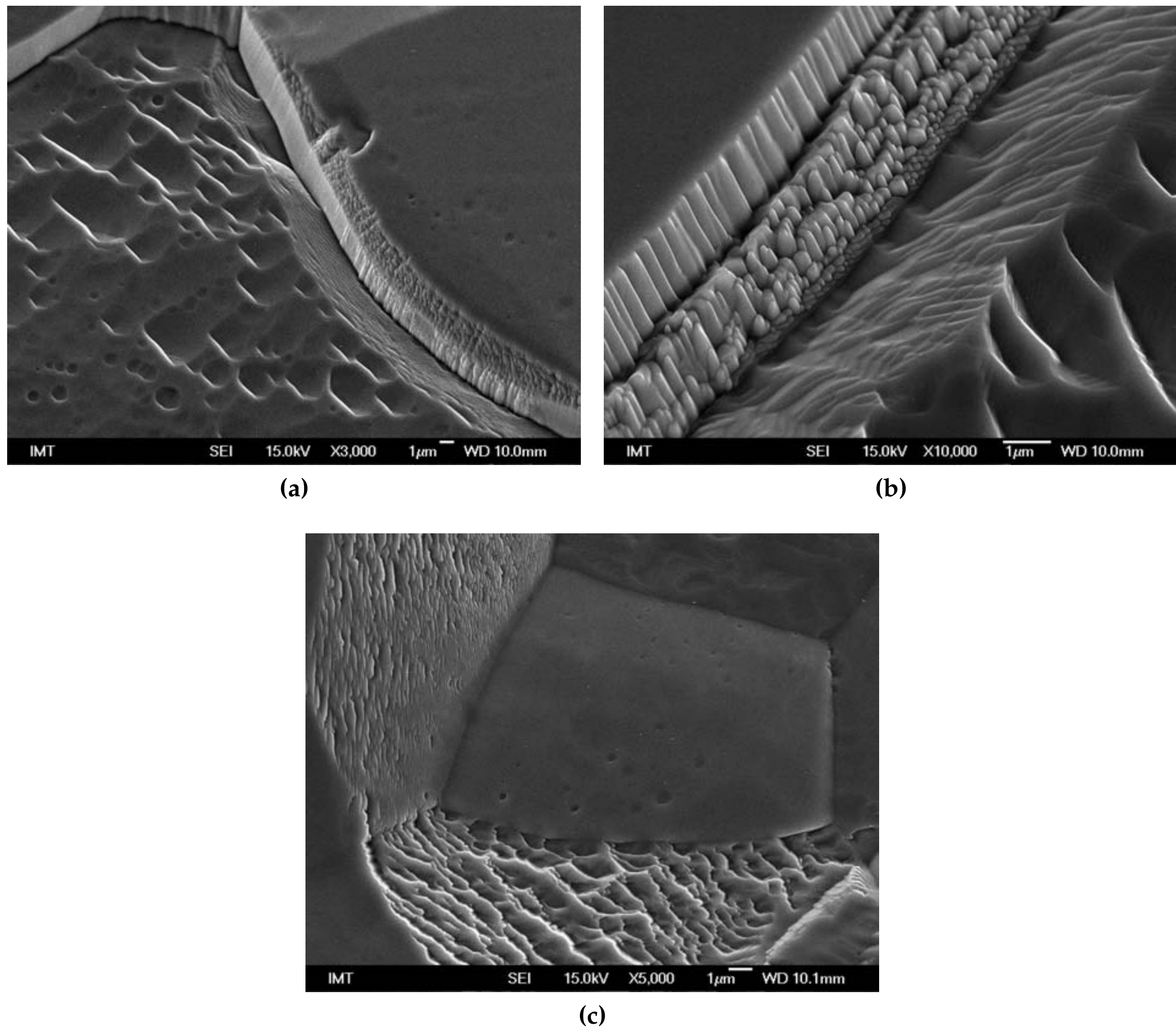

Figure 6.2: Examples of grain boundary delineation - intergranular structures. The material is FeSiAl alloy, etched by Ar^+ ions at (a) 6 keV, 5×10^{18} ions/cm^2, (b) 10 keV, 6×10^{18} ions/cm^2 and (c) 1×10^{19} ions/cm^2. (a) and (c) were both sputtered at normal incidence, and (b) was sputtered at a 45° angle.

free surfaces is very important [127, 128, 129], and as such could also play an important role in the ion-beam induced pattern formation.

The grain boundaries depicted in fig. 6.2 show that the grain boundary delineation is possible for different ion beam parameters. It is also evident from the images that a pattern forms on the grain boundary area itself. In fig. 6.2b one can also see two grain boundaries on top of one another: they each develop a characteristic pattern when exposed to ion beam.

6.3 Intragranular effects

In intragranular effects, the concern is with the processes that occur in specific grains. In effect, these processes are the same as in single crystal substrates, except that with polycrystalline material we expect different behavior of individual grains.

This category can be further divided into two additional sub-categories: the features can be either depressed (such as pit-like structures) or elevated (such as pyramids and cones), relative to their surrounding. Additionally, the features can be either repetitive, giving an appearance of a periodic perturbation; or isolated, meaning that they stand alone and are not periodic through the grain surface. When sputtering a polycrystalline FeSiAl alloy, I observed both depressed and elevated features, and the morphology is either repetitive or isolated. The formation of morphological features is governed mainly by the ion beam angle (at normal incidence mainly etch-pits form, and at off normal incidences the surface undergoes different changes) and the substrate crystallinity (different orientations produce different morphological features).

6.3.1 Etch pits - an example of depressed features

The most clearly defined depressed structures made by the sputtering process are etch pits. Experimental evidence, as is for example [130, 131] suggests that pits develop at local regions in the surface associated with some form of dislocation. Often, chemically induced etch pits are used to determine the dislocation type and dislocation densities. The dislocations present in the material can enhance the sputtering yield at the dislocation site. Still open to debate is the question of whether such dislocations or regions with reduced atomic binding energies are present in the solid before irradiation or are formed by the radiation induced defect production.

In the case of polycrystalline FeSiAl alloys, we observe etch pit development in the case of normal incidence Ar^{+} ion sputtering conditions. Pits started developing even at low ion exposures and the pit density varies from grain to grain as well as with sputtering time. SEM micrographs shown in fig. 6.3 show some examples of etch pits formed by ion beam sputtering.

The images of pits formed by ion etching clearly indicate that pit morphology is correlated with crystal type and orientation, as well as with irradiation conditions. Etch pits formed exclusively during normal incidence ion beam etching. At off-normal incidences the surface exhibited other morphological features. Images of adjacent grains exhibiting differently shaped pits, such as the one depicted in fig. 6.3a, show that the shapes of etch pits could be grain-orientation dependent. Other evidence that leads to this conclusion is the pit symmetry, which suggests that faces correspond to low-index

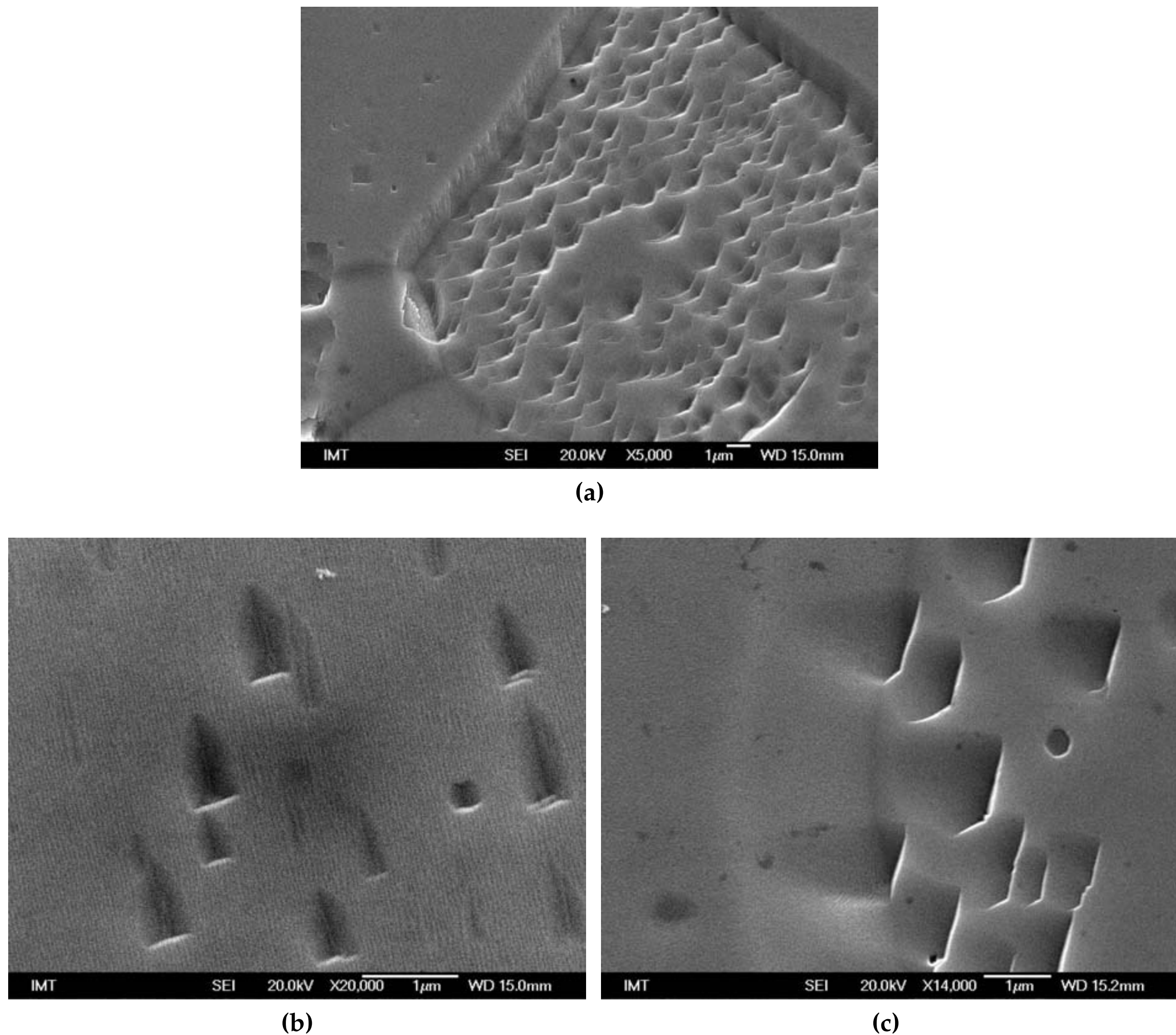

Figure 6.3: Examples of etch pits that form on the surface of FeSiAl alloy during normal incidence ion beam sputtering. (a) 10 keV, $2{\times}10^{18}$ ions/cm^2, (b) 10 keV, $3{\times}10^{18}$ ions/cm^2 and (c) 6 kV, $3{\times}10^{18}$ ions/cm^2.

planes. Further discussion of this orientation dependence of etch pit shape is given in chapter 7. Etch pit distribution is denser in the specimens that contain additional surface active element Se. However, this could also be a consequence of a different density of dislocations and other defects present in the material itself, and it is not possible at this stage to pinpoint the cause.

Atomic force microscopy reveals that the pits are of different depths - ranging from very shallow pits (less than 10 nm in depth) to quite deep ones (around 100 nm in depth), as fig. 6.4 shows.

I also observed ripple formation at normal incidence sputtering along with pits. Ripples were observed in grains with a triangular and a rectangular pit shape, and were observable by SEM imaging as well as with the AFM. The ripples are shallow, with groove depths of around 2 nm to 4 nm, and the wavelength of the ripple structure I observed on

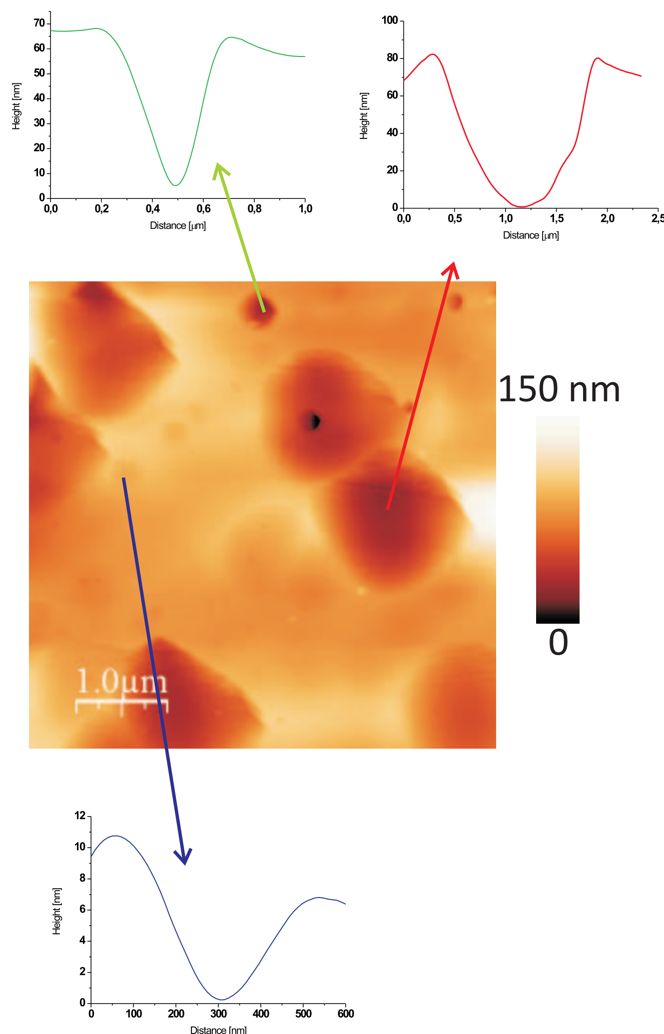

Figure 6.4: Etch pits are different in shape as well as in depth. AFM images of pits present in a single grain. The FeSiAl alloy was sputtered at normal incidence, using a 7 keV beam and the ion fluence was 4.5×10^{18} ions/cm^2.

a particular grain seen in fig. 6.5 is around 80 nm. The ripple peak separation distances are quite uniform and much deeper individual etch pits between them are present.

6.3.2 Protuberant structures - triangular facet-like structures

Many observations of pyramidal or conical structures on the surfaces of ion sputtered materials have been documented in [17]. On FeSiAl alloy surfaces, I observed triangular structures resembling pyramids. An example of such structures is given in fig. 6.6. Image in fig. 6.7 shows AFM imaging of the same structure (from the same specimen and the same grain).

The triangular structures form on certain individual grains at a wide range of off-normal sputtering conditions. In my experiments, I observed some triangular faceting in all

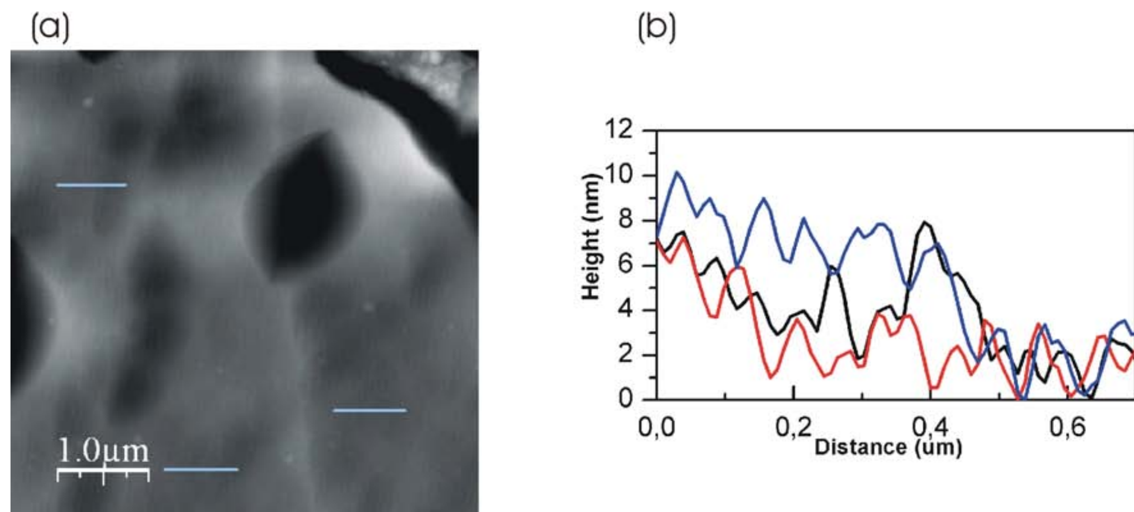

Figure 6.5: Ripple pattern formation along with much deeper pits. AFM image and line profiles, showing the rippled surface. The specimen received $3times10^{18}ions/cm$, and the beam energy was 6 kV.

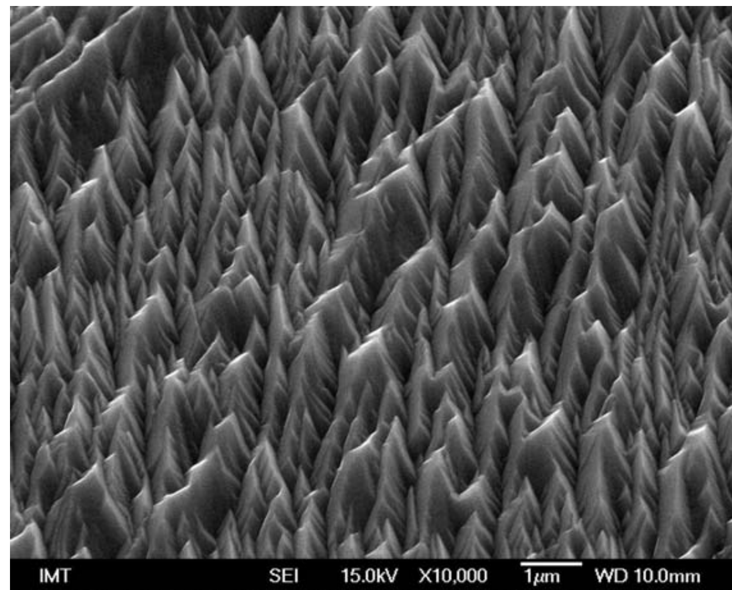

Figure 6.6: An example of protuberant features - triangular facet like structures. FeSiAl alloy was bombarded by Ar^{+} ions of 6 keV energy at 60° angle of incidence for 40 minutes with 300 μA current.

specimens sputtered at angles larger than 45°, regardless of the ion energy (varied from 6 keV to 10 keV) or the ion fluence. Several line profiles along the facets are shown in fig. 6.8.

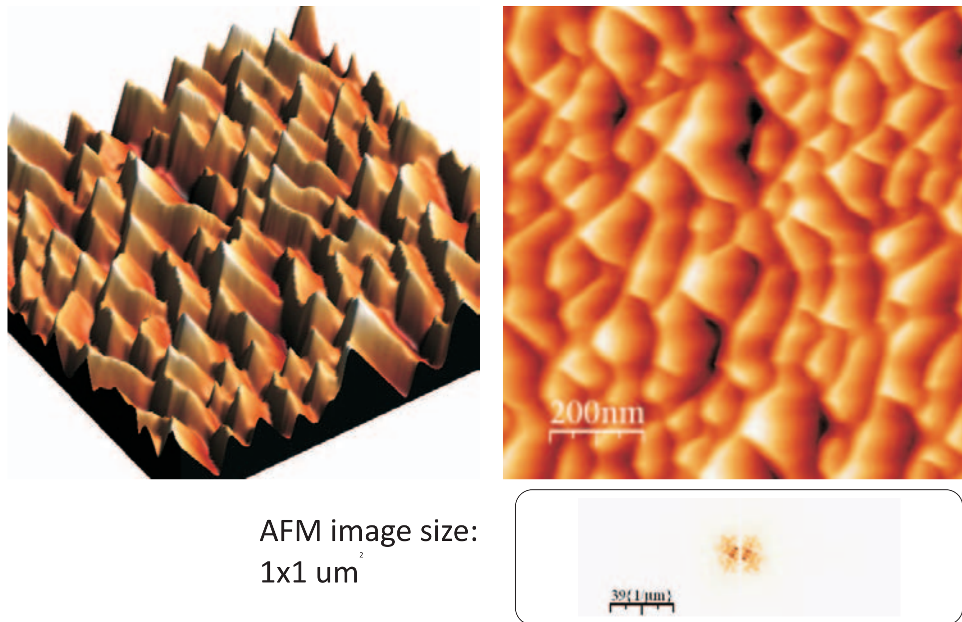

Figure 6.7: Triangular structures as they formed on a grain in polycrystalline FeSiAl alloy: 3D AFM image representation, 2D AFM image representation and the corresponding 2D FFT, showing the image periodicity. FeSiAl alloy was bombarded by Ar^+ ions of 6 keV energy at 60° angle of incidence for 40 minutes with 300 µA current.

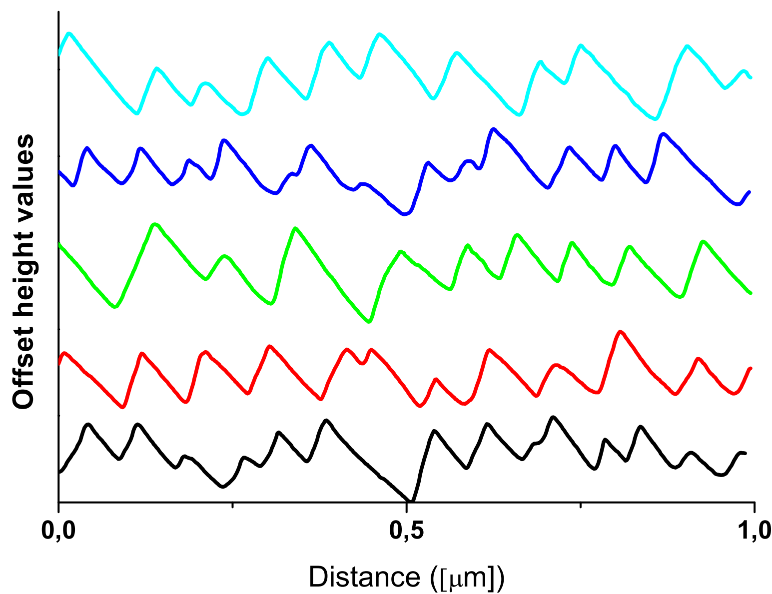

Figure 6.8: Some line profiles along the triangular structures produced by ion beam bombardment. (FeSiAl alloy was bombarded by Ar^+ ions of 6 keV energy at 60 ° angle of incidence for 40 minutes with 300 µA current.)

6.3.3 Periodic ripple-like structures

The most abundant structures observed are periodic ripples. A closer look at these structures by AFM shows that the ripple tops are not rounded, but the structure resembles roof-top-like ripples. An example of such facets is given in fig. 6.9.

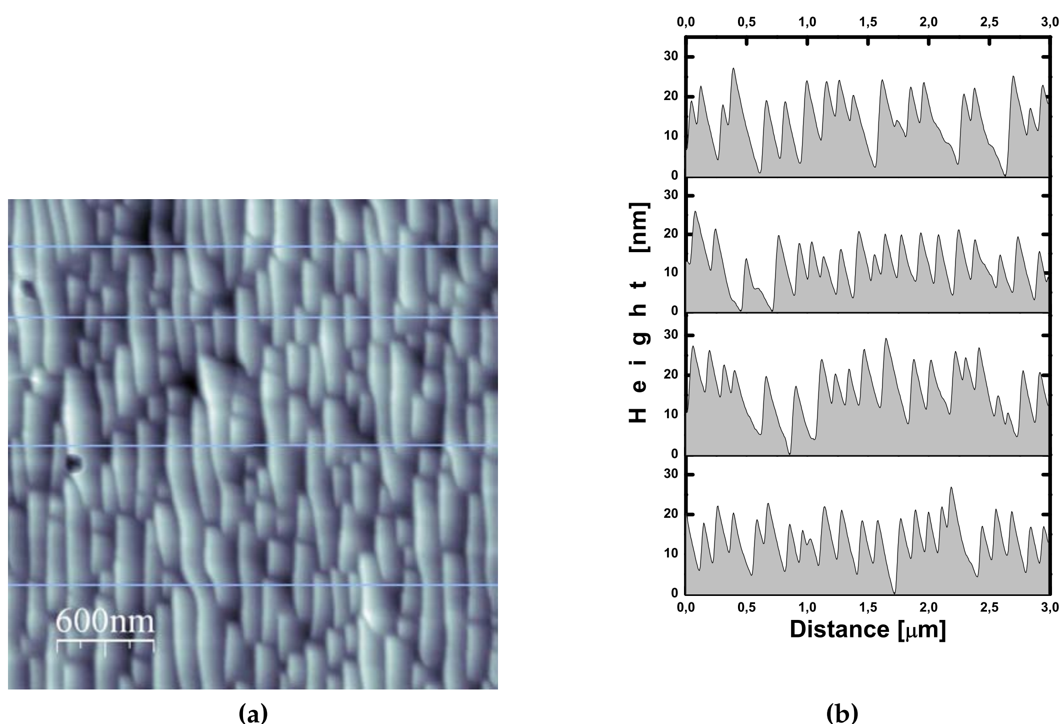

Figure 6.9: The structures that form resemble facets with steep sides instead of ripples with rounded tops.

The facets posses numerous shapes: they can be oriented either parallel or perpendicular to the ion beam direction, and the characteristic ridge separation length seems to depend more on the nature of the individual crystal grain than on the sputter time. Three different facet examples are seen in the line profile shown in fig. 6.10. Many authors also report the formation of facets on the surfaces of other materials, for example on Ni surfaces [132] or on Si(111) surfaces [133] when etched by oxygen ions.

However, the facet slopes are not universal - they depend on the sputtering parameters (mainly the incidence angle) and the surface crystallinity itself. An attempt to correlate the facet angles with ion beam orientation has been made in for example [132]. The authors suggest a two-step model for facet formation. Initially small oxide islands are formed and act as nuclei for the facet formation. The islands are tilted and faceted as a result of successive surface diffusion in a selected direction due to the surface momentum transfer from the incident ions. At the facet propagation step, the facets grow larger and the summits of the facets are propagated toward the ion beams by the great

difference in sputtering rate of the two facet faces. A similar mechanism can be used to explain the different facet slopes in the case of FeSiAl alloys.

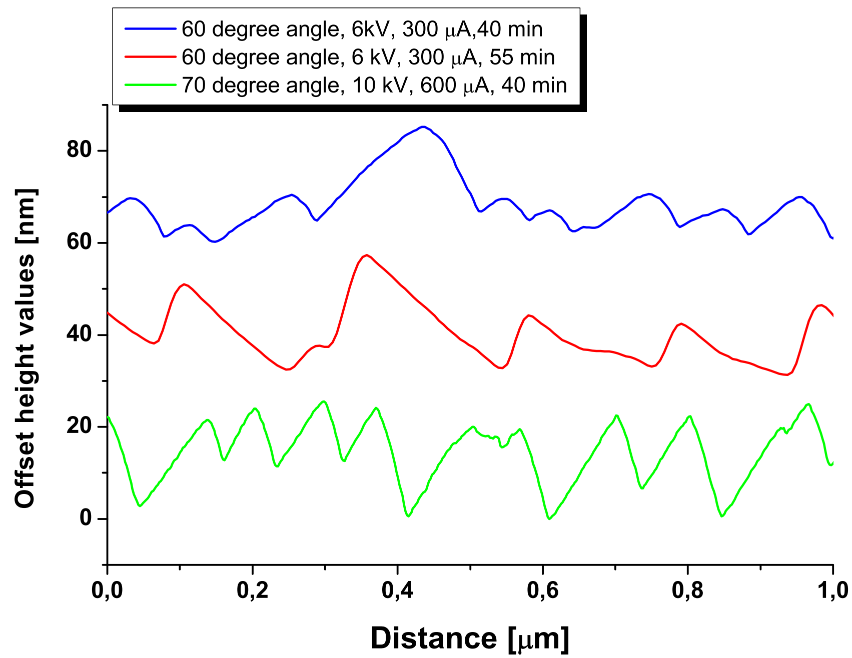

Figure 6.10: Comparison of AFM line profiles for three different sputtering conditions.

6.3.4 Smoothing of individual crystal grains

Another possible morphology that can develop on the surface of polycrystalline alloys is the smoothing of individual grains, as fig. 6.11 shows. SEM images as well as AFM measurements confirm the fact that smoothing takes place. Smoother grains were only observed at off-normal incidence conditions. The possibility for a surface to undergo some smoothing, or a layer-by-layer erosion, is documented in the literature, for example [134] or [135].

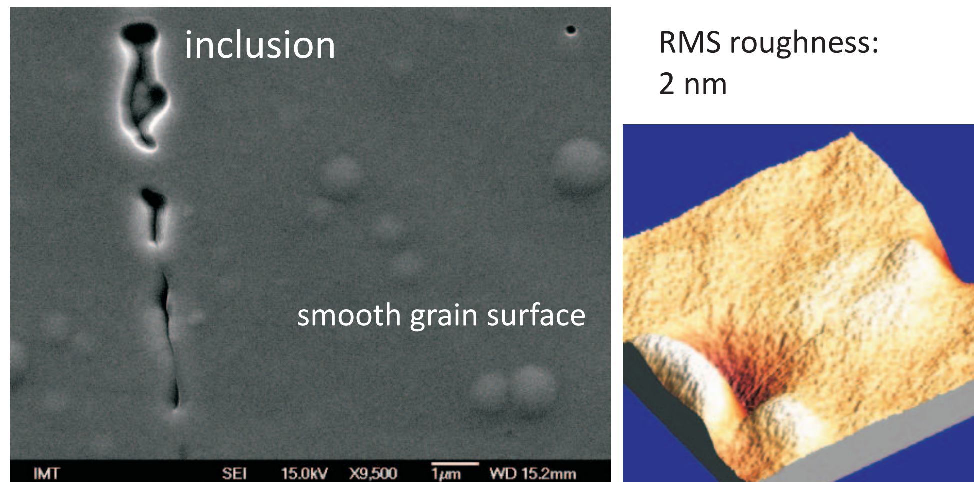

Figure 6.11: An SEM and AFM micrograph of a grain that underwent smoothing mechanism - average RMS roughness of the surface as was estimated from AFM images is 2 nm.

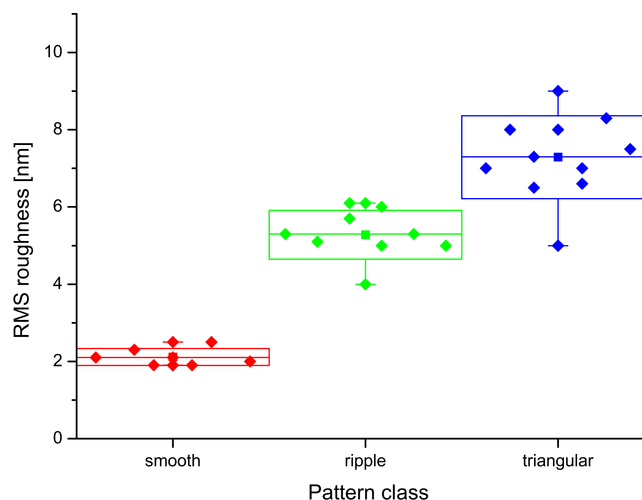

Figure 6.12: A "box plot" of roughness measurements of individual pattern class: smooth, ripple, and triangular facet-like structures. Data collected on a specimen sputtered at 60° angle of incidence, 300μA current for 40 minutes.

An important parameter that quantitatively determines the changes the surfaces undergo during ion beam sputtering is the RMS surface roughness, which can be estimated from AFM measurements. As there are many different morphological features that can form during ion beam sputtering, I collected the roughness data in plot in fig. 6.12. The roughness measurements of individual pattern classes, described in this chapter, are given: smooth surfaces, periodic ripple (facet) surfaces and triangular surfaces. All plotted data were acquired from the same specimen, so they take into account just the difference in surface crystallinity, but not the ion beam processing conditions. The angle of incidence was 60°, the sample was sputtered for 55 minutes at 6 keV energy and 300 μA beam current. The box plot shows that the different pattern classes exhibit individual roughnesses, and the triangular structures are roughest in appearance.

7
The role of grain orientation

Ion beam sputtering causes morphological changes on the surface of the specimen, resulting in different patterns. These patterns are limited by the individual grain boundaries and it seems as if an individual grain acts like a single-crystal of a defined orientation. In this chapter, I explore the connection between individual grain orientations and the patterns that form on the surface. To do this, I used SEM imaging in correlation with EBSD to determine the crystal orientation of individual grains. I collected data from a number of individual grains and found a correlation between the pattern and the orientation. In this chapter, I also include measurements on normal incidence sputtering of single crystal substrates to validate the formation of grain orientation dependent etch pits.

7.1 Initial characterization of the alloy

FeSiAl alloy is a polycrystalline material. The microstructure consists of α-Fe grains (bcc structure) with some inclusions, depending on the composition [136, 137]. A micrograph of the specimen surface is shown in fig. 7.1. This type of steel is used for the production of electrical motor cores and transformers. There are two available types of electrical steels: non-oriented and oriented, and the first was used in this work.

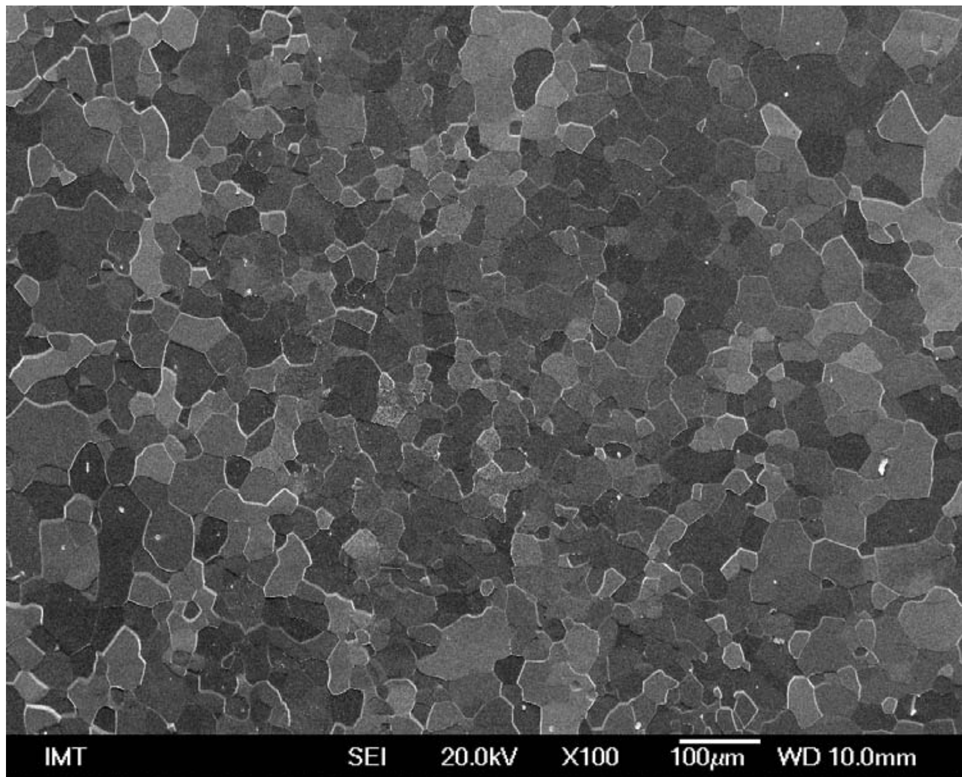

Figure 7.1: Microstructure of FeSiAl alloy, SE micrograph.

To determine the grain orientation and the texture of the specimen, I performed EBSD orientation mapping. The EBSD color-coded map (fig. 7.2) shows that there is some texture present in the specimen, but however the grains are randomly oriented and practically any desired orientation of the grain can be found. To determine the average grain orientation, I used several EBSD orientation maps at different positions to obtain data from a representative number of grains [138]. The average grain diameter determined from the EBSD measurements is 40 μm (see fig. 7.3). Grains consisting of fewer than 5 pixels were treated as errors and were eliminated from the analysis.

An inverse pole plot shows that the grains are, despite some texture, quite randomly oriented. The Z-direction inverse pole plot constructed from orientation maps is shown in fig. 7.4. Each spot in the inverse pole figure corresponds to an EBSD map point.

The specimens were also checked for homogeneity in elemental composition. To do so, I performed an EDS analysis on a number of grains, using the same size of the sampling window and microscope settings. The data shows that the specimen grains are quite homogeneous in elemental composition, within the error of the experimental technique. Some representative EDS spectra are given in fig. 7.5, and a table compiling all the EDS quantification results is given in table 7.1. The carbon was disregarded from the analysis, as it usually presents a problem to distinguish between C as a contamination element and the carbon that is actually present in the specimen [139]. The chemical

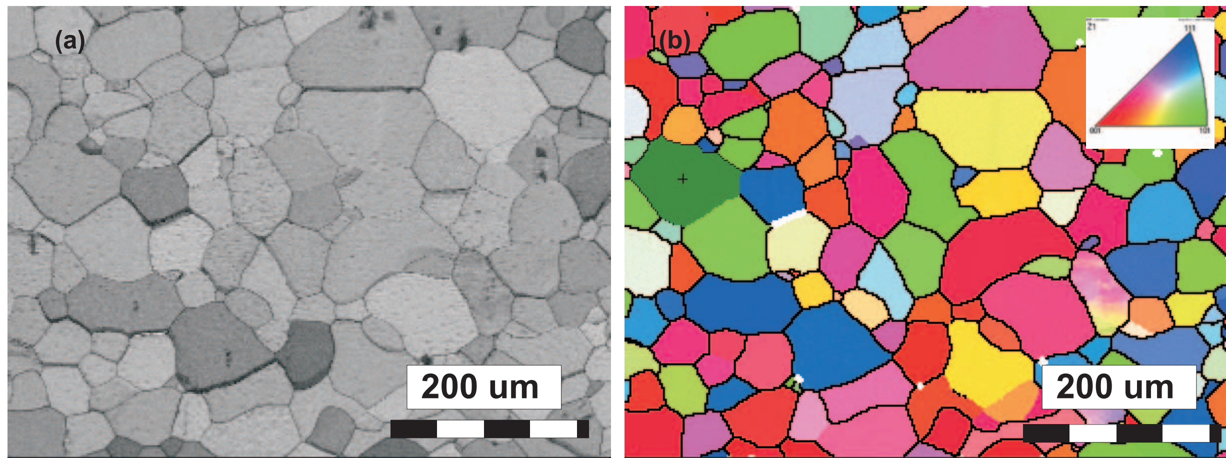

Figure 7.2: EBSD mapping of the specimen. (a) shows the "pattern quality" map, and (b) is the orientation map, where individual grains are color-coded according to their orientation.

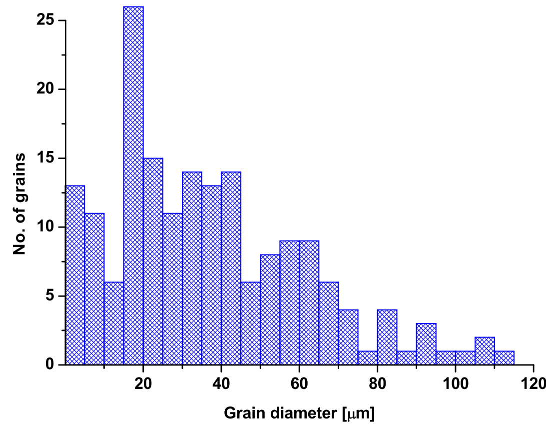

Figure 7.3: Histogram of grain sizes. The average grain diameter is 40 µ, determined from EBSD analysis.

analysis of the specimens (see table 4.1) agrees well with the EDS analysis. However, the elements of content below 0.5 mass% cannot be detected by the EDS technique.

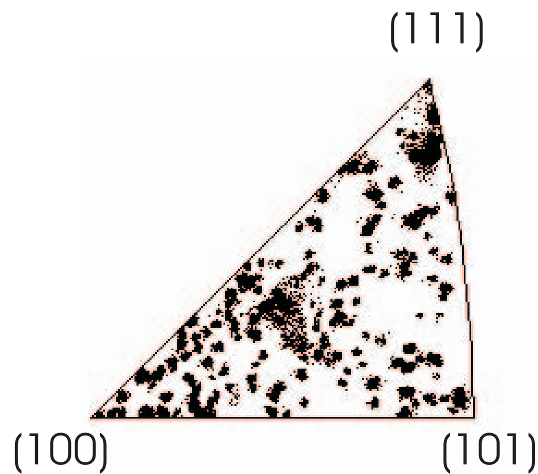

Figure 7.4: Inverse pole plot in Z-direction of the FeSiAl alloy. It can be seen that, despite some texture, no orientation dominates.

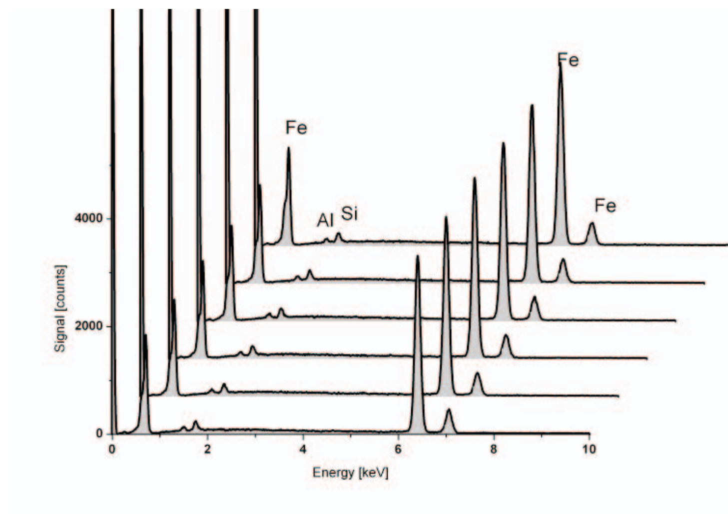

Figure 7.5: Energy dispersive spectroscopy (EDS) analysis performed on several different grains. The spectra show that the grains are homogeneous in composition within the limits of the EDS technique.

7.2 Normal incidence sputtering

Normal incidence sputtering experiments for the determination of correlation between etch pit shapes and individual crystal orientation were performed on specimens of composition B (no added Se) (see table 4.1. However, the SEM imaging of the sputtered samples of composition A (additional Se) also show the formation of etch pits with similar characteristics, which are usually even denser in this case. This could be associated with larger defect densities, which serve as initiation points for the pit formation. The pit shapes are similar in both cases.

Table 7.1: EDS analysis performed on several different grains showing the compositional differences between individual grains. The C peak was excluded from the analysis.

	Composition A			Composition B		
Spectrum	Al	Si	Fe	Al	Si	Fe
1	0.9	1.9	97.2	0.9	1.6	97.5
2	0.8	1.7	97.5	0.7	1.8	97.5
3	0.8	1.9	97.4	0.9	1.6	97.5
4	0.7	1.9	97.3	1.0	1.7	97.2
5	0.6	1.7	97.7	0.9	1.6	97.5
6	0.9	2.0	97.1	0.7	1.9	97.4
7	0.8	1.8	97.3	0.7	1.5	97.8
8	1.0	1.6	97.4	0.8	1.7	97.5
9	1.0	1.9	97.1	0.8	1.8	97.4
10	0.9	1.9	97.2	0.9	1.6	97.5

The literature [4, 15] reports on the formation of mounds and pits instead of ripple-like patterns on single crystal materials at normal incidence sputtering conditions. The features formed on (001) surfaces usually posses a square symmetry, and the exact shape depends on surface diffusion kinetics. Triangular or hexagonal pits and mounds have been observed on (111) close packed surfaces. The changes of shape and orientation have been explored and explained in kinetic Monte-Carlo simulations by a balance between growth kinetics and equilibrium shape.

However, less experimental evidence exists on pattern formation at normal incidence in the case of polycrystalline materials. Carter et. al. [17] did provide an extensive report on ion bombarded f.c.c. surfaces and the development of topography by ion beam sputtering, but made no attempt to correlate the crystallinity of the specimen with the resulting pattern, as at that time this was connected to experimental limitations. They associated pit formation with the presence of dislocations and the later development of pits was governed by enhanced sputtering yield resulting from lower atomic binding energies. The continuous growth of pits reveals the importance of crystallography of the substrate and the details of the sputtering behavior of different crystal planes.

Figure 7.6 shows an FeSiAl alloy specimen surface after 30 minute sputtering by a 6 keV beam and 250 μA current at normal incidence. It can be seen that individual grains

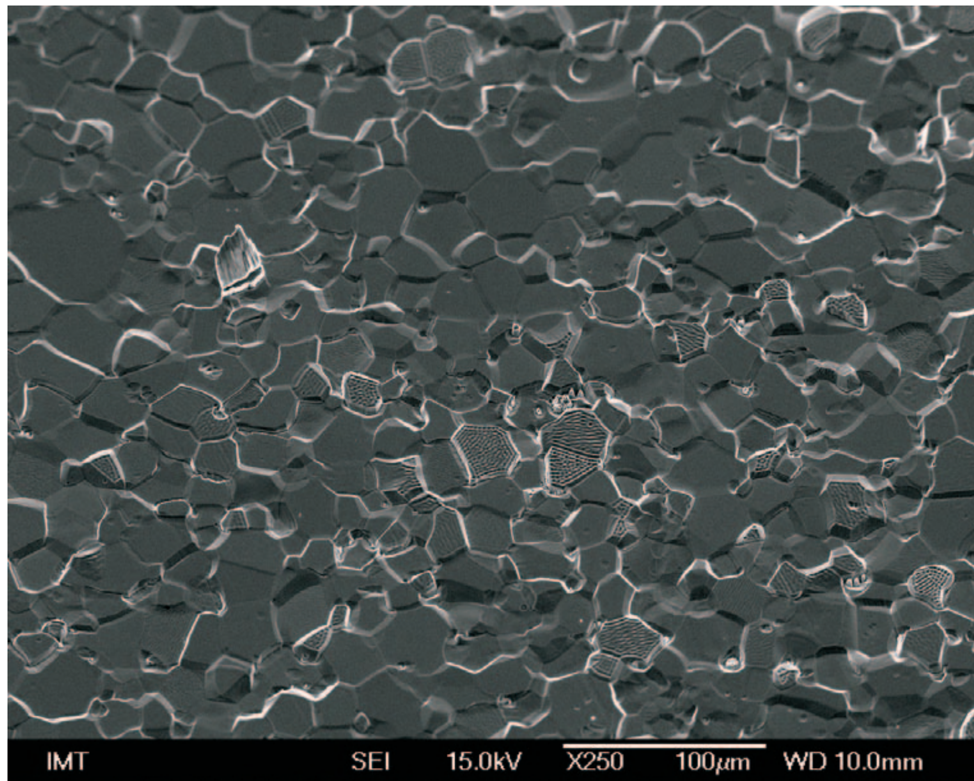

Figure 7.6: A larger-scale view of the FeSiAl alloy sputtered specimen at normal incidence conditions. The grains etch at different rates, and each grain develops an individual pattern limited by the grain boundary. The specimen was sputtered at normal incidence, 6 keV, receiving about 3×10^{18} ions/cm^2 ion fluence.

undergo different sputtering rates, which is evident from different grain heights as well as different patterns that form inside individual grains.

Individual grains show a distinguishable step between them, which can be best characterized by the AFM. Figure 7.7 shows an AFM image of three grains with a distinguished step between them. The height differences, established from the AFM profile curves, are also marked in the image. Grain step heights were determined from a number of different adjacent grains of the sputtered sample, and the steps vary in height between 20 nm and 300 nm for the case of 3×10^{18} ions/cm^2 ion fluence. This is clear evidence of grain-orientation dependent sputter yield, which has also been reported, for example, in Al polycrystalline samples [140].

The origin of this phenomenon lies in the difference of crystal plane surface densities, which is proportional to the surface binding energy. A b.c.c.-structured metal, which is the case in the alloys used in this work, has the lowest surface density for (111) crystal planes; so (111) planes should etch at a faster average rate. This has also been checked visually from EBSD data on individual crystal grains: the (111) crystal planes are lower than the neighboring grains of other orientations (compare also fig. 7.9, where it can be

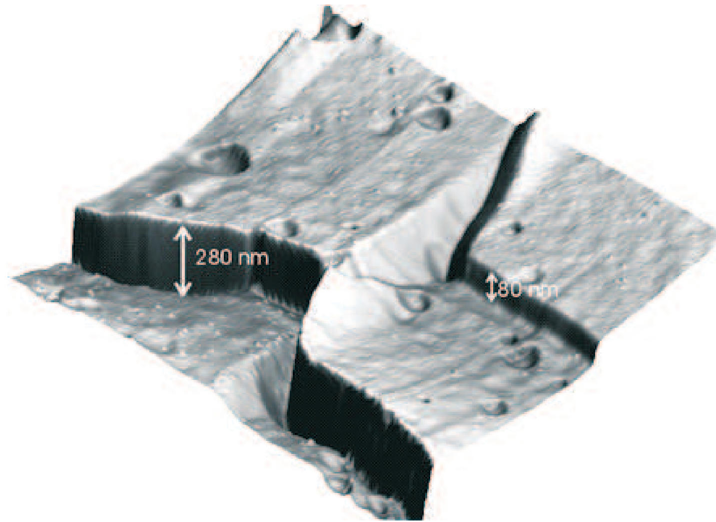

Figure 7.7: AFM image of grain boundary area. Different grains exhibit different step-heights between them. AFM scan size is 10x10 μm^2.

seen that the (111) grain is the lowest of the three neighboring grains). For example, Harrison *et al.*[141] calculated the sputter yield of three low-index Cu planes (Cu is a f.c.c. metal); (100), (110) and (111); for 600 eV Ar^+ ion bombardment. The results show that the sputter yield is the highest for the (111) plane, and lowest for the (100) plane. The ratio between these two sputter yields is 1.65; while the experimentally observed value was 1.3.

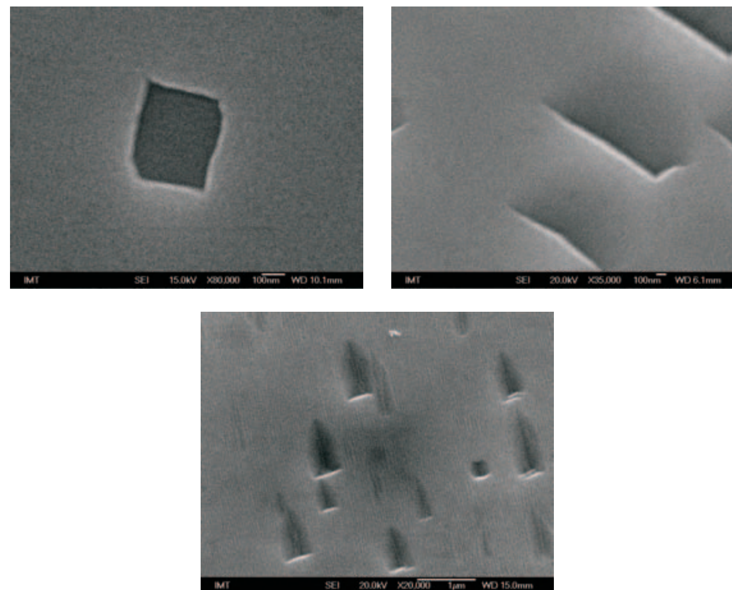

Figure 7.8: Etch pit formation - different grains exhibit different etch pit shapes, which can be generally classified into three shapes: ”square”, ”rectangular” and ”triangular”.

A close look at each individual grain reveals the presence of so-called *etch pits*. Etch-pit formation on the surface of various materials by different chemical etching techniques

is a well-known phenomenon [142, 143, 144], and chemically induced etch pits on the surface of silicon steels with similar composition have been reported as well [85]. The pits posses different shapes and symmetries, and the origin of the etch pit shape lies in the crystal structure of the specimen. Similar etch pits also form on the surface of FeSiAl alloys for normal incidence ion beam sputtering, as is shown in fig. 7.8. The pits can be classified into three general shape groups; square, rectangular and triangular.

7.2.1 Origin of the etch pits

Electron backscattered diffraction (EBSD) experiments were performed to correlate the etch pit shape with crystal orientation. The results are reported in Figure 7.9, where it is clearly seen that the etch pits shape is in fact governed by substrate orientation. Inverse pole figure in fig. 7.9 shows that the results are similar to the ones seen in chemical etching: (111) grains result in triangular pits, (100) in square pits and (110) in rectangular pits.

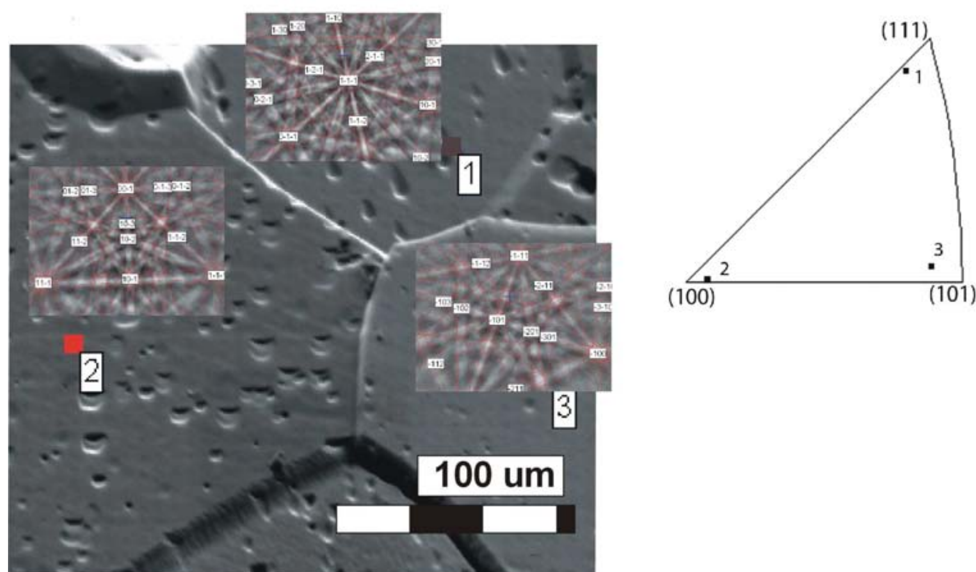

Figure 7.9: Three grains with three different orientations and their EBSD patterns. Different etch pit shapes are evident: Triangular in the case of spot 1, square in spot 2 and rectangular in spot 3. The sample has been tilted to 70° in the microscope, thus the pit shape in this image is somewhat distorted.

During chemical etching (usually employing an aqueous solution of HF and H_2O_2 for silicon steels, and numerous other etchants for other materials), the differently shaped pits form due to different etching rates of individual planes. This technique was used before the advent of the EBSD technique as an alternative way to provide information on the texture and orientation of individual grains. The shape of the pit is connected to the crystalline orientation and a similar mechanism can be employed to understand the etch-pit formation or normal incidence ion beam sputtering.

The initiation of pitting most probably is a consequence of crystal imperfections and the pits start to form at defects such as dislocations. This assumption is further supported by the non-random distribution of etch pits inside the grains. The pits are usually aligned along a certain line, or are spread in a certain direction, where the dislocations are more likely to be present.

7.3 Off-normal incidence sputtering

Normal incidence sputtering leads to the development of etch pits, but at off-normal incidence the situation is completely different. Due to a different configuration of the ion beam direction towards the specimen surface, etch pits do not form, but a wide range of surface changes can be observed.

Sputtering experiments were performed for a range of ion fluences (6×10^{17} ions/cm^2 - 1×10^{19} ions/cm^2) and ion energies (6 keV - 10 keV) with a fixed ion beam incidence angle of 60°. All observed specimens exhibit similar morphological features, with differences mainly regarding the spacing and height of the facets and ripples. Representative morphologies collected from different specimens are shown in fig. 7.10. As with etch pits, I tried to group the resulting morphologies according to their features. The four proposed ″classes″ of morphological features are the following:

- Ripples oriented *parallel* to the ion beam projection
- Ripples oriented *perpendicular* to the ion beam projection
- Triangular facet-like mound structures
- Smoother surfaces

Each grain acts as a single entity in itself. The neighboring grains can have completely different patterns, and as each grain erodes at an individual rate, this leads to visible steps between the neighboring grains. The image in fig. 7.11 shows a micrograph of the surface of a specimen sputtered at 60° and 6 keV Ar^+ beam.

Similar to the normal incidence sputtering, the origin of different patterns stems from the crystallographic orientation of that grain. To further prove this point, I performed EBSD spot analysis on individual grains and established the relationship between crystalline orientation of a particular grain and its pattern. According to the four different proposed ″pattern classes″, I was able to construct an inverse pole plot showing different grain orientations and their corresponding patterns. A larger number of grains (>50) from different specimens, all sputtered at 60° angle with beam energies of 6 keV to 10 keV, was checked in establishing this connection. The results are plotted in fig. 7.12.

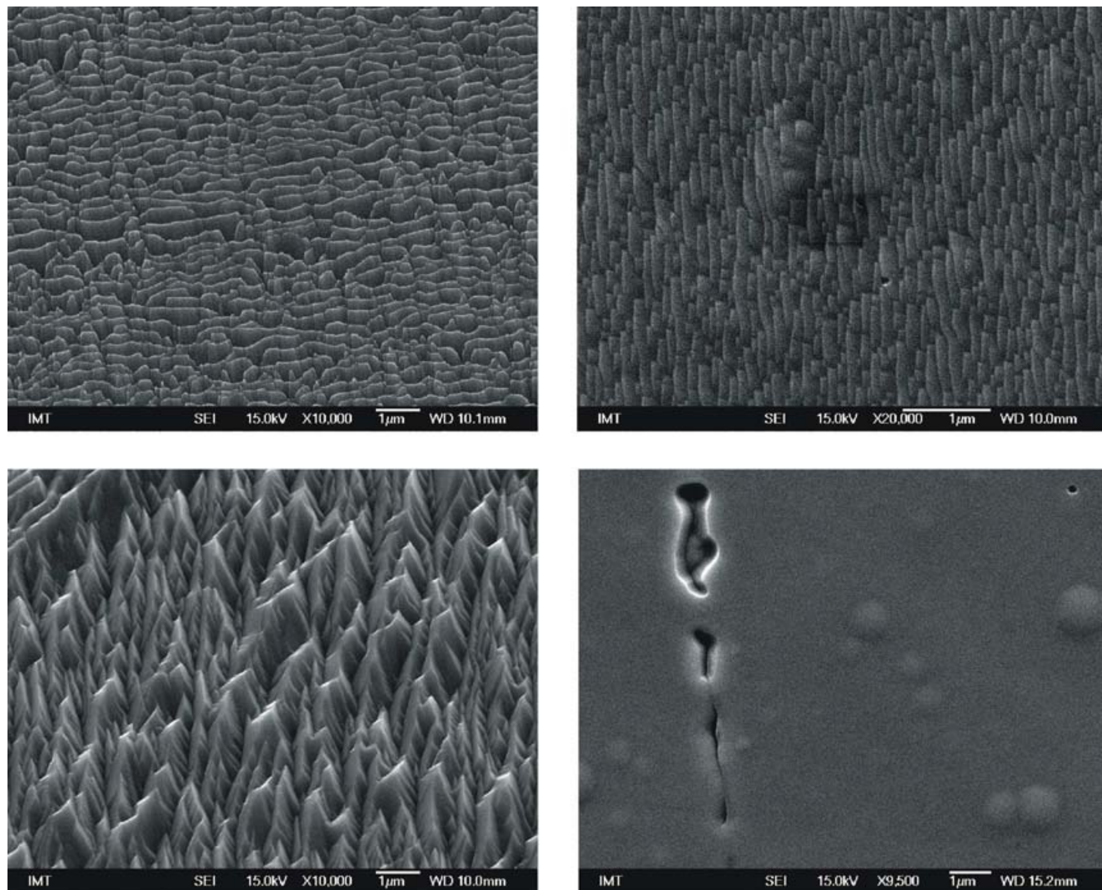

Figure 7.10: Four different classes observed in patterning Fe-Si-Al alloy with an off-normal incidence Ar^+ ion beam. The images were collected from different specimens sputtered at a 60° angle.

Similar pattern structures are grouped in the inverse pole figure. The grains belonging to the central part of the pole figure undergo ripple-like behavior, which is also the most abundant structure found. The corners belonging to (100) and (111) oriented surfaces form triangular facets and smooth grains. Ripples that are parallel to the ion beam direction are found in the (001) and the (101) corners of the inverse pole figure. It is evident that the same pattern structures fall in the same regions within the pole plot, thus showing similar orientations of the crystal structure. However, we can also observe that the (001) corner is occupied by faceted grains as well as with grains containing ripples parallel to the ion beam direction.

With this, I classified the resulting ripple patterns at normal and off-normal incidence sputtering in a polycrystalline FeSiAl alloy. The differences in patterns formed in individual grains are mostly attributed to the difference in their crystalline orientation.

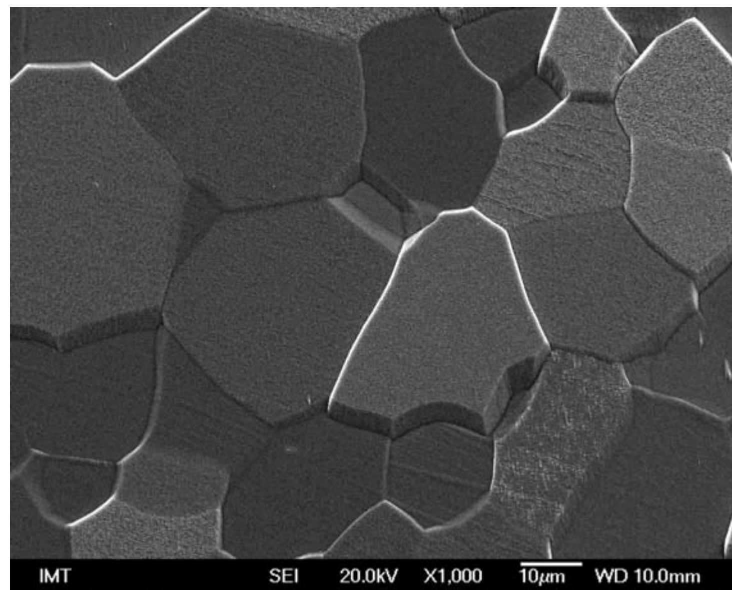

Figure 7.11: SEM micrograph of the surface of an off-normal incidence sputtered specimen. The pattern in each grain is confined to that grain, steps between individual grains are also observed.

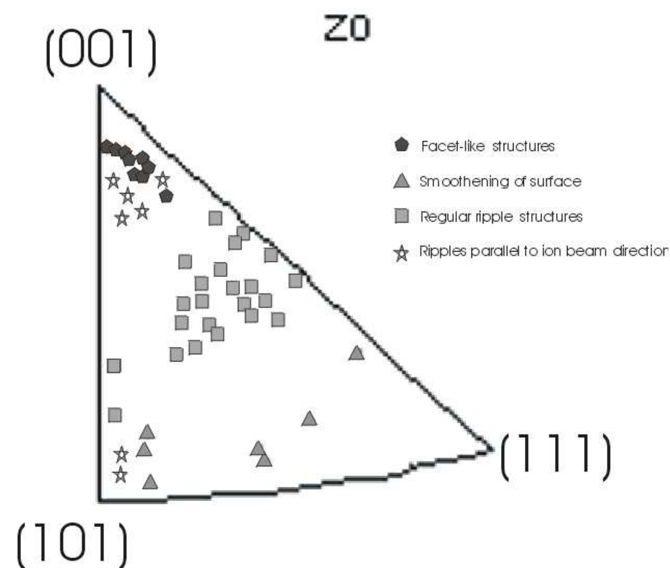

Figure 7.12: Inverse pole figure constructed from a larger number of grains showing the connection between surface crystal structure and the resulting pattern.

7.4 Single crystal substrates

In order to further validate the data obtained from polycrystalline substrates I also studied selected single crystal substrates. The main aim of this was to prove that the morphological features found on polycrystalline substrates are comparable to the ones formed on single crystals and that the grain-orientation dependence of the ion beam induced surface structures found on polycrystalline alloys can be compared to the ones formed on monocrystalline substrates of a well-defined orientation. Two types of single-crystal substrates were included: pure α-Fe (b.c.c.) single crystals and Fe-10% Si (b.c.c.) single crystals. The employed orientations were (100), (110) and (111) for both types. The Fe-10% Si single crystals were kindly provided by Dr. Pavel Lejček of the Department of Metals, Institute of Physics, Academy of Sciences of the Czech Republic.

7.4.1 Initial characterisation

For initial characterization of the specimens, I performed EDS analysis to establish that the single crystals are homogeneous in composition and that no significant amount of additional elements are present in the specimen. I also checked the single crystal orientations with the EBSD method and it has been found that the specimens are in fact single crystals of the specified orientations and crystal structures. The Fe is α-Fe, which grows in b.c.c. crystal structure, and the Fe-10% Si specimens are also in the b.c.c. crystal structure, which is also evident from the phase diagram in fig. 7.13.

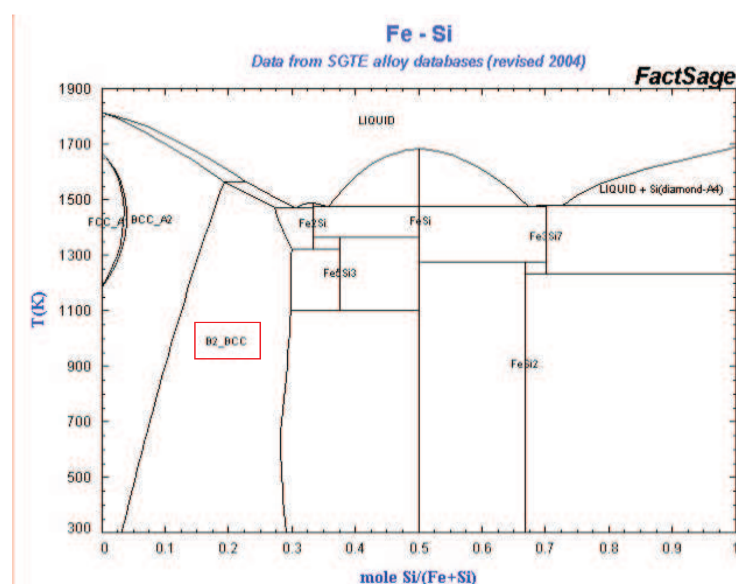

Figure 7.13: Fe-Si phase diagram. The diagram shows that Fe-10% Si has a bcc structure.

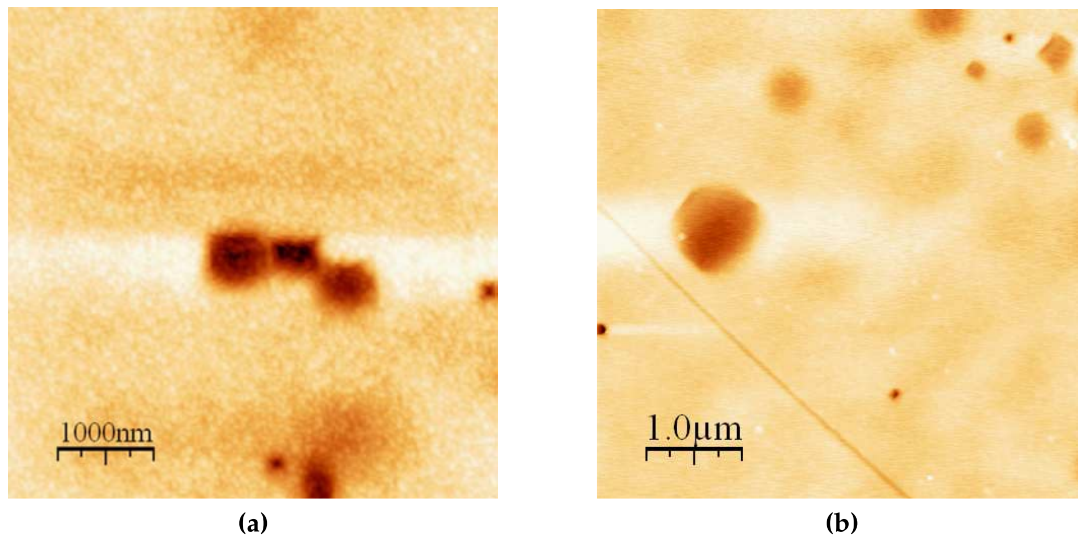

(a) (b)

Figure 7.14: Etch pits formed at normal incidence sputtering conditions in (a) monocrystalline Fe and (b) polycrystalline alloy. Both specimens were sputtered using the same conditions: 10 keV beam and 3×10^{18} ions/cm^2.

7.4.2 Etch pit formation

For normal incidence sputtering the grains of a polycrystalline alloy exhibit etch pits of characteristic shapes, which are related to the grain orientation. A similar phenomenon can be expected also for monocrystalline surfaces. The image in fig. 7.14 shows a comparison of etch pits formed on a (100) monocrystal of α-Fe and on an (100) grain of polycrystalline FeSiAl alloy. The two specimens received the same ion fluence and were both sputtered by 10 keV Ar^+ ions.

The etch pits that formed during normal incidence sputtering are comparable in α-Fe and polycrystalline FeSiAl alloy. The etch pits exhibit crystal symmetry, and thus square-shaped pits form on (100) substrate and rectangular-shaped pits can be observed on (110) substrates. SEM images further reveal the distribution, size, and positioning of the etch pits. A representative micrograph of the surface of a (100) single crystal Fe specimen, etched at normal incidence angle, is given in fig. 7.15. The pits are different in size, ranging from very small ones to large pits exceeding several μm in size. The shape of the pits is square, and the surface exhibits some rough structure. In the case of normal incidence ion sputtering of (110) surfaces of Fe single crystal, I observe rectangular etch pits that are shown in fig. 7.16.

From this data, it can be concluded that the formation of crystal-orientation dependent etch pits is also present in single-crystal α-Fe. The (100) surface exhibits, along with square etch pits, some non-periodic roughnening of the surface, while in the case of the (110) surface very regular ripple-like structures with wavelengths of approximately 200 nm are present. This is visible in fig. 7.16b.

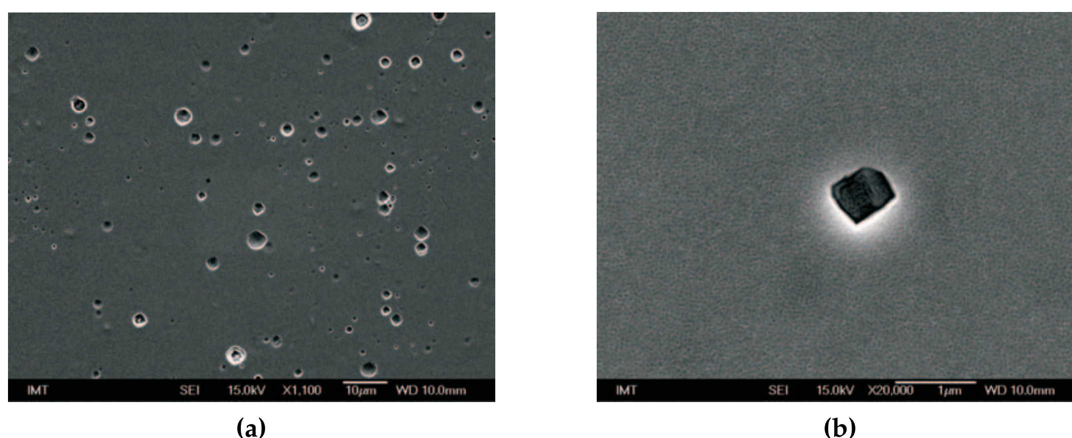

(a) (b)

Figure 7.15: SEM micrograph of a (100) single crystal Fe specimen sputtered at normal incidence employing a 10 keV Ar^+ and ion fluence of 3×10^{18} ions/cm^2.

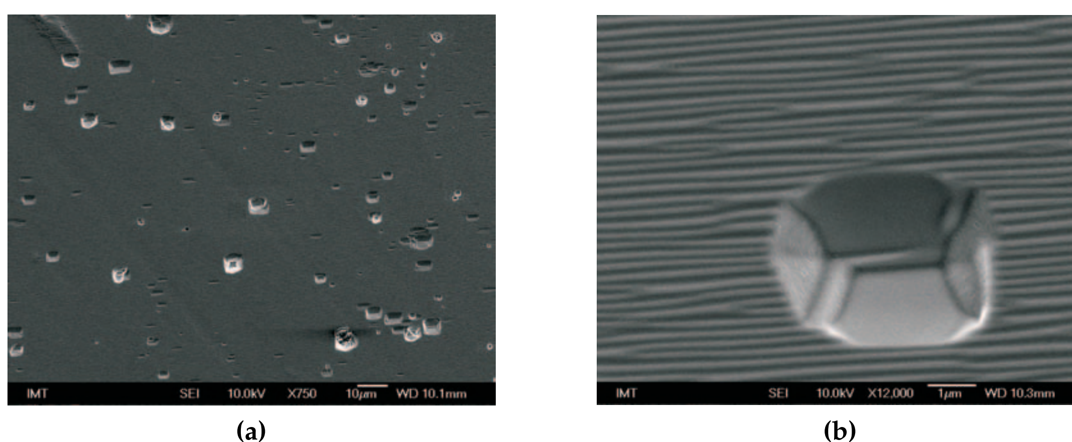

(a) (b)

Figure 7.16: SEM micrograph of the (110) single crystal Fe specimen sputtered at normal incidence employing a 10 keV Ar^+ and ion fluence of 3×10^{18} ions/cm^2.

However, the case of Fe-10% Si is significantly different. Even though the crystal still has a b.c.c. structure (as is evident from the Fe-Si phase diagram, shown in fig. 7.13), the surface did not exhibit visible etch pits, even for prolonged sputter times (up to three hours at 10 keV and 500 μA current, corresponding to an ion fluence of $4\times10^{1}9$ ions/cm^2), but only some degree of surface roughening is present. The (111) surface is marginally rougher than the (100) surface for the same ion dose. The roughness plot and the corresponding surface AFM images are given in fig. 7.17. The images show that a similar pattern forms on both specimens, regardless of the orientation. The surface is also quite smooth compared to the polycrystalline alloys that received the same ion dose.

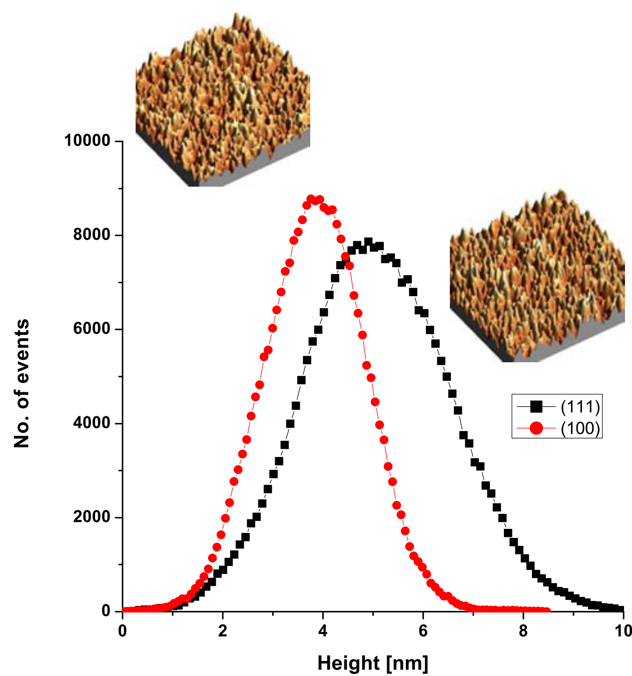

Figure 7.17: Roughness of normal incidence sputtered specimens of Fe-10% Si at (111) and (100) orientations. The AFM image size is 10 × 10 µm in both cases. The single crystal substrates received $3{\times}10^{18}$ ions/cm^2 and the beam energy was 10 keV.

8 Conclusions

I have investigated ion beam sputtering of metallic substrates - polycrystalline thin films, polycrystalline FeSiAl alloys and single crystal substrates. The wide range of materials used shows the possibility of controlled patterning of different substrates and again confirms that ion beam sputtering is an important tool in nanostructuring the surface. Thin films were patterned at an off-normal incidence angle while the polycrystalline bulk substrates were sputtered also at normal incidence.

Thin polycrystalline films used were Au films, deposited by different deposition methods to achieve different starting surfaces. The films consisted of grains in the range of 50 - 150 nm, which is the order of magnitude of the resulting ripples during ion beam sputtering at a grazing angle. The surfaces were sputtered by 800 eV Ar^+ ion beam and the time-evolution of the surface was examined by AFM and SEM. It has been shown that the initial wavelength selection process is governed by the grain size and grain size distribution, which has been previously not mentioned in publications regarding ion beam patterning of thin films. The mechanism responsible for this is the *shadowing mechanism*, which leads to accelerated patterning of the thin films compared to flat substrates.

Polycrystalline alloys that were used in the experimental work were FeSiAl alloys, also known as electrical or silicon steels. The materials are non-oriented and grains have a specific grain orientation, which has been measured by EBSD. The grains pattern in an individual way, thus two adjacent grains have a structure that can be completely dif-

ferent. However, here the governing mechanism is the orientation of individual grain: grains with similar orientations exhibit the same pattern.

To show that the pattern formed in individual grains is mainly due to the orientation, I correlated the individual grain orientations with the patterns that form in that grain at normal incidence and at an off-normal incidence angle. At normal incidence, I observed the formation of etch pits of a specific shape for individual orientation, and at off-normal incidence angle, four different possible pattern classes were observed.

To cross-check the validity of these results, I also included normal-incidence sputtering of single crystal materials: Fe(110) and Fe(100), and Fe-10% Si (100) and (111). In the Fe single crystals I also observed the formation of etch pits of square shape in the case of (100) and retangular shape in the case of (110), but for the Fe-10% single crystals only roughening with no specific pattern was observed.

8.1 Contribution to science

The work presented in this doctoral dissertation explored ion beam sputtering of polycrystalline materials, a class of materials that have not been regularly included in experimental studies. Most publications dealing with ion beam induced morphological changes employ single crystal or amorphous substrates to eliminate the effect of individual grains of different sizes and orientations. However, with the advent of new techniques that enable determination of individual crystal grain orientation, such as electron backscatter diffraction (EBSD), sputter-induced morphology studies can be controllably performed also on cheaper and more widely available polycrystalline materials, adding new knowledge to the field.

The results in this thesis have been presented in four papers in SCI international journals and at national and international conferences.

Acknowledgments

This work would not be possible without the help and support of many people.

First, I would like to sincerely thank my mentor, Prof. Dr. Monika Jenko, for her guidance during my study years and for providing the opportunity to perform research work at the Institute of Metals and Technology.

A part of this work was performed at the University of Genova, Department of Physics. Prof. Dr. Francesco Buatier de Mongeot and his group, especially Dr. Andrea Toma and Daniele Chiappe, have been extremely hospitable during my stay - thank you for a wonderful experience.

Prof. Dr. Dragan Mihailović kindly provided access to atomic force microscopy facilities, and Jure Strle was always there to rescue me from blunt tips and lasers that did not want to center themselves. Thank you.

A sincere thank you to the members of the evaluation board, for pointing out the inconsistencies, providing many useful suggestions and all the comments that helped improve this work. Any mistakes that still remain are solely mine...

As a physicist in an environment consisting mainly of materials scientists and metallurgists, I had a lot to learn. My co-workers have guided me through the process, adding bits of knowledge at the right times. Dr. Matjaž Godec introduced me into the magnificent world of electron microscopy and has been a wonderful teacher since my first day. Nataša Lipovšek guided me through the process of specimen preparation and other secrets of metallography.

I have shared many young researcher woes with Ažbe Križaj, Dr. Črtomir Donik and Irena Paulin. Thank you.

Last, but not least: a big thank you to my family, who have all stood by me.

References

[1] Peter J. Hesketh. *BioNanoFluidic MEMS*, pages 63–130. Springer, 2008.

[2] Theodore E. Madey, Robert E. Johnson, and Thom M. Orlando. Far-out surface science: radiation-induced surface processes in the solar system. *Surface Science*, 500(1-3):838 – 858, 2002.

[3] W. L. Brown, L. J. Lanzerotti, and R. E. Johnson. Fast ion bombardment of ices and its astrophysical implications. *Science*, 218(4572):525–531, 1982.

[4] Wai Lun Chan and Eric Chason. Making waves: Kinetic processes controlling surface evolution during low energy ion sputtering. *Journal of Applied Physics*, 101 (12):121301, 2007.

[5] T. M. Mayer, E. Chason, and A. J. Howard. Roughening instability and ion-induced viscous relaxation of SiO_2 surfaces. *Journal of Applied Physics*, 76(3):1633–1643, 1994.

[6] B. Ziberi, M. Cornejo, F. Frost, and B. Rauschenbach. Highly ordered nanopatterns on Ge and Si surfaces by ion beam sputtering. *Journal of Physics - Condensed Matter*, 21(22), 2009.

[7] S Rusponi, G Costantini, FB de Mongeot, C Boragno, and U Valbusa. Patterning a surface on the nanometric scale by ion sputtering. *Applied Physics Letters*, 75(21): 3318–3320, 1999.

[8] O Malis, JD Brock, RL Headrick, MS Yi, and JM Pomeroy. Ion-induced pattern formation on Co surfaces: An X-ray scattering and kinetic Monte Carlo study. *Physical Review B*, 66(3), 2002.

[9] R Reiche and W Hauffe. Pyramid formation on a high index copper bicrystal during bombardment with 10 keV argon and krypton ions. *Applied Surface Science*, 165(4):279–287, 2000.

[10] Heiji Watanabe and Masakazu Ichikawa. Layer-by-layer sputtering of Si(111) and (001) surfaces mediated by surface vacancy diffusion: Surface physics and application for nanofabrication. *Journal of Vacuum Science and Technology B*, 15(6): 2666–2671, 1997.

[11] Heiji Watanabe and Masakazu Ichikawa. Initial stage of layer-by-layer sputtering of Si(111) surfaces studied by scanning reflection electron microscopy. *Applied Physics Letters*, 68(18):2514–2516, 1996.

[12] F. Frost, R. Fechner, B. Ziberi, J. Voellner, D. Flamm, and A. Schindler. Large area smoothing of surfaces by ion bombardment: fundamentals and applications. *Journal of Physics - Condensed Matter*, 21(22), 2009.

[13] A. Keller, A. Biermanns, G. Carbone, J. Grenzer, S. Facsko, O. Plantevin, R. Gago, and T. H. Metzger. Transition from smoothing to roughening of ion-eroded GaSb surfaces. *Applied Physics Letters*, 94(19), 2009.

[14] M. Ritter, M. Stindtmann, M. Farle, and K. Baberschke. Nanostructuring of the Cu(001) surface by ion bombardment: a STM study. *Surface Science*, 348(3):243 – 252, 1996.

[15] U Valbusa, C Boragno, and F Buatier de Mongeot. Nanostructuring surfaces by ion sputtering. *Journal of Physics: Condensed Matter*, 14(35):8153–8175, 2002.

[16] M. Navez, C. Sella, and D. Chaperot. Microscopie electronique—étude de lattaque du verrepar bombardement ionique. *Comptes Rendus de l'Académie des Sciences*, 254 (2):240, 1962.

[17] G. Carter, M. J. Nobes, and J. L. Whitton. Sputtering induced topography development on fcc metals. *Applied Physics A - Materials Science & Processing*, 38(2): 77–95, 1985.

[18] ADG Stewart. Investigation of the topography of ion bombarded surfaces with a scanning electron microscope. *Advances in imaging and electron physics*, 133:175–178, 2004.

[19] R. M. Bradley and J. M. E. Harper. Theory of ripple topography induced by ion-bombardment. *Journal of Vacuum Science & Technology A-Vacuum, Surfaces, and Films*, 6(4):2390–2395, 1988.

[20] Richard L. Schwoebel. Step motion on crystal surfaces. II. *Journal of Applied Physics*, 40(2):614–618, 1969.

[21] Eric Chason and Bruce K. Kellerman. Monte Carlo simulations of ion-enhanced island coarsening. *Nuclear Instruments and Methods in Physics Research Section B: Beam Interactions with Materials and Atoms*, 127-128:225 – 229, 1997.

[22] I. Koponen, M. Hautala, and O.-P. Sievänen. Simulations of ripple formation on ion-bombarded solid surfaces. *Physical Review Letters*, 78(13):2612–2615, 1997.

[23] I. Koponen, M. Hautala, and O.-P. Sievänen. Simulations of submicrometer-scale roughening on ion-bombarded solid surfaces. *Physical Review B*, 54(19):13502–13505, 1996.

[24] M. C. Moore, N. Kalyanasundaram, J. B. Freund, and H. T. Johnson. Structural and sputtering effects of medium energy ion bombardment of silicon. *Nuclear Instruments and Methods in Physics Research Section B: Beam Interactions with Materials and Atoms*, 225(3):241 – 255, 2004.

[25] Mai Ghaly and R. S. Averback. Effect of viscous flow on ion damage near solid surfaces. *Phys. Rev. Lett.*, 72(3):364–367, 1994.

[26] G Carter. The effects of ion bombardment sputtering and atomic transport related roughening and smoothing on depth profiling resolution. *Vacuum*, 47(5):409–420, 1996.

[27] G Carter. Theory of ripple topography inhibition in depth profiling with sample rocking. *Applied Physics Letters*, 71(21):3066–3068, 1997.

[28] A Zalar. Significance of sample rotation in Auger-electron spectroscopy sputter depth profiling of thin films. *Thin solid films*, 193(1-2):258–269, 1990.

[29] A Zalar, S Hofmann, and P Panjan. Auger-electron spectroscopy depth profiling of metal/oxide multilayer structures. *Thin solid films*, 206(1-2):327–329, 1991.

[30] S Hofmann and A Zalar. Depth profiling with sample rotation - capabilities and limitations. *Surface and Interface Analysis*, 21(5):304–309, 1994.

[31] R. Mark Bradley and Eun-Hee Cirlin. Theory of improved resolution in depth profiling with sample rotation. *Applied Physics Letters*, 68(26):3722–3724, 1996.

[32] E. Chason and W. L. Chan. Kinetic phase diagram for morphological evolution on Cu(001) surfaces during ion bombardment. *Nuclear Instruments & Methods in Physics Research Section B-Beam Interactions with Materials and Atoms*, 256(1):305–312, 2007. Chason, Eric Chan, Wai Lun.

[33] Conyers Herring. Effect of change of scale on sintering phenomena. *Journal of Applied Physics*, 21(4):301–303, 1950.

[34] William W. Mullins. Flattening of a nearly plane solid surface due to capillarity. *Journal of Applied Physics*, 30(1):77–83, 1959.

[35] A. Toma, F. B. de Mongeot, R. Buzio, G. Firpo, S. R. Bhattacharyya, C. Boragno, and U. Valbusa. Ion beam erosion of amorphous materials: evolution of surface morphology. *Nuclear Instruments and Methods in Physics Research Section B - Beam Interactions with Materials and Atoms*, 230:551–554, 2005. Sp. Iss. SI.

[36] A. Karen, K. Okuno, F. Soeda, and A. Ishitani. A study of the secondary-ion yield change on the GaAs surface caused by the O_2^+ ion-beam-induced rippling. *Journal of Vacuum Science & Technology A: Vacuum, Surfaces, and Films*, 9(4):2247–2252, 1991.

[37] Jonah Erlebacher, Michael J. Aziz, Eric Chason, Michael B. Sinclair, and Jerrold A. Floro. Spontaneous pattern formation on ion bombarded Si(001). *Phys. Rev. Lett.*, 82(11):2330–2333, 1999.

[38] Ari-David Brown and Jonah Erlebacher. Temperature and fluence effects on the evolution of regular surface morphologies on ion-sputtered Si(111). *Physical Review B*, 72(7):075350, 2005.

[39] B. Ziberi, F. Frost, Th. Höche, and B. Rauschenbach. Ripple pattern formation on silicon surfaces by low-energy ion-beam erosion: Experiment and theory. *Physical Review B*, 72(23):235310, 2005.

[40] Gert Ehrlich and F. G. Hudda. Atomic view of surface self-diffusion: Tungsten on Tungsten. *The Journal of Chemical Physics*, 44(3):1039–1049, 1966.

[41] J. Villain. Continuum models of crystal growth from atomic beams with and without desorption. *Journal de Physique I*, (1):19–42, 1991.

[42] Artem Levandovsky and Leonardo Golubović. Epitaxial growth and erosion on (001) crystal surfaces: Far-from-equilibrium transitions, intermediary states, and vertical asymmetry. *Physical Review B*, 69(24):241402, 2004.

[43] Leonardo Golubović, Artem Levandovsky, and Dorel Moldovan. Epitaxial growth and erosion on (110) crystal surfaces: Structure and dynamics of interfacial states. *Phys. Rev. Lett.*, 89(26):266104, 2002.

[44] G Costantini, S Rusponi, F Buatier de Mongeot, C Boragno, and U Valbusa. Periodic structures induced by normal-incidence sputtering on Ag(110) and Ag(001): flux and temperature dependence. *Journal of Physics: Condensed Matter*, 13(26): 5875, 2001.

[45] P Bedrossian and T Klitsner. Surface reconstruction in layer-by-layer sputtering of Si(111). *Physical Review B*, 44(24):13783–13786, 1991.

[46] E Chason, P Bedrossian, JE Houston, JY Tsao, BW Dodson, and ST Picraux. Simulations of layer-by-layer sputtering erosion. *Applied Physics Letters*, 59(27):3533–3535, 1991.

[47] J. Tersoff, A. W. Denier van der Gon, and R. M. Tromp. Critical island size for layer-by-layer growth. *Phys. Rev. Lett.*, 72(2):266–269, 1994.

[48] D. Cvetko, V. De Renzi, L. Floreano, A. Morgante, M. Peloi, F. Tommasini, V. Cháb, and K. C. Prince. Inverse growth kinetics on insb(110). *Surface Science*, 323(3):L305 – L310, 1995.

[49] MVR Murty, AJ Couture, BH Cooper, AR Woll, JD Brock, and RL Headrick. Persistent layer-by-layer sputtering of Au(111). *Journal of Applied Physics*, 88(1):597–599, 2000.

[50] P. Bedrossian, J. E. Houston, J. Y. Tsao, E. Chason, and S. T. Picraux. Layer-by-layer sputtering and epitaxy of si(100). *Physical Review Letters*, 67(1):124–127, 1991.

[51] Thomas Michely and George Comsa. Generation and nucleation of adatoms during ion bombardment of Pt(111). *Physical Review B*, 44(15):8411–8414, 1991.

[52] Thomas Michely and Christian Teichert. Adatom yields, sputtering yields, and damage patterns of single-ion impacts on Pt(111). *Physical Review B*, 50(15):11156–11166, 1994.

[53] Markus Morgenstern, Thomas Michely, and George Comsa. Collective effects in the adatom production by 4.5 keV rare-gas impacts on Pt(111): A low-temperature scanning tunnelling microscopy analysis. *Philosophical Magazine A*, 79:775, 1999.

[54] Toshio Seki, Takaaki Aoki, Jiro Matsuo, and Isao Yamada. STM observation of surface vacancies created by ion impact. *Nuclear Instruments and Methods in Physics Research Section B: Beam Interactions with Materials and Atoms*, 164-165:650 – 655, 2000.

[55] K Mochiji, S Yamamoto, H Shimizu, S Ohtani, T Seguchi, and N Kobayashi. Scanning tunneling microscopy and atomic force microscopy study of graphite defects produced by bombarding with highly charged ions. *Journal of Applied Physics*, 82 (12):6037–6040, 1997.

[56] B An, S Fukuyama, K Yokogawa, and M Yoshimura. Evolution of Ar^+-damaged graphite surface during annealing as investigated by scanning probe microscopy. *Journal of Applied Physics*, 92(5):2317–2322, 2002.

[57] X.-S. Wang, R. J. Pechman, and J. H. Weaver. Interaction of 300 - 5000 eV ions with GaAs(110). *Applied Physics Letters*, 65(22):2818–2820, 1994.

[58] PJ Bedrossian and TD de la Rubia. Surface segregation of low-energy ion-induced defects in Si. *Journal of Vacuum Science & Technology A - Vacuum, Surfaces and Films*, 16(3, Part 1):1043–1046, 1998.

[59] RS Averback and M Ghaly. A model for surface damage in ion-irradiated solids. *Journal of Applied Physics*, 76(6):3908–3910, 1994.

[60] M Ghaly and RS Averback. The formation of vacancy-type defect clusters by ion bombardment - a problem revisited by molecular-dynamics. *Journal of Physics and Chemistry of Solids*, 55(10):945–953, 1994.

[61] M Ghaly, RS Averback, and TD Delarubia. Surface effects on damage production during ion bombardment - A molecular-dynamics study. *Nuclear Instruments & Methods in Physics Research Section B-Beam Interactions with Materials and Atoms*, 102(1-4):51–57, 1995.

[62] Ramona S. Taylor and Barbara J. Garrison. Molecular dynamics simulations of keV particle bombardment. Correlation of intact molecular ejection with adsorbate size. *Chemical Physics Letters*, 230(6):495 – 500, 1994.

[63] Kathleen E. Ryan, Edward J. Smiley, Nicholas Winograd, and Barbara J. Garrison. Angle of incidence effects in a molecular solid. *Applied Surface Science*, 255(4):844 – 846, 2008.

[64] Roger Smith, Don E. Harrison, and Barbara J. Garrison. kev particle bombardment of semiconductors: A molecular-dynamics simulation. *Phys. Rev. B*, 40(1):93, 1989.

[65] Debabrata Ghose. Ion beam sputtering induced nanostructuring of polycrystalline metal films. *Journal of Physics - Condensed Matter*, 21(22), 2009.

[66] P. Romero-Gomez, A. Palmero, F. Yubero, M. Vinnichenko, A. Kolitsch, and A.R. Gonzalez-Elipe. Surface nanostructuring of TiO2 thin films by ion beam irradiation. *Scripta Materialia*, 60(7):574 – 577, 2009.

[67] P. Mishra and D. Ghose. Effect of initial target surface roughness on the evolution of ripple topography induced by oxygen sputtering of Al films. *Journal of Applied Physics*, 105(1):014304, 2009.

[68] P. Karmakar and D. Ghose. Ion beam sputtering induced ripple formation in thin metal films. *Surface Science*, 554(2-3):L101 – L106, 2004.

[69] P. Mishra and D. Ghose. Formation of nanoripples in Al films during O^2+ sputtering. *Physical Review B*, 74(15):155427, 2006.

[70] J. Krim, I. Heyvaert, C. Van Haesendonck, and Y. Bruynseraede. Scanning tunneling microscopy observation of self-affine fractal roughness in ion-bombarded film surfaces. *Physical Review Letters*, 70(1):57–60, 1993.

[71] M Stepanova and S K Dew. Ion beam sputtering nanopatterning of thin metal films: the synergism of kinetic self-organization and coarsening. *Journal of Physics: Condensed Matter*, 21(22):224014, 2009.

[72] M. Stepanova, S. K. Dew, and I. P. Soshnikov. Sputtering from ion-beam-roughened cu surfaces. *Physical Review B*, 66(12):125407, 2002.

[73] Alexander K. Hartmann, Reiner Kree, Ulrich Geyer, and Matthias Kölbel. Long-time effects in a simulation model of sputter erosion. *Physical Review B*, 65(19):193403, 2002.

[74] M. Stepanova, S. K. Dew, and I. P. Soshnikov. Copper nanopattern on SiO_2 from sputter etching a Cu/SiO_2 interface. *Applied Physics Letters*, 86(7):073112, 2005.

[75] M. Stepanova and S. K. Dew. Discrete-path transport theory of physical sputtering. *Journal of Applied Physics*, 92(3):1699–1708, 2002.

[76] M. Stepanova and S. K. Dew. Self-organized Cu nanowires on glass and Si substrates from sputter etching Cu/substrate interfaces. *Journal of Vacuum Science & Technology B: Microelectronics and Nanometer Structures*, 24(2):592–598, 2006.

[77] S Rusponi, G Costantini, FB de Mongeot, C Boragno, and U Valbusa. Patterning a surface on the nanometric scale by ion sputtering. *Applied Physics Letters*, 75(21): 3318–3320, 1999.

[78] S Rusponi, C Boragno, and U Valbusa. Ripple structure on Ag(110) surface induced by ion sputtering. *Physical Review Letters*, 78(14):2795–2798, 1997.

[79] Rodolfo Cuerno and Albert-László Barabási. Dynamic scaling of ion-sputtered surfaces. *Physical Review Letters*, 74(23):4746–4749, 1995.

[80] Maxim A. Makeev and Albert-László Barabási. Ion-induced effective surface diffusion in ion sputtering. *Applied Physics Letters*, 71(19):2800–2802, 1997.

[81] K Fichthorn and M Scheffler. Nanophysics - A step up to self-assembly. *Nature*, 429(6992):617–618, 2004.

[82] M Strobel, KH Heinig, and T Michely. Mechanisms of pit coarsening in ion erosion of fcc(111) surfaces: a kinetic 3D lattice Monte-Carlo study. *Surface Science*, 486(1-2):136–156, 2001.

[83] Gottfried K. Wehner. *Sputtering by Ion Bombardment*, volume 7 of *Advances in Electronics and Electron Physics*, pages 239 – 298. Academic Press, 1955.

[84] B. B. Meckel and R. A. Swalin. Selective delineation of screw dislocations by cathodic sputtering. *Journal of Applied Physics*, 30(1):89–93, 1959.

[85] M. Godec, M. Jenko, F. Vodopivec, M. Ambrožič, Dj. Mandrino, L. Kosec, and M. Lovrečič Saražin. Določanje teksture z metodo jedkalnih figur - determination of microtexture by method of etch figures. *Kovine zlitine tehnologije*, 28:105–109, 1994.

[86] M. Kalff, G. Comsa, and T. Michely. Temperature dependent morphological evolution of Pt(111) by ion erosion: destabilization, phase coexistence and coarsening. *Surface Science*, 486(1-2):103–135, 2001.

[87] Thomas Michely, Matthias Kalff, George Comsa, Matthias Strobel, and Karl-Heinz Heinig. Step edge diffusion and step atom detachment in surface evolution: Ion erosion of Pt(111). *Phys. Rev. Lett.*, 86(12):2589–2592, 2001.

[88] M. V. Ramana Murty, T. Curcic, A. Judy, B. H. Cooper, A. R. Woll, J. D. Brock, S. Kycia, and R. L. Headrick. X-ray scattering study of the surface morphology of Au(111) during Ar^+ ion irradiation. *Phys. Rev. Lett.*, 80(21):4713–4716, 1998.

[89] MVR Murty, T Curcic, A Judy, BH Cooper, AR Woll, JD Brock, S Kycia, and RL Headrick. Real-time X-ray scattering study of surface morphology evolution during ion erosion and epitaxial growth of Au(111). *Physical Review B*, 60(24): 16956–16964, 1999.

[90] V Repain, JM Berroir, S Rousset, and J Lecoeur. Interaction between steps and reconstruction on Au(111). *Europhysics Letters*, 47(4):435–441, 1999.

[91] C Boragno, FB de Mongeot, G Costantini, U Valbusa, R Felici, DM Smilgies, and S Ferrer. Ion etching of Ag(110) studied by X-ray and STM. *Nuclear Instruments & Methods in Physics Research Section B - Beam Interactions with Materials and Atoms*, 193:590–595, 2002.

[92] C Boragno, FB de Mongeot, G Costantini, U Valbusa, R Felici, DM Smilgies, and S Ferrer. In situ X-ray scattering study of Ag(110) nanostructuring by ion erosion. *Physical Review B*, 65(15), 2002.

[93] S. Facsko, H. Kurz, and T. Dekorsy. Energy dependence of quantum dot formation by ion sputtering. *Physical Review B*, 63(16):165329, 2001.

[94] T. Bobek, S. Facsko, H. Kurz, T. Dekorsy, M. Xu, and C. Teichert. Temporal evolution of dot patterns during ion sputtering. *Physical Review B*, 68(8):085324, 2003.

[95] A. Ronda and I. Berbezier. Self-patterned Si surfaces as templates for Ge islands ordering. *Physica E: Low-dimensional Systems and Nanostructures*, 23(3-4):370 – 376, 2004. Proceedings of the Fifth International Workshop on Epitaxial Semiconductors on Patterned Substrates and Novel Index Surfaces (ESPS-NIS).

[96] S. Facsko, T. Bobek, H. Kurz, T. Dekorsy, S. Kyrsta, and R. Cremer. Ion-induced formation of regular nanostructures on amorphous GaSb surfaces. *Applied Physics Letters*, 80(1):130–132, 2002.

[97] Francesca Granone, V. Mussi, A. Tommie, S. Orlanducci, M.L. Terranova, C. Boragno, F. Buatier de Mongeot, and U. Valbusa. Ion sputtered surfaces as templates for carbon nanotubes alignment and deformation. *Nuclear Instruments and Methods in Physics Research Section B: Beam Interactions with Materials and Atoms*, 230 (1-4):545 – 550, 2005.

[98] Dale F. Johnson and W. Henry Weinberg. Quantitative determination of the activity of defect sites on a single-crystalline surface: C–H bond activation of carbon-13 labeled ethane on Ir(111). *The Journal of Chemical Physics*, 101(7):6289–6300, 1994.

[99] Dale F. Johnson and W. Henry Weinberg. Quantification of the influence of surface structure on C–H bond activation by Iridium and Platinum. *Science*, 261(5117):76–78, 1993.

[100] G. Costantini, F. Buatier de Mongeot, S. Rusponi, C. Boragno, U. Valbusa, L. Vattuone, U. Burghaus, L. Savio, and M. Rocca. Tuning surface reactivity by in situ surface nanostructuring. *The Journal of Chemical Physics*, 112(15):6840–6843, 2000.

[101] F. Buatier de Mongeot, A. Toma, A. Molle, S. Lizzit, L. Petaccia, and A. Baraldi. Carbon monoxide dissociation on Rh nanopyramids. *Physical Review Letters*, 97 (5):056103, 2006.

[102] M T Johnson, P J H Bloemen, F J A den Broeder, and J J de Vries. Magnetic anisotropy in metallic multilayers. *Reports on Progress in Physics*, 59(11):1409, 1996.

[103] R Skomski. Nanomagnetics. *Journal of Physics: Condensed Matter*, 15(20):R841, 2003.

[104] C A F Vaz, J A C Bland, and G Lauhoff. Magnetism in ultrathin film structures. *Reports on Progress in Physics*, 71(5):056501, 2008.

[105] R. Moroni, F. Bisio, F. Buatier de Mongeot, M. Canepa, C. Boragno, U. Valbusa, and L. Mattera. Onset of magnetic anisotropy in ion-sculpted ultrathin magnetic films. *Nuclear Instruments and Methods in Physics Research Section B: Beam Interactions with Materials and Atoms*, 256(1):419 – 422, 2007.

[106] R. Moroni, F. Bisio, F. Buatier de Mongeot, M. Canepa, C. Boragno, L. Mattera, and U. Valbusa. Ion sculpting: A tool for tuning magnetic anisotropy in ultrathin films. *Nuclear Instruments and Methods in Physics Research Section B: Beam Interactions with Materials and Atoms*, 257(1-2):359 – 364, 2007.

[107] A. Toma, B. Šetina Batič, D. Chiappe, C. Boragno, U. Valbusa, M. Godec, M. Jenko, and F. Buatier de Mongeot. Patterning polycrystalline thin films by defocused ion beam: The influence of initial morphology on the evolution of self-organized nanostructures. *Journal of Applied Physics*, 104(10), 2008.

[108] A. Toma, D. Chiappe, B. Šetina Batič, M. Godec, M. Jenko, and F. Buatier de Mongeot. Erosive versus shadowing instabilities in the self-organized ion patterning of polycrystalline metal films. *Physical Review B*, 78(15):153406, 2008.

[109] B. Šetina Batič and M. Jenko. Orientation-dependent ion beam sputtering at normal incidence conditions in FeSiAl alloy. *Journal of Vacuum Science and Technology A, accepted for publication*, jun 2010.

[110] B. Šetina Batič and M. Jenko. Structuring polycrystalline Fe-Si-Al steel surfaces by means of ion beam - the role of grain orientation. *Surface and Interface Analysis*, 2010.

[111] Gatan INC. *PECS - Precision Etching and Coating System; Users Manual*, 5 edition, 2000.

[112] G. Binnig, C. F. Quate, and Ch. Gerber. Atomic force microscope. *Physical Review Letters*, 56(9):930–933, 1986.

[113] Franz J. Giessibl. Advances in atomic force microscopy. *Rev. Mod. Phys.*, 75(3): 949–983, 2003.

[114] I. Horcas, R. Fernandez, J. M. Gomez-Rodriguez, J. Colchero, J. Gomez-Herrero, and A. M. Baro. WSxM: A software for scanning probe microscopy and a tool for nanotechnology. *Review of Scientific Instruments*, 78(1), 2007.

[115] Valerie Randle and Olaf Engler. *Introduction to Texture Analysis: Macrotexture, Microtexture and Orientation Mapping*. CRC Press, 2000.

[116] *HKL Channel 5, User's Manual*, 2007.

[117] Valerie Randle. *Recent Developments in Electron Backscatter Diffraction*, volume 151, pages 363 – 416. Elsevier, 2008.

[118] Dae Won Moon and Kyung Joong Kim. Surface topography development on ion-beam-sputtered surfaces: Role of surface inhomogeneity induced by ion-beam bombardment. *Journal of Vacuum Science & Technology A: Vacuum, Surfaces, and Films*, 14(5):2744–2756, 1996.

[119] P Mishra, P Karmakar, and D Ghose. Electrical characterization of oxygen-induced nanosized ripples on aluminum thin films by conductive atomic force microscopy. *Nuclear Instruments & Methods in Physics Research B - Beam Interactions with Materials and Atoms*, 243(1):16–19, 2006.

[120] P. Mishra and D. Ghose. The energy dependence of sputtering induced ripple topography in Al film. *Nuclear Instruments & Methods in Physics Research B - Beam Interactions with Materials and Atoms*, 266(8):1635–1641, 2008.

[121] P Karmakar and D Ghose. Low energy Ar+ ion beam induced kinetic roughening of thin Pt films on a Si substrate. *Nuclear Instruments & Methods in Physics Research B - Beam Interactions with Materials and Atoms*, 222(3-4):477–483, 2004.

[122] Celia Polop, Christian Rosiepen, Sebastian Bleikamp, Robert Drese, Joachim Mayer, Arbi Dimyati, and Thomas Michely. The STM view of the initial stages of polycrystalline Ag film formation. *New Journal of Physics*, 9(3):74, 2007.

[123] H. D. Espinosa, B. C. Prorok, and B. Peng. Plasticity size effects in free-standing submicron polycrystalline FCC films subjected to pure tension. *Journal of the Mechanics and Physics of Solids*, 52(3):667 – 689, 2004.

[124] SPI supplies on-line catalogue. http://www.2spi.com/catalog/gold-sub.shtml.

[125] Gianangelo Bracco and Davide Cavanna. Decay of nanoripples on Au(111) studied by He atom scattering. *Physical Review B*, 76(3):033411, 2007.

[126] Benny Davidovitch, Michael J. Aziz, and Michael P. Brenner. On the stabilization of ion sputtered surfaces. *Physical Review B*, 76(20):205420, 2007.

[127] M Jenko, J Fine, and D Mandrino. Effects of selenium surface segregation on the texture of a selenium-doped fesi alloy. *Surface and Interface Analysis*, 30(1):350–353, 2000.

[128] M. Jenko, F. Vodopivec, B. Pracek, M. Godec, and D. Steiner. AES studies of antimony surface segregation in non-oriented silicon steel. *Journal of Magnetism and Magnetic Materials*, 133(1-3):229 – 232, 1994.

[129] M. Godec, M. Remskar, Dj. Mandrino, and M. Jenko. Scanning tunneling microscopy study of Sb-alloyed electrical steel sheet. *Applied Surface Science*, 143 (1-4):1 – 5, 1999.

[130] G. Stokkan. Relationship between dislocation density and nucleation of multicrystalline silicon. *Acta Materialia*, 58(9):3223 – 3229, 2010.

[131] Hitoshi Shindo, Toshinori Igarashi, Wataru Karino, Akihiro Seo, Maiko Yamanobe-Hada, and Masa aki Haga. Stabilities of crystal faces of anhydrite ($caso_4$) compared by afm observation of facet formation processes in aqueous solutions. *Journal of Crystal Growth*, 312(4):573 – 579, 2010.

[132] K. J. Kim and K. H. Jung. Mechanism of facet formation on ni surfaces by sputtering with oxygen ion beams. *Surface and Interface Analysis*, 26(3):224–232, 1998.

[133] K. Wittmaack. Effect of surface roughening on secondary ion yields and erosion rates of silicon subject to oblique oxygen bombardment. *Journal of Vacuum Science & Technology A: Vacuum, Surfaces, and Films*, 8(3):2246–2250, 1990.

[134] F. Frost, B. Ziberi, A. Schindler, and B. Rauschenbach. Surface engineering with ion beams: from self-organized nanostructures to ultra-smooth surfaces. *Applied Physics A - Materials Science & Processing*, 91(4):551–559, 2008.

[135] Bo Young Kim, Jae Sang Lee, Kye-Ryung Kim, Byung Ho Choi, and Bum Sik Park. Development of ion beam sputtering technology for surface smoothing of materials. *Nuclear Instruments and Methods in Physics Research Section B: Beam Interactions with Materials and Atoms*, 261(1-2):682 – 685, 2007.

[136] Franc Vodopivec. *Kovine in zlitine: kristalna zgradba, mikrostruktura, procesi, sestava in lastnosti*. Inštitut za kovinske materiale in tehnologije, 2002.

[137] Chun-Kan Hou. Effects of sulfur content and slab reheating temperature on the magnetic properties of fully processed nonoriented electrical steels. *Journal of Magnetism and Magnetic Materials*, 320(6):1115 – 1122, 2008.

[138] K.P. Mingard, B. Roebuck, E.G. Bennett, M.G. Gee, H. Nordenstrom, G. Sweetman, and P. Chan. Comparison of EBSD and conventional methods of grain size measurement of hardmetals. *International Journal of Refractory Metals and Hard Materials*, 27(2):213 – 223, 2009. International Conference on the Science of Hard Materials - 9.

[139] Joseph Goldstein, Dale Newbury, David Joy, Charles Lyman, Patrick Echlin, Eric Lifshin, Linda Sawyer, and Joseph Michael. *Scanning electron microscopy and X-ray microanalysis*. Kluwer Academic, 3 edition, 2003.

[140] D. Manova, M. Schreck, S. Mändl, B. Stritzker, and B. Rauschenbach. Orientation dependent sputter yield of Aluminium. *Surface and Coatings Technology*, 151-152: 72 – 75, 2002.

[141] Don E. Harrison Jr., P.W. Kelly, Barbara J. Garrison, and Nicholas Winograd. Low energy ion impact phenomena on single crystal surfaces. *Surface Science*, 76(2):311 – 322, 1978.

[142] M. Bickermann, S. Schmidt, B. M. Epelbaum, P. Heimann, S. Nagata, and A. Winnacker. Wet KOH etching of freestanding AlN single crystals. *Journal of Crystal Growth*, 300(2):299–307, 2007.

[143] Che-Ming Liu, Jyh-Chen Chen, Yi-Cheng Huang, and Hung-Lin Hsieh. The morphology of etch pits on a sapphire surface. *Journal of Physics and Chemistry of Solids*, 69(2-3):572–575, 2008.

[144] Takaomi Suzuki, Naoki Sugihara, Katsuya Teshima, Shuji Oishi, and Masayuki Kawasaki. Specific surface free energy and etch pit density of synthesized quartz crystal. *Journal of Crystal Growth*, 311(3):719–721, 2009.

List of Figures

1.1 Sputtering by ion beam. As ions strike the surface, they produce sputtering of the atoms from the substrate. 1

2.1 An Xe ion beam sputtered solid SiO_2 surface. Image from [5]. 4

2.2 Kinetic phase diagram for pattern formation on Cu(001)/Ag(001) surfaces. Each region in the diagram represents a different pattern formed on the surface [32]. 7

2.3 More energy is deposited at areas with a positive curvature, leading to a faster sputtering of these areas compared to the areas with a negative curvature. The elliptical shapes represent the deposition of ion energy inside the bulk according to Sigmund sputtering model. 9

2.4 Bradley and Harper's theory of sputtering: wave vector rotation. (a) Ripples perpendicular to ion beam direction form at near-normal incidence angles, and (b) ripples parallel to the ion beam form at grazing incidence [19]. 10

2.5 Scanning tunneling microscopy image of defects induced by single ion impacts on Pt(111) surface. Bombarding species was Xe at 5 keV. Image size is 770x770 Å^2. The image is taken from [52]. 13

2.6 Schematic representation of ion impact and defect evolution [4]. (a) An ion bombards the solid surface, defects are created in the bulk and on the surface. Some atoms are sputtered away, leaving vacancies on the surface. (b) Evolution after the ion impact: defects annihilate and recombine; bulk defects can diffuse to the surface to create surface defects. . . . 15

2.7 AFM images of the unbombarded and 16.7 keV Ar+ sputtered Co, Cu, Ag, Pt and Au surfaces at different angles of incidence. The bombarding fluence for Co, Cu, Ag, and Au is 1×10^{17} ions/cm^2, while that for Pt is 5×10^{16} ions/cm^2. The ion beam direction is from the bottom to the top. Image from Karmakar *et al* [68]. 17

2.8 Images of 9.7 keV Ar^+ sputtered 30 nm Pt thin films at an angle $\theta = 45°$, showing a sequence of the evolution of surface topography with increasing ion fluence. Image from Gose *et al.* [65]. 18

2.9 Model that describes the surface of a thin film undergoing ion beam sputtering. Image from [71]. 19

2.10 Simulated 100 nm × 100 nm surface morphologies for Cu bombarded by 1 keV ions at (a) normal incidence and (b) 80 ° incidence. Image from [71]. 19

2.11 AFM images of Ag(110) after ion sputtering at normal incidence for different temperatures: a) 160 K, b) 230 K, c) 270 K, d) 290 K, e) 320 K, f) 350 K. The size of the images is 350 × 350 nm^2. [15] 22

2.12 STM topographies after normal angle ion erosion of Pt(111) at 650 K. The removed amount of material (in monolayers) is indicated, as well as the temperatures and the image scales. The inset in (a) is shown at higher magnification [82]. 23

2.13 Diffusive and erosive regimes and the surface morphologies produced in each of them. [15] 24

2.14 Example of grain boundary area: illustration shows differential sputtering of different grains and a steep intergranular boundary. The material is polycrystalline FeSiAl alloy. In this image we can also distinguish between elevated and depressed features. 25

2.15 Example of triangular etch pits in a grain of FeSiAl alloy. 26

4.1 Schematic representation of film growth methods: (a) thermal deposition of the film, (b) sputter deposition of the film. 32

4.2 The polished steel specimen as seen by optical microscopy. 33

4.3 The ion beam sputtering system at the Genova Department of Physics, where thin film sputtering experiments were performed. 34

4.4 Gatan PECS system, which was used for ion beam sputtering of the bulk specimens. 35

4.5 A two-dimensional sinusoidal wave and the corresponding self-correlation function. 37

4.6 Wavelength definition as obtained from self-correlation function. The profile is along the self-correlation image shown in fig. 4.5, where the sinusoidal wavelength is 88 nm. 38

4.7 Horizontal and vertical cosines and their corresponding 2D FFTs. 38

4.8 An example of 2D FFT as was performed for "real" AFM images. The image is an 88 nm wave, and the corresponding 2D FFT shows that the distance between two peaks is in fact 22.62 $1/\mu m$, which is 88 nm wavelength. 39

4.9 The scanning electron microscope used for experimental work. 41

4.10 EBSD automatic indexing procedure. 43

4.11 Construction of EBSD inverse pole figure. 43

5.1 AFM images of three different film thicknesses, deposited by sputter deposition method. The image sizes are in all three cases 1 $\mu m \times$ 1 μm. . . . 46

5.2 RMS roughness evolution of sputter deposited gold films. An increasing trend of surface roughness vs. the film thickness can be observed. 47

5.3 (a) Inverse pole plot in the normal (Z) direction and (c) pole figures obtained by orientation mapping of 30200 points shows a clear preference for (111) grain growth. A representative pattern in (b) shows that despite small grain sizes, a good-quality pattern can be obtained and indexed. . . 48

5.4 XRD measurements of Au sputter deposited and thermally deposited thin film. (111) peak is large, while the other peak (200) is suppresed. . . . 49

5.5 Comparison of surface morphologies of initial 150 nm thin films of Au, (a) SEM images and (b) AFM images. The AFM image color scale is given in nm. The sputter deposited specimen exibits smaller and more uniform grains, and surface roughness is much larger in the case of the thermally deposited specimen. 50

5.6 Flame-annealed thin Au film of 150 nm thickness, deposited on mica. The specimen exhibits a very smooth surface, as is evident from the color scale (in nm). 50

5.7 Roughness histograms of the three films. Due to large differences in heights, the scale is logarithmic. 51

5.8 Grain size distribution of the Au films. 51

5.9 Sputter time evolution of sputter deposited specimens, SEM and AFM images as insets. 52

5.10 Evolution of surface morphology: (a) 7 minute sputter time, (b) 75 minute sputter time. Below each image is a corresponding 2D FFT image, showing the periodicity of the ripple. 53

5.11 Evolution of average separation distance (wavelength) and RMS roughness of the sputter deposited thin film. 54

5.12 Sputtering an 150 nm thermally deposited film also results in regular ripple formation. Two SEM images with AFM images as insets or two different sputtering times are shown. 54

5.13 Evolution of average separation distance (wavelength) and RMS roughness of the thermally deposited 150 nmthin film. 55

5.14 Patterning a 150 nm thin Au flat film, deposited on mica substrate. 56

5.15 Evolution of surface RMS roughness and wavelength of the resulting ripples on a flat film deposited on mica substrate. 57

5.16 Shadowing mechanism. The taller and larger grains shadow the smaller grains, so these regions sputter at a slower rate [108]. 58

5.17 (a), (b): Average amplitude (h) and periodicity (Λ) of the formed nanostructures vs. ion fluence, derived from the AFM images. The green triangles refer to the flat films, blue open squares to thermally deposited films, and red closed squares to sputter deposited films. Insets show a horizontal rigid shift of the curves representing the rougher films, which leads to an overlap of the data points of the rougher films and the flat film. (c), (d) and (e): Topographs of the different sample series irradiated with the same scaled ion dose; (c) thermally deposited specimen, (d) Sputter deposited specimen, (e) flat film. The respective 2D FFT line cuts evidence the equivalence of wavelength [108]. 59

5.18 SEM image of the ripples propagating through individual grain boundaries. (a) Sputter deposited film with smaller grains; (b) Thermally evaporated film with larger grains. Both films were sputtered by the same ion fluence. 60

5.19 SEM image of the ripples propagating through individual grain boundaries in the case of the flat film with large grains. A slight mismatch of the ripple orientation can be observed on the grain boundary, but otherwise the ripple propagation is not hindered and the ripple lengths can exceed several micrometers. 61

6.1 Classification of ion beam induced surface morphological properties as proposed by Carter *et al.* [17]. 64

6.2 Examples of grain boundary delineation - intergranular structures. The material is FeSiAl alloy, etched by Ar^+ ions at (a) 6 keV, 5×10^{18} ions/cm^2, (b) 10 keV, 6×10^{18} ions/cm^2 and (c) 1×10^{19} ions/cm^2. (a) and (c) were both sputtered at normal incidence, and (b) was sputtered at a 45° angle. . 65

6.3 Examples of etch pits that form on the surface of FeSiAl alloy during normal incidence ion beam sputtering. (a) 10 keV, 2×10^{18} ions/cm^2, (b) 10 keV, 3×10^{18} ions/cm^2 and (c) 6 kV, 3×10^{18} ions/cm^2. 67

6.4 Etch pits are different in shape as well as in depth. AFM images of pits present in a single grain. The FeSiAl alloy was sputtered at normal incidence, using a 7 keV beam and the ion fluence was 4.5×10^{18} ions/cm^2. . . 68

6.5 Ripple pattern formation along with much deeper pits. AFM image and line profiles, showing the rippled surface. The specimen received $3times10^{18}ions/cm$, and the beam energy was 6 kV. 69

6.6 An example of protuberant features - triangular facet like structures. FeSiAl alloy was bombarded by Ar^+ ions of 6 keV energy at 60° angle of incidence for 40 minutes with 300 μA current. 69

6.7 Triangular structures as they formed on a grain in polycrystalline FeSiAl alloy: 3D AFM image representation, 2D AFM image representation and the corresponding 2D FFT, showing the image periodicity. FeSiAl alloy was bombarded by Ar^+ ions of 6 keV energy at 60° angle of incidence for 40 minutes with 300 μA current. 70

6.8 Some line profiles along the triangular structures produced by ion beam bombardment. (FeSiAl alloy was bombarded by Ar^+ ions of 6 keV energy at 60 ° angle of incidence for 40 minutes with 300 μA current.) 70

6.9 The structures that form resemble facets with steep sides instead of ripples with rounded tops. 71

6.10 Comparison of AFM line profiles for three different sputtering conditions. 72

6.11 An SEM and AFM micrograph of a grain that underwent smoothing mechanism - average RMS roughness of the surface as was estimated from AFM images is 2 nm. 73

6.12 A "box plot" of roughness measurements of individual pattern class: smooth, ripple, and triangular facet-like structures. Data collected on a specimen sputtered at 60° angle of incidence, 300μA current for 40 minutes. 73

7.1 Microstructure of FeSiAl alloy, SE micrograph. 76

7.2 EBSD mapping of the specimen. (a) shows the "pattern quality" map, and (b) is the orientation map, where individual grains are color-coded according to their orientation. 77

7.3 Histogram of grain sizes. The average grain diameter is 40 μ, determined from EBSD analysis. 77

7.4 Inverse pole plot in Z-direction of the FeSiAl alloy. It can be seen that, despite some texture, no orientation dominates. 78

7.5 Energy dispersive spectroscopy (EDS) analysis performed on several different grains. The spectra show that the grains are homogeneous in composition within the limits of the EDS technique. 78

7.6 A larger-scale view of the FeSiAl alloy sputtered specimen at normal incidence conditions. The grains etch at different rates, and each grain develops an individual pattern limited by the grain boundary. The specimen was sputtered at normal incidence, 6 keV, receiving about 3×10^{18} ions/cm^2 ion fluence. 80

7.7 AFM image of grain boundary area. Different grains exhibit different step-heights between them. AFM scan size is 10x10 μm^2. 81

7.8 Etch pit formation - different grains exhibit different etch pit shapes, which can be generally classified into three shapes: "square", "rectangular" and "triangular". 81

7.9 Three grains with three different orientations and their EBSD patterns. Different etch pit shapes are evident: Triangular in the case of spot 1, square in spot 2 and rectangular in spot 3. The sample has been tilted to 70° in the microscope, thus the pit shape in this image is somewhat distorted. 82

7.10 Four different classes observed in patterning Fe-Si-Al alloy with an off-normal incidence Ar^+ ion beam. The images were collected from different specimens sputtered at a 60° angle. 84

7.11 SEM micrograph of the surface of an off-normal incidence sputtered specimen. The pattern in each grain is confined to that grain, steps between individual grains are also observed. 85

7.12 Inverse pole figure constructed from a larger number of grains showing the connection between surface crystal structure and the resulting pattern. 85

7.13 Fe-Si phase diagram. The diagram shows that Fe-10% Si has a bcc structure. 86

7.14 Etch pits formed at normal incidence sputtering conditions in (a) monocrystalline Fe and (b) polycrystalline alloy. Both specimens were sputtered using the same conditions: 10 keV beam and 3×10^{18} ions/cm^2. 87

7.15 SEM micrograph of a (100) single crystal Fe specimen sputtered at normal incidence employing a 10 keV Ar^+ and ion fluence of 3×10^{18} ions/cm^2. . . 88

7.16 SEM micrograph of the (110) single crystal Fe specimen sputtered at normal incidence employing a 10 keV Ar^+ and ion fluence of 3×10^{18} ions/cm^2. 88

7.17 Roughness of normal incidence sputtered specimens of Fe-10% Si at (111) and (100) orientations. The AFM image size is 10×10 μm in both cases. The single crystal substrates received 3×10^{18} ions/cm^2 and the beam energy was 10 keV. 89

List of Tables

4.1 Steel compositions. 33

7.1 EDS analysis performed on several different grains showing the compositional differences between individual grains. The C peak was excluded from the analysis. 79

Selected bibliography of the author

The work of this thesis has been published in four SCI indexed journals.

1. A. Toma, B. Šetina Batič, D. Chiappe, C. Boragno, U. Valbusa, M. Godec, M. Jenko, F. Buatier de Mongeot *Patterning polycrystalline thin films by defocused ion beam: the influence of initial morphology on the evolution of self-organized nanostructures.* **Journal of Applied Physics, 2008, 104 (10), 104313, doi: 10.1063/1.3021100**

2. A. Toma, D. Chiappe, B. Šetina Batič, M. Godec, M. Jenko, F. Buatier de Mongeot *Erosive versus shadowing instabilities in the self-organized ion patterning of polycrystalline metal films* **Physical Review B, 2008, 78 (15), 153406, doi: 10.1103/PhysRevB.78.153406**

3. B. Šetina Batič, M. Jenko. *Structuring polycrystalline Fe-Si-Al steel surfaces by means of ion beam - the role of grain orientation* **Surface and Interface Analysis, 2010, doi: 10.1002/sia.3326**

4. B. Šetina Batič, M. Jenko. *Orientation-dependent ion beam sputtering at normal incidence conditions in FeSiAl alloy* **Journal of Vacuum Science and Technology A, 2010** - accepted article.